TELECOMMUNICATIONS ENGINEERING SCHOOL

TECHNICAL UNIVERSITY OF CARTAGENA

Final Degree Project

Research on Leaky-Wave antennas for microwave and infrared applications.

AUTHOR: Jorge Julio Jácome Muñoz
DIRECTORS: Juan Sebastián Gómez Díaz
Julien Perruisseau-Carrier
Alejandro Álvarez Melcón

Cartagena, July 2013

Autor	Jorge Julio Jácome Muñoz
E-mail del Autor	jj.jacome.munoz@gmail.com
Director	Juan Sebastián Gómez Díaz
E-mail del Director	juan-sebastian.gomez@epfl.ch
Director	Julien Perruisseau-Carrier
E-mail del Director	julien.perruisseau-carrier@epfl.ch
Director	Alejandro Álvarez Melcón
E-mail del Director	alejandro.alvarez@upct.es
Título del PFC	Investigación en antenas Leaky-wave para aplicaciones de microondas e infrarrojos. Research on Leaky-Wave antennas for microwave and infrared applications.

Resumen

En este proyecto se realiza un estudio de antenas en tecnología leaky-wave en diferentes rangos de frecuencia. En el primer caso, a frecuencias de microondas, se estudia una estructura tipo champiñón basada en líneas metamateriales, y se propone una metodología de diseño para optimizar el nivel de lóbulo principal a secundario. Para ello, se realiza un estudio de la influencia de los parámetros geométricos en la constante compleja de propagación mediante simulaciones full-wave. Con los resultados de este estudio, se realiza un diseño taper de la antena, con el que se consigue una reducción de los lóbulos secundarios a una frecuencia determinada. La antena diseñada se encuentra actualmente en fabricación en los laboratorios de la EPFL (Suiza), lugar donde se desarrolló una parte del proyecto.

En la segunda antena, se aplican conocimientos y técnicas de microondas para diseñar el equivalente óptico a una antena leaky-wave. Se parte de una estructura óptica de guiado basada en semiconductores, la cual puede reconfigurarse mediante inyección de portadores en los materiales utilizados. Con base a esto, se propone una implementación alternativa en tecnología de microfluidos, con el fin de facilitar el proceso de fabricación e introducir nuevas prestaciones debido a la flexibilidad y versatilidad que aporta esta tecnología.

Abstract

In this project, a study on leaky-wave antennas is performed at different frequency ranges. In the first research line, at microwave frequencies, a composite right/left-handed transmission line based on a mushroom-type structure is analyzed, and a design methodology for optimizing the side lobe level is proposed as well. For that purpose, a study of the influence of geometrical parameters on the complex propagation constant is carried out with full-wave simulations. With the results obtained from this study, a tapered antenna is designed, and achieves the reduction of side lobes at a determined frequency. The designed antenna is currently under fabrication at the EPFL (Switzerland) laboratories, place where a part of this project was developed.

In the second line, concepts and techniques related to microwave structures are applied to design an optical equivalent of a leaky-wave antenna. The reference optical guiding structure is made of semiconductor materials, and can be reconfigured via carrier injection. Based on this, an alternative implementation is proposed with microfluidics technology, with the purpose of reducing manufacturing process complexity and introducing new features due to flexibility and versatility that microfluidics provide.

Titulación	Ingeniería de Telecomunicación
Departamento	Tecnologías de la Información y Comunicaciones
Fecha de Presentación	19 de julio de 2013

Contents

Introduction

Antennas are a fundamental component in any wireless communication system. They are the structures in charge of linking guided and space-propagating waves. Over the years, a large number of structures have been proposed and developed to provide this transition for guiding and space-propagating waves, especially in the microwave and millimeter-wave frequency range. Some examples include patch antennas [Balanis, 2005], cavity-backed antennas [Álvarez Melcón, 1998], spiral structures [Balanis, 2005], etc. One interesting type of antennas, due to its high directivity and gain, are the so-called leaky-wave antennas (LWA) [Oliner and Jackson, 2007].

The first leaky-wave antenna known was introduced by W. W. Hansen in 1940, consisting of a slitted rectangular waveguide. The topic of leaky-wave antennas did not see a lot of development until the 1950s. Starting in the 1950s a variety of different types of leaky-wave antennas were introduced, together with some numerical methods for their analysis. Most of these initial leaky-wave antennas were based on closed waveguides, where the power leakage was achieved by introducing long uniform slits into the waveguides to allow them to radiate. Since then, many investigations of (1D and 2D) uniform, quasi-uniform and periodic leaky wave antennas were conducted and summarized in a variety of comprehensive reports [Balanis, 2007]. Radiation phenomenon in LWAs, as well as in other aperture-type antennas, takes place at a fixed angle for a given frequency. Ideally, it is desired that all available power is radiated in this direction and only at it. Antennas with uniform field aperture distribution do not produce radiation exclusively at this angle, but also at angles different to the desired one; these undesired contributions are represented in the radiation pattern as side lobes.

The discovery of metamaterials has led to many novel microwave components and applications, including antennas. Recent leaky wave antennas based on composite right/left-handed structures obtained unique radiation effects due to their unusual propagation properties [Caloz and Itoh, 2006]. This has led to improvements in features such as beam scanning, improving its capabilities in both 1D and 2D antennas. Applications based on this remarkable feature are affected, however, by a poor control of the leakage factor, and consequently, by the side lobe level. The side lobe level is the ratio, in decibels (dB), of the amplitude at the peak of the main lobe to the amplitude at the peak of a side lobe. The unavailability of analytical expression for leakage factor for most leaky-wave antennas and the non-trivial influence of the geometrical parameters on it, make the

modification of the antenna aperture illumination pattern a difficult task. This can be achieved by changing the antenna geometry along its longitudinal direction, which is commonly known as taper design ([Gómez, 2005], [Gómez, 2008], [García-Vigueras, 2010]).

On the other hand, while antennas in the radiowave and microwave frequencies are widely used in nowadays communication systems (Radio, TV, Cell phones, etc), their optical analog is basically non-existent in today's technology. Emerging fields such as nanophotonics and optoelectronics have been gaining significant attention in recent years and, in particular, the interest in plasmonics and Silicon-on-Isolator (SOI) devices, such as optical antennas has increased rapidly ([Wang, 2011], [Sederberg, 2011]). The SOI platform is a very interesting solution, since it enhances electronic tunability of the optical parameters of silicon, thus providing versatility and reconfigurability in such antennas. Plenty of optoelectronic devices, besides antennas, have been designed by using this platform. Nevertheless, practical implementation of a LWA may be quite difficult, or even non-feasible in some cases. At the same time, the field of optofluidics has attracted substantial attention due to the potential of integrating optics with microfluidics, thus enabling cost-effective methods for lab-on-a-chip applications [Psaltis, 2006], which represents a very appealing alternative to the afore mentioned approaches. Most optical systems are currently made with solid materials such as glasses, metals and semiconductors, but there are cases in which it is advantageous to use fluids. Fluidic replacement or modification leads to reconfigurable optical systems, whereas the implementation of optics through the microfluidic toolkit gives highly compact and integrated devices. [Psaltis, 2006]

In this context, this project presents the design of two leaky wave antennas at different frequency ranges. First, a composite-right/left-handed LWA designed to operate at microwave frequencies with its fundamental harmonic, which constitutes the basis for this work. A geometrical parameter influence study is carried out with the purpose of providing insight on the control of the leakage factor. Later on, a design methodology is proposed for an amplitude taper design to reduce side lobe level to a desired value. The methodology includes an analysis of the aperture illumination distribution on LWAs and its effect on side lobes. Moreover, the radiation pattern is predicted by using a MATLAB routine, which implements formulas related to this theoretical basis. Full-wave simulations indicate that the used methodology is appropriate to achieve the objective. Due to the excellent results, the antenna is under manufacturing process at the time of writing this report. It is important to notice that there is only evidence of one taper design in the field of metamaterials antennas [Siragusa, 2012].

Second, an optical LWA based on Silicon-On-Isolator technology is proposed. The use of semiconductor perturbations in this antenna facilitates electronic tuning of the radiation pattern via carrier injection. Regarding the optical LWA, variations in the designed antenna are proposed in order to simplify the fabrication complexity and enhance versatility by using microfluidics. Results demonstrate that a practical implementation with this technology is very promising for future optoelectronic communication systems, allowing reconfiguration capabilities. Its practical implementation is being evaluated at the École Polytechnique Fédérale de Lausanne, university where an important part of this project was developed.

Project Scope

The objectives of this project, for both research lines, are presented next. For the first research line, the microwave composite right/left-handed LW antenna, the main objective is **the reduction of the side lobe level in the radiation pattern via a tapered geometry design**. This objective can be achieved by developing the following steps:

- Study and design of a leaky-wave antenna based on a mushroom-type structure.
- Study of the influence of the geometrical parameters in the complex propagation constant in a leaky-wave antenna based on a mushroom-type structure.
- Evaluation of the viability of an amplitude taper design, by a proper control of the normalized attenuation constant, in the left-handed and right-handed frequency bands.
- Use of a design technique to obtain dimensions of the geometrical parameters in a mushroom structure, which allow the variation of the attenuation constant at a given frequency with an invariant phase constant.
- Design of an amplitude taper design for a leaky-wave antenna with the purpose of reducing side lobe level to a given value, based on a customized amplitude aperture distribution.
- Design of a manufacturable tapered CRLH-LWA, considering suitable materials and the limitations of the technical available resources.

On the other hand, for the second research line, the main objective **is the design of an optical equivalent of a leaky-wave antenna by applying radiowave and microwave antenna theory, focusing on a practical and versatile implementation**. The following steps will be useful in order to achieve the main goal:

- Study of a rectangular optical fiber, as a host transmission line.
- Study of the influence of semiconductor corrugations inside the host transmission line.
- Design of an optical leaky-wave antenna in the near-IR frequency range based on microfluidics technology.

Most of the theoretical aspects related to leaky wave antennas are synthesized in Chapter 3, which constitutes a common ground for the two research lines developed in this project. Chapter 3 reviews fundamental concepts of this type of structures, as well as a method for

calculating the complex propagation constant in periodic structures. Additionally, there is a section that treats the reduction of side lobes by controlling the attenuation constant along the antenna length.

The first and second research lines are developed in Chapter 4 and Chapter 5, respectively. Chapter 4 contains a review of the current state-of-the-art of the CRLH-LWA, as well as a review on the side lobe level optimization of this type of antennas. The physical insights obtained from the studies performed lead to a simple yet complete approach to effectively control both the phase and attenuation constants. Moreover, aspects related to manufacturing process are considered in the final optimized design.

Chapter 5 is focused on the application of microwave theory concepts into a specific structure that operates in the optical frequency regime. A novel practical implementation is also proposed, highlighting its advantages over the base reference antenna. Chapter 6 includes the final conclusion of this project, and Chapter 7 contains a summary of the consulted references.

Theoretical fundamentals

3.1. Leaky Wave Antennas

Leaky wave antennas [Oliner and Jackson, 2007] are a class of antennas that use a traveling wave on a guiding structure as the main radiating mechanism. These antennas are capable of producing narrow beams, with the beamwidth limited by the size of the structure; they also possess the advantage of simplicity, since no complicated feed network is required as, for example, in a planar array antenna. Because of this simplicity, they are often attractive for higher microwave and millimeter-wave frequencies. Most leaky-wave antennas have the inherent property that the beam scans with frequency. [Balanis, 2007]

Leaky wave antennas are based on the concept of leaky-modes in open guiding structures. In conventional waveguiding structures, such as transmission lines, propagation phenomenon occurs along the longitudinal direction. Depending on the waveguide's geometry and the boundary conditions applied on it, the propagating fields have a specific distribution inside it. These discrete solutions of Maxwell's equations [Ramo et al, 1994] are commonly known as modes. Electromagnetic guided modes propagate through the line without attenuation, considering that no dielectric and ohmic losses exist and the wave's frequency is above cutoff.
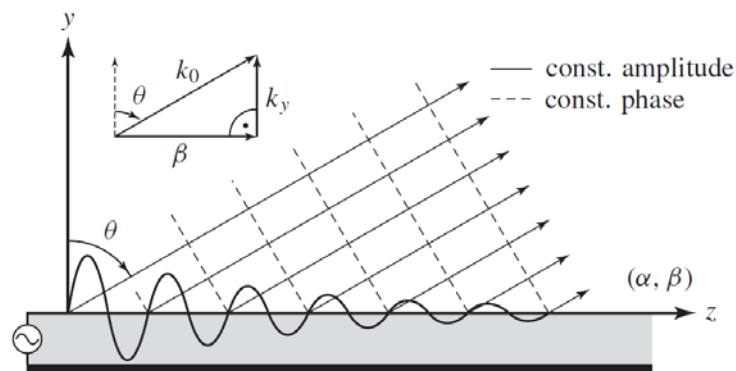

Figure 3.1: Schematic representation of a LW structure. Reproduced from [Caloz and Itoh, 2006]

A leaky mode, on the other hand, can propagate inside the open structure and, at the same time, radiate or "leak" power to the surrounding space if specific conditions are satisfied (hence the name of the mode). As a consequence, unlike purely guided modes, which are characterized by a real propagation constant, a leaky mode is characterized by a complex propagation constant due to the leakage of power, consisting of both a phase constant β and an attenuation constant α (even if the structure is lossless). A LW structure is schematically represented in Fig 3.1. The fields in free space above the structure exhibits the general wave form

$$\psi(x,z) = \psi_0 e^{-\gamma z} e^{-jk_y y} = \psi_0 \left(e^{-\alpha z} e^{-j\beta z} \right) e^{-jk_y y} , \tag{3.1.1}$$

where $\gamma = \alpha + j\beta$ is the complex propagation constant of the wave in the direction of the waveguide (z), and k_y is the propagation constant perpendicular to this direction, related to β by [Oliner, 2003]

$$k_y = \sqrt{k_0^2 - \beta^2} , \tag{3.1.2}$$

where k_0 is the free-space wavenumber. For waves slower than the velocity of light (phase velocity - $v_p < c$) or $\beta > k_0$, the perpendicular propagation constant is imaginary, and there is exponential decay along y. In contrast, for waves faster than the velocity of light or $\beta < k_0$, the perpendicular propagation constant has also a real component, and therefore leakage phenomenon occurs since there is propagation along y. According to this, a slow wave is a guided wave, whereas a fast wave is a leaky wave. As stated, a leaky wave will radiate into space if the fast-wave condition is satisfied:

$$\left| \frac{\beta}{k_0} \right| < 1 \tag{3.1.3}$$

As a general rule, the phase constant of the leaky wave controls the beam angle, while the attenuation constant controls the beamwidth. As illustrated in Fig. 3.1, the angle of radiation of the main beam can be obtained by [Oliner and Jackson, 2007]

$$\theta_m \approx \sin^{-1}\left(\frac{\beta}{k_0} \right), \tag{3.1.4}$$

and the beamwidth can be obtained by [Oliner and Jackson, 2007]

$$\Delta\theta \approx \frac{1}{(L/k_0)\cos\theta_m} . \tag{3.1.5}$$

From (3.1.4), in order to radiate power from an open waveguiding structure to the surrounding space with a real angle, the longitudinal propagation constant must be smaller than the free-space wavenumber k_0, which implies that a transverse propagation constant exists and it has a real component. When the longitudinal propagation constant is greater than the free-space wavenumber k_0, the angle obtained from (3.1.4) is a complex value and does not correspond to an actual radiation phenomenon.
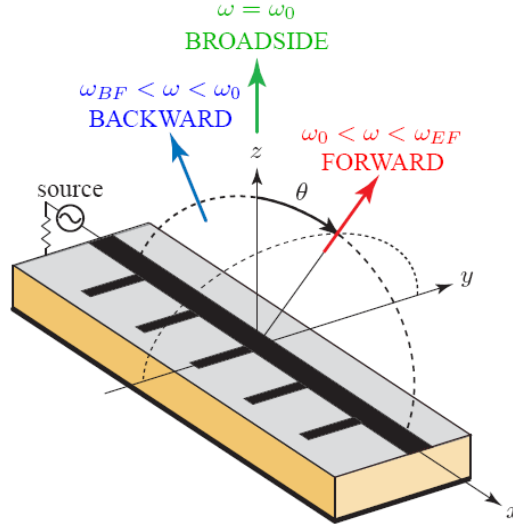
Figure 3.2: Beam scanning capability in forward and backward quadrants. Reproduced from [Caloz and Itoh, 2006]

Hence, no propagation occurs along the transverse direction, while non-radiative propagation along the longitudinal direction occurs. If the waveguide is dispersive (β is a non-linear function of ω), a frequency scanning phenomenon appears, since the main beam angle is also frequency dependent. This suggests that radiation phenomena can occur, theoretically, in any angle from back-fire (θ_m=-90º) to end-fire (θ_m=+90º) directions if the longitudinal propagation constant of the leaky mode varies across the range [$-k_0, +k_0$], as shown in Fig. 3.2.

On the other hand, the beamwidth depends primarily by the antenna length L, but is also influenced by the aperture field amplitude distribution. The antenna length L is usually selected for a given value of alpha, in order to obtain a determined efficiency value of radiated power; a usual radiation efficiency value is 90%, and the remaining 10% of power is absorbed by a matched load. For 90% of radiated power, we find [Oliner, 2003]

$$\frac{L}{\lambda_0} \approx \frac{0.18}{\alpha / k_0}; \qquad \Delta\theta \approx \frac{\left(\alpha / k_0\right)}{0.18\cos\theta_m} \qquad (3.1.6)$$

From (3.1.6), large values of α provide wider main beams, because of the fact that all the power has leaked out after a short length, which implies that the resulting radiation aperture [Kraus and Marhefka, 2001] is small and the resulting fan beam is wide. In contrast, small values of α provide narrow beams, since the antenna has to be sufficiently long to leak all the power out of it, resulting in a large radiation aperture and consequently, a very directive fan beam. In the case of a 1D leaky wave antenna, the beam is narrow in the scan plane and fat in the transverse plane, whereas in 2D leaky wave antennas, the beam is narrow in both planes, hence the radiation pattern is known as a pencil beam.

Regarding classification, leaky wave antennas can be divided into different categories, depending on the geometry and the principle of operation. Structures can be classified in one dimensional or two dimensional; another classification is depending on whether the geometry of the guiding structure is uniform or is periodically modulated along its length.

The geometry of uniform leaky wave antennas does not change in the longitudinal direction. The radiation on this type of antennas is limited to the forward quadrant and can, potentially, scan in any angle from broadside to end-fire. The leaky mode in the waveguiding structure is fast and radiate to surrounding space when the structure is open. [Gómez et al, 2005].

In periodic leaky wave antennas, the waveguiding structure is modulated periodically in some fashion in the longitudinal direction. Unlike uniform antennas, where the fundamental mode is always fast, the fundamental mode in a periodic antenna is slow, so that it cannot radiate by itself, and the addition of perturbations periodically produces the radiation. This fundamental difference between these types of antennas affects directly the scan ranges.

By including some periodical modulation in the guiding structure, this periodicity creates a guided wave that consists of an infinite number of space harmonics, each characterized by phase constant β_n and related to each other by [Oliner, 2003]

$$\beta_n d = \beta_0 d + 2\pi n \qquad (3.1.7)$$

where d is the period and β_0, the fundamental space harmonic, is simply the original β of the dominant mode of the unperturbed waveguide, but somehow perturbed due to the presence of the periodic perturbations. β_n can take on a large variety of values, so that these space harmonics can be forward or backward in nature, and be slow or fast.

All the space harmonics are tied together, and all of them together comprise the dominant mode of the loaded structure. If the structure is open, a space harmonic that is fast will radiate; thus, the whole mode becomes leaky if one or more of these space harmonics becomes fast [Oliner, 2003]. Usually, for a practical LWA with optimized physical dimensions, the spatial harmonic n=-1 is chosen. Periodic leaky wave antennas can, potentially, radiate at any angles ranging from back-fire to end-fire, through broadside.

3.2. Analysis of periodic structures

In the previous section, aspects related to leaky wave fundamentals have been treated briefly, but concisely. Until now, all the theoretical reasoning and analyses have been done around the complex propagation constant, which is crucial for a well understanding of the behavior of any electromagnetic guiding structure. Due to this, it is essential to know how to calculate this valuable information from any structure, in particular for leaky wave antennas.

Both of the antennas studied and designed in this project are composed of a cascade of a finite number of identical unit-cells along the longitudinal direction. Therefore, as periodic structures, the analysis is based on a very important concept: the Bloch-Floquet theorem [Floquet, 1883], which will be revised next. Later, the calculation of the complex propagation constant is carried out by imposing periodic boundary conditions in a two-port network characterized by its transmission parameter matrix.

Consider an arbitrary structure periodic with period p and infinitely long, as illustrated in Fig. 3.3. The geometry periodicity forces the fields to be periodic; hence the fields of a wave propagating along such a structure may differ only by a complex exponential constant (3.2.1) from the fields one period farther. This can be expressed mathematically as

$$C = e^{-\gamma p}, \quad \gamma = \gamma(\omega) = \alpha(\omega) + j\beta(\omega) \tag{3.2.1}$$

$$\frac{\psi(z+p)}{\psi(z)} = \frac{\psi(z+2p)}{\psi(z+p)} = \frac{\psi(z+3p)}{\psi(z+2p)} = \dots = \frac{\psi(z+np)}{\psi(z+(n-1)p)} = C = e^{-\gamma p}, \forall n \tag{3.2.2}$$

Recursively, it can be found from (3.2.2) that

$$\psi(z+np) = C^n \psi(z) = e^{-\gamma np}\psi(z), \quad \forall n \tag{3.2.3}$$

This mathematical relation represents the periodic boundary conditions predominating in a periodic structure.
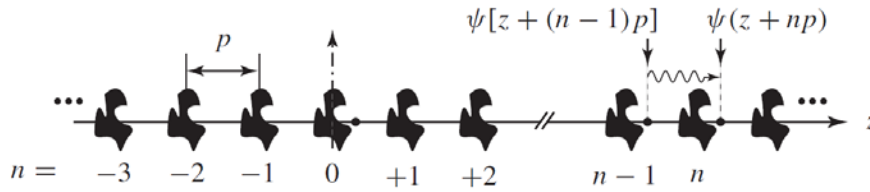
Figure 3.3: Arbitrary periodic infinite structure. Reproduced from [Caloz and Itoh, 2006]

A periodic function can be defined based on previous relations, so that it can be expressed via a Fourier series expansion:

$$P(z) = e^{\gamma z}\psi(z) \tag{3.2.4}$$

$$P(z+p) = e^{\gamma z}e^{\gamma p}\psi(z+d) = e^{\gamma z}e^{\gamma p}e^{-\gamma p}\psi(z) = e^{\gamma z}\psi(z) = P(z) \tag{3.2.5}$$

Similarly, $$P(z+np) = P(z) \tag{3.2.6}$$

$$P(z) = \sum_{n=-\infty}^{\infty} a_n e^{-j\frac{2\pi n}{p}z} \tag{3.2.7}$$

where a_n represents the Fourier series expansion coefficients. The wave equation can be obtained from equations (3.2.4) and (3.2.7), thus

$$P(z) = \sum_{n=-\infty}^{\infty} a_n e^{-j\frac{2\pi n}{p}z} = e^{\alpha(\omega)z + j\beta(\omega)z}\psi(z)$$

$$\psi(z) = e^{-\alpha(\omega)z} \sum_{n=-\infty}^{\infty} a_n e^{-j\left(\beta(\omega)+\frac{2\pi n}{p}\right)z} = e^{-\alpha(\omega)z} \sum_{n=-\infty}^{\infty} a_n e^{-j\beta_n(\omega)z} \tag{3.2.8}$$

9

where
$$\beta_n(\omega) = \beta(\omega) + \frac{2\pi n}{p} \qquad (3.2.9)$$

which represents the *n-th spatial Floquet harmonic* of the wave. The *Bloch-Floquet theorem* states that the wave in a periodic structure consists of the superposition of an infinite number of plane waves, called space harmonics or Bloch-Floquet's waves. The wave $\beta_0 = \beta(\omega)$ is called the fundamental, whereas the waves β_n with *n < 0* and *n > 0* are called the negative and positive space harmonics, respectively. [Oliner, 2003]

Consider now that a unit-cell of the arbitrary infinite periodic structure is modeled as a two-port network, characterized by its ABCD parameter matrix, as depicted in Fig 3.4.
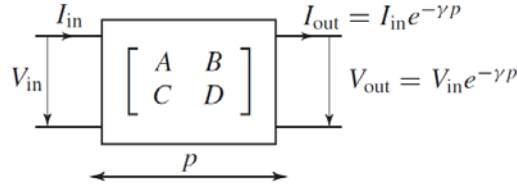
Figure 3.4: Application of PBCs to a two-port network unit cell. Reproduced from [Caloz and Itoh, 2006]

By imposing periodic boundary conditions, the output current and voltage variables differ from the input current and voltage only by a complex exponential constant. The propagation and attenuation constants can be obtained from the following mathematical expression [Pozar, 2005]:

$$\begin{bmatrix} V_{in} \\ I_{in} \end{bmatrix} = \begin{bmatrix} A & B \\ C & D \end{bmatrix}\begin{bmatrix} V_{out} \\ I_{out} \end{bmatrix} = \begin{bmatrix} A & B \\ C & D \end{bmatrix}\begin{bmatrix} V_{in}e^{-\gamma p} \\ I_{in}e^{-\gamma p} \end{bmatrix}$$

$$\begin{bmatrix} A & B \\ C & D \end{bmatrix}\begin{bmatrix} V_{in} \\ I_{in} \end{bmatrix} = e^{\gamma p}\begin{bmatrix} V_{in} \\ I_{in} \end{bmatrix} \qquad (3.2.10)$$

$$\begin{bmatrix} A-e^{\gamma p} & B \\ C & D-e^{\gamma p} \end{bmatrix}\begin{bmatrix} V_{in} \\ I_{in} \end{bmatrix} = \begin{bmatrix} 0 \\ 0 \end{bmatrix}$$

If the two-port network is reciprocal, then the complex propagation constant may be computed by [Pozar, 2005]

$$AD + e^{2\gamma p} - (A+D)e^{\gamma p} - BC = 0 \quad \Rightarrow \quad \cosh(\gamma p) = \frac{A+D}{2} \qquad (3.2.11)$$

Another important parameter is the Bloch impedance, which is the (constant) ratio between the voltage and current at the terminals of the unit-cell at any *k*-th point of the whole structure. [Pozar, 2005]

$$Z_B = \frac{V_k}{I_k} = \frac{V_{in}}{I_{in}} = \frac{-B}{A-e^{\gamma p}} \qquad (3.2.12)$$

10

If the two-port network is reciprocal, then the Bloch impedance may be computed by [Pozar, 2005]

$$Z_B^{\pm} = \frac{-2B}{2A - A - D \mp \sqrt{(A+D)^2 - 4}} \quad \Rightarrow \quad Z_B^{\pm} = \frac{\pm B}{\sqrt{A^2 - 1}} = \pm\sqrt{\frac{B}{C}} \tag{3.2.13}$$

In some occasions, it may be difficult to express the unit cell transmission parameters in terms of voltages and currents. Often, a more suitable description would be in terms of reflected and incident waves, where the unit cell characterization is given by the scattering parameter matrix [Pozar, 2005]. The ABCD matrix is related to the scattering parameter matrix by (3.2.14), considering that port impedances are purely real [Jarry and Beneat, 2008]

$$\begin{bmatrix} A & B \\ C & D \end{bmatrix} = \begin{bmatrix} \sqrt{\dfrac{R_G}{R_L}} \dfrac{(1+S_{11})(1-S_{22})+S_{21}S_{12}}{2S_{21}} & \sqrt{R_G R_L} \dfrac{(1+S_{11})(1+S_{22})-S_{21}S_{12}}{2S_{21}} \\ \dfrac{1}{\sqrt{R_G R_L}} \dfrac{(1-S_{11})(1-S_{22})-S_{21}S_{12}}{2S_{21}} & \sqrt{\dfrac{R_L}{R_G}} \dfrac{(1-S_{11})(1+S_{22})+S_{21}S_{12}}{2S_{21}} \end{bmatrix} \tag{3.2.14}$$

3.3. Control of aperture illumination for sidelobe reduction

The control of the aperture illumination is not exclusive for leaky wave antennas, in fact is widely used for all types of antennas. It can be used to improve illumination efficiency (hence an increase in directivity) as well as to reduce side lobes to a certain level, since side lobes make an antenna inefficient in terms of radiating power in a given range of undesired angles.

This concept is absolutely valid for any aperture-type antenna and antenna arrays. The process for reducing the side lobes in a leaky wave antenna is described next: the starting point is the specification of the desired radiation pattern; this way, the sidelobe level is fixed from the very beginning. Then, the corresponding aperture distribution is obtained by standard antenna techniques. After the aperture illumination is determined, the leakage distribution $\alpha(x)$, which is now a function of position along the antenna length, is calculated along the antenna from (3.3.7). Finally, the last step is to compute the tapered geometry that provides this $\alpha(x)$ distribution. In this final step is crucial that β/k_0 remain constant all along the antenna length, since radiation should only occur at a fixed angle.

The mathematical procedure to extract $\alpha(x)$ from the aperture illumination is described next [Oliner, 2003]:

The power distribution along the antenna can be expressed in the form

$$P(x) = P(0)e^{-2\int_0^x \alpha(\zeta)d\zeta}. \tag{3.3.1}$$

where ξ represents the integration variable along the longitudinal direction. Upon differentiation

$$-\frac{dP(x)}{dx} = 2\alpha(x)P(x). \tag{3.3.2}$$

$$I(x) = A(x)e^{-j\beta x} \tag{3.3.3}$$

Now, suppose that the desired aperture illumination (which would achieve the specified radiation pattern) is defined as (3.3.3). Also, (3.3.2) may be written alternatively

$$-\frac{dP(x)}{dx} = c|A(x)|^2 \tag{3.3.4}$$

where c is a constant of proportionality. From (3.3.2) and (3.3.4) is evident that

$$2\alpha(x) = \frac{c|A(x)|^2}{P(x)} \tag{3.3.5}$$

Upon integration of (3.3.5), and after some straightforward manipulations for eliminating c, the expression obtained for $\alpha(x)$ is:

$$c\int_0^L |A(\zeta)|^2 \, d\zeta = P(0) - P(L)$$

$$c\int_0^x |A(\zeta)|^2 \, d\zeta = P(0) - P(x) \tag{3.3.6}$$

$$\alpha(x) = \frac{\frac{1}{2}|A(x)|^2}{\frac{1}{\eta}\int_0^L |A(\zeta)|^2 \, d\zeta - \int_0^x |A(\zeta)|^2 \, d\zeta} \tag{3.3.7}$$

From (3.3.7), it can be seen that the leakage distribution depends on the desired aperture illumination and on antenna parameters such as radiation efficiency and total length. For antennas with a very high radiation efficiency (up to 95%), the denominator in (3.3.7) tends to zero, which constitute very high values of leakage factor for points close to the end of the antenna. Therefore, in order to avoid this high (and in occasions impractical) values, the radiation efficiency must be fixed to a more suitable value, around 85-90%. A similar situation would occur if the antenna length is not sufficiently long for a given radiation efficiency: large values of leakage would appear at points near the end of the antenna, since more power has to be leaked out there in order to satisfy the given efficiency value.

On the other hand, the reverse procedure for a tapered design is also very interesting and starts from a leakage factor distribution (obtained from a tapered geometry) with the purpose of calculating the radiation pattern via the resultant normalized aperture illumination. After some straightforward manipulations on (3.3.5) and (3.3.1):

$$c\left|A'(x)\right|^2 = \frac{dP(x)}{dx} = -2\alpha(x)P(x)$$

$$P(x) = P(0)e^{-2\int_0^x \alpha(\zeta)d\zeta}$$

$$\Rightarrow \left|A'(x)\right| = C_1\sqrt{\alpha(x)}\,e^{-\int_0^x \alpha(\zeta)d\zeta} \qquad (3.3.8)$$

where C_1 is a constant of proportionality. From (3.3.8), the shape of the aperture illumination can be computed correctly; nevertheless the exact amplitude cannot be computed mainly due to the proportionality constant in (3.3.4). Despite of this, expression (3.3.7) suggests that any constant multiplying the illumination function is not relevant for the calculation of the needed leakage factor, since both numerator and denominator in the formula are multiplied by it. The aperture illumination is then usually normalized in values within the range [0,1]. In this case

$$\left|A(x)\right| = \frac{\left|A'(x)\right|}{\max\left\{\left|A'(x)\right|\right\}} \qquad (3.3.9)$$

Normalized radiation pattern can be obtained directly from Fourier transform of the normalized resultant aperture illumination by [Link 1]

$$E_\theta = j\frac{e^{-jkr}}{2\lambda r}\cos\phi\left(\frac{\eta}{Z_0}\cos\theta + 1\right)\iint_{s'} E(x',y')e^{jk_x x}e^{jk_y y}\,dx'dy'$$

$$E_\phi = -j\frac{e^{-jkr}}{2\lambda r}\sin\phi\left(\frac{\eta}{Z_0} + \cos\theta\right)\iint_{s'} E(x',y')e^{jk_x x}e^{jk_y y}\,dx'dy' \qquad (3.3.10)$$

Considering that the electric field is polarized horizontally on the aperture.
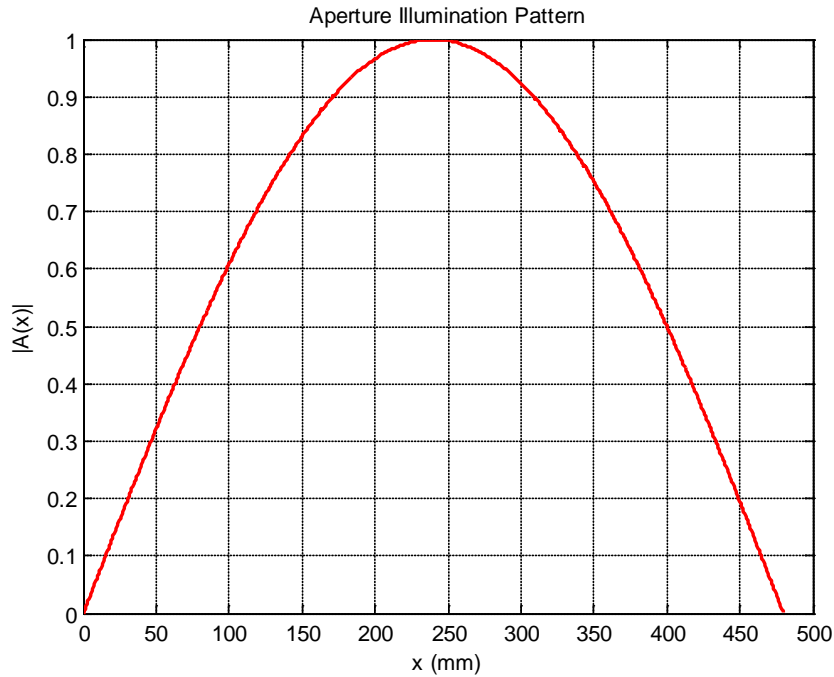
Figure 3.5: Desired aperture illumination. f = 5 GHz – L = $8\lambda_0$ = 480 mm – η = 90%.

In order to illustrate this procedure, formulas (3.3.7), (3.3.8), (3.3.9) and (3.3.10) have been implemented in a MATLAB routine. Let us consider an example based on the cosine aperture illumination, a radiation efficiency of 90%, an antenna length $8\lambda_0$ long and the operating frequency 5GHz. The main beam angle is set to 30º. Fig. 3.5 presents the desired aperture illumination.
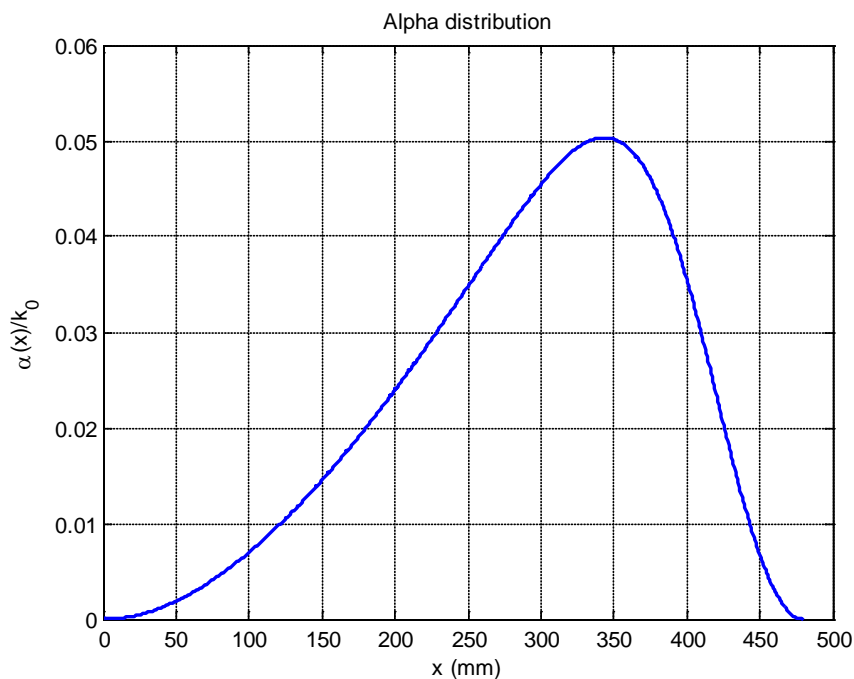

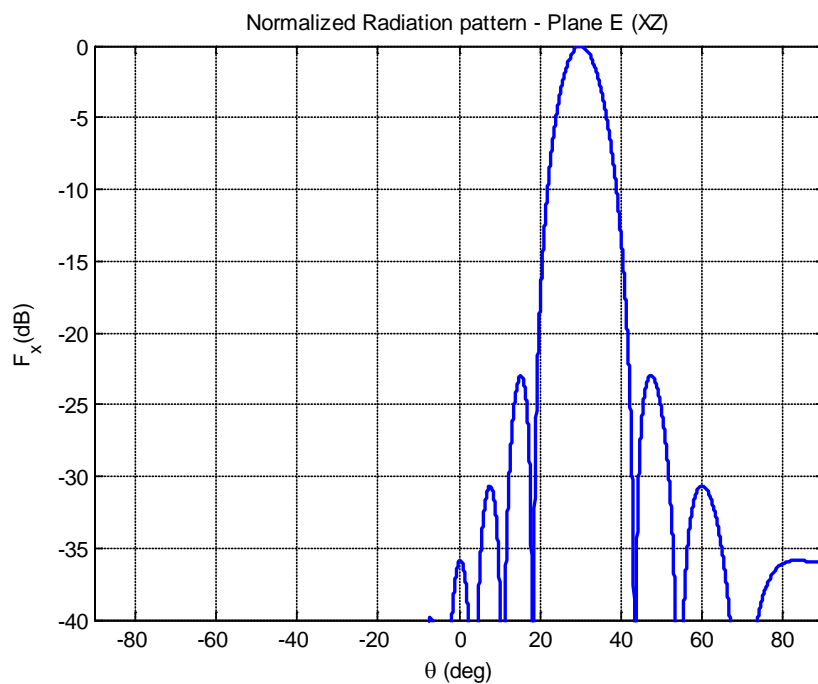Figure 3.6: Resultant leakage factor distribution. f = 5 GHz – $L = 8\lambda_0$ = 480 mm – η = 90%.

Figure 3.7: Normalized radiation pattern. f = 5 GHz – $L = 8\lambda_0$ = 480 mm – η = 90%.

The desired aperture illumination patter, cosine-type, can be achieved by the leakage factor distribution presented in Fig 3.6. It is important to notice the variation of leakage factor versus the position along the antenna: at the beginning, radiation losses are fairly small and increases gradually as the wave travels towards the end of the antenna. After reaching its maximum point, the leakage rate decreases almost abruptly. Thus, less power is radiated at the beginning, so that a considerable part of it can reach farther parts of the antenna and be radiated in a greater degree. The remaining power that reaches the end of the antenna is quite small and goes to the load. Radiation pattern is shown in Fig 3.4. The sidelobe level achieved is -23 dB; therefore, less than 0.5% of the radiated power is wasted in undesired directions.

It is supposed that the remaining power at the very end of the antenna goes to a matched load. Therefore, the radiation pattern only considers the wave traveling from the beginning of the antenna, but does not consider the reflected wave at the load (since it is matched). Fig. 3.7 shows the obtained normalized radiation pattern.

Finally, the required leakage distribution to reduce the side lobes to a determined level must be provided by controlled modifications in the geometry of the antenna, once the relationship (hence the control) of the attenuation constant and geometrical parameters has been established (via theoretical formulation or full-wave simulations). In particular, for leaky wave antennas this geometry variation must not affect the longitudinal propagation constant β, as all the individual leakage contributions of the leaky wave antenna have to be pointing at the same angle.

In some cases, it may be impractical to obtain some of the required leakage distribution values, mostly due to geometry constraints; and some constraints must be imposed in order to ensure a proper behavior in a determined waveguiding structure. Furthermore, manufacturing processes often imposes a limitation in the election of the size of elements in a given geometry, such as diameter of via holes or gap slots in a metalized dielectric substrate. Undoubtedly, these constraints affect unavoidably the leakage factor, since it will be ranging over an interval $[\alpha_{min}, \alpha_{max}]$, which may be insufficient for succeeding in a specific sidelobe reduction design procedure.

The effect of these geometrical constraints can be included in the resultant attenuation constant distribution and thus, the reverse procedure can be carried out by applying (3.3.8) and (3.3.9). Effects such as discretization and α_{min}-truncating are revised next.

Discretization

In case of periodic structures comprising a finite number N of unit cells, the attenuation constant distribution is not continuous; it is a sampled version of the original required distribution. Fig. 3.8 illustrates discretized distributions for a different number of unit-cells. Notice that unit-cells required must have a larger length as its number decreases, in order to satisfy a fixed antenna length. Fig. 3.9 shows the resultant aperture illumination for the aforementioned cases. It can be seen that the obtained pattern has pronounced and sharp edges as the number of unit-cells decreases. Nevertheless, the obtained shape is still similar to the desired one. The normalized radiation patterns can be found in Fig. 3.10. As

can be seen, the side lobe level remains practically unaffected. Note that side lobes far from the main beam present a considerable increase in amplitude, but they are still smaller than side lobes next to the main beam. Therefore, the sidelobe level is not affected by discretization, even for poorly discretized distributions.
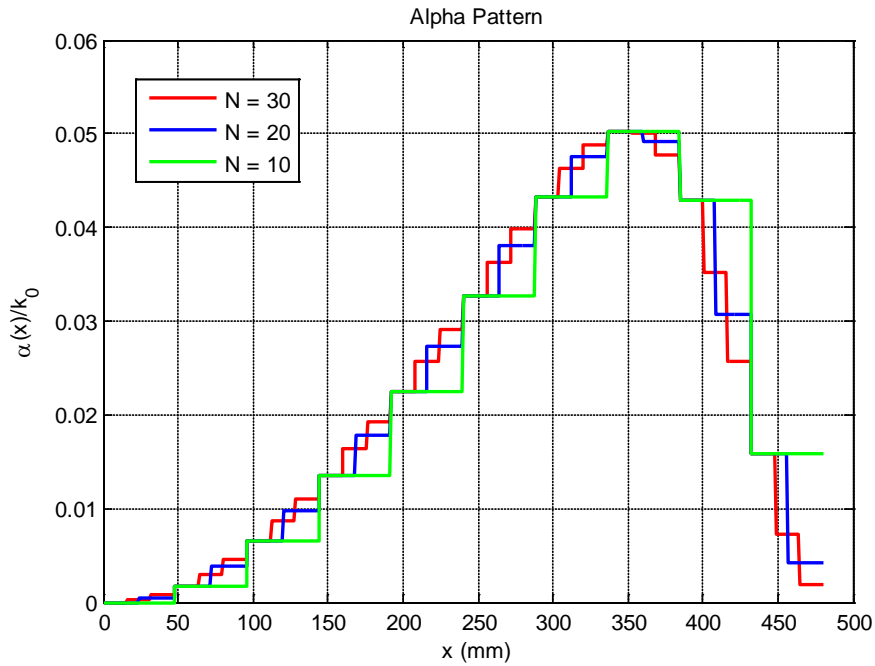

Figure 3.8: Base leakage factor distribution. f = 5 GHz – L = $8\lambda_0$ = 480 mm – η = 90%.
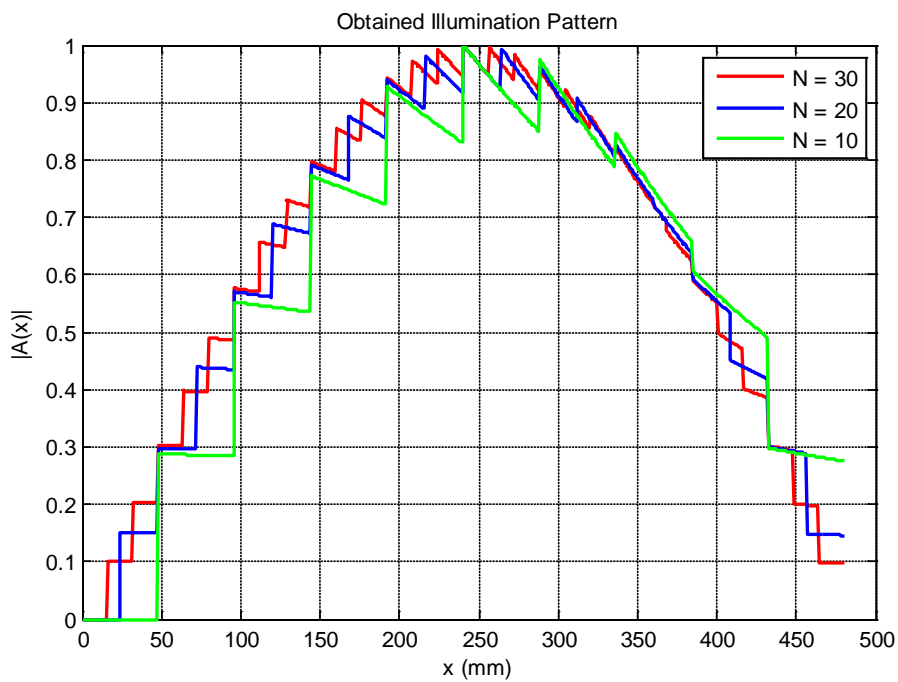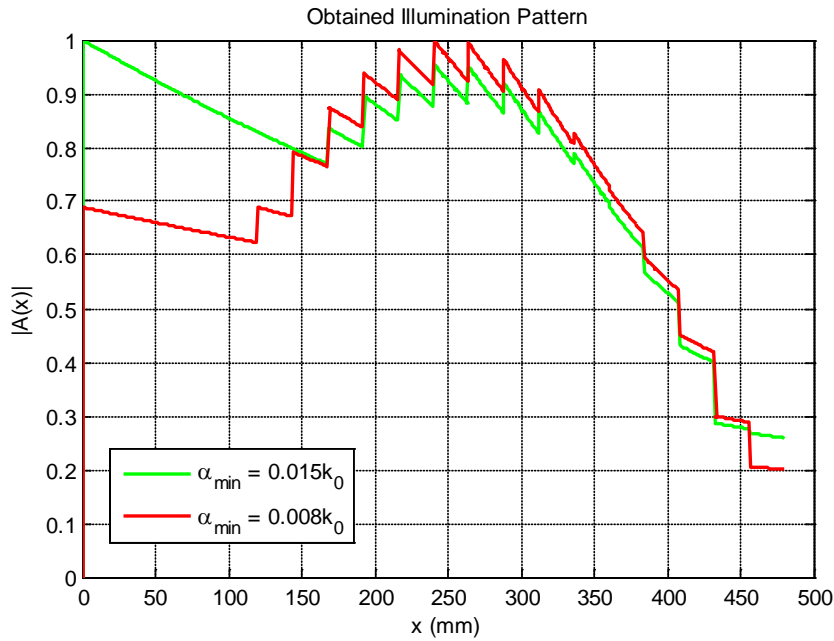

Figure 3.9: Resultant aperture illumination. f = 5 GHz – L = $8\lambda_0$ = 480 mm – η = 90%.
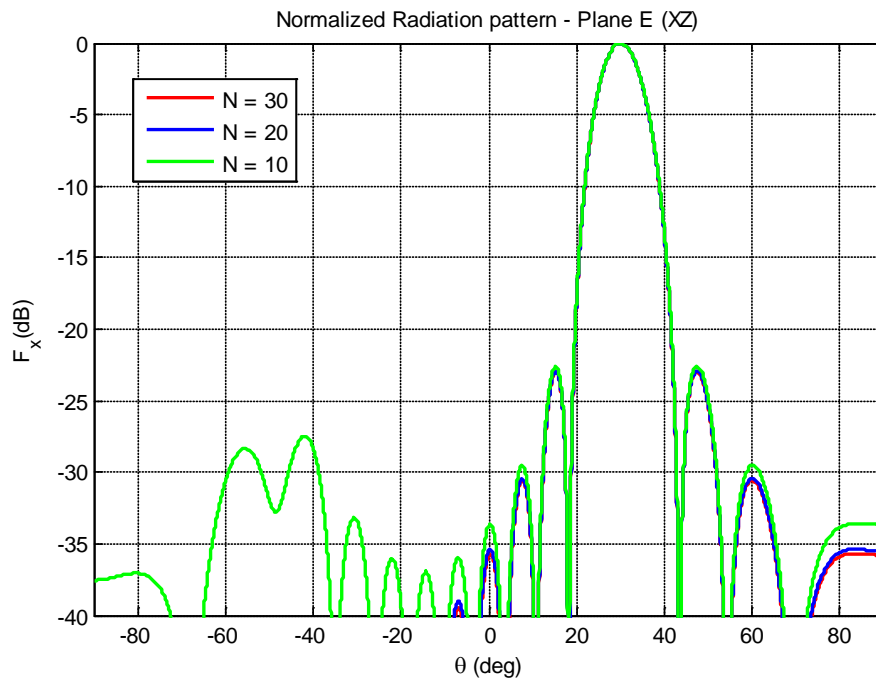
Figure 3.10: Normalized radiation pattern. f = 5 GHz – $L = 8\lambda_0$ = 480 mm – η = 90%.

α_{min}-truncating

In the truncated-distribution scenarios, some of the required values of leakage factor cannot be achieved after geometry modifications, considering specified constraints; usually, small values are difficult to obtain.
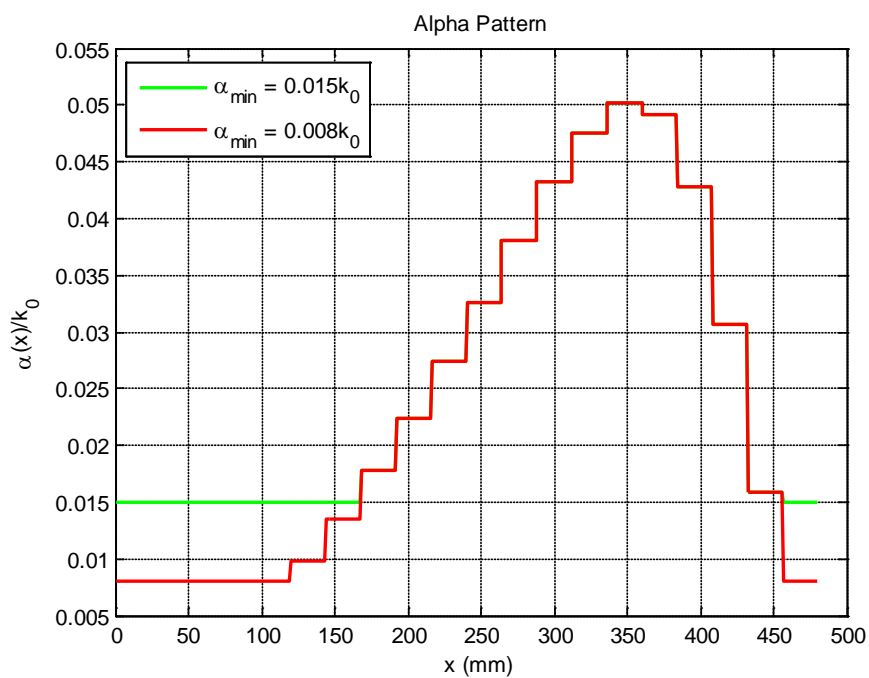
Figure 3.11: Base leakage factor distribution. f = 5 GHz – $L = 8\lambda_0$ = 480 mm – η = 90%.

Whether the truncating is done by setting to zero or setting to α_{min} all the unreachable values, this abrupt variation in the base distribution may affect considerably both the aperture illumination and the sidelobe level. Fig. 3.11 depicts an example of a truncated leakage factor distribution. In Fig. 3.12 are shown the resultant aperture illumination for hard-truncated and soft-truncated leakage distribution, respectively.

Figure 3.12: Resultant aperture illumination. f = 5 GHz – L = $8\lambda_0$ = 480 mm – η = 90%.
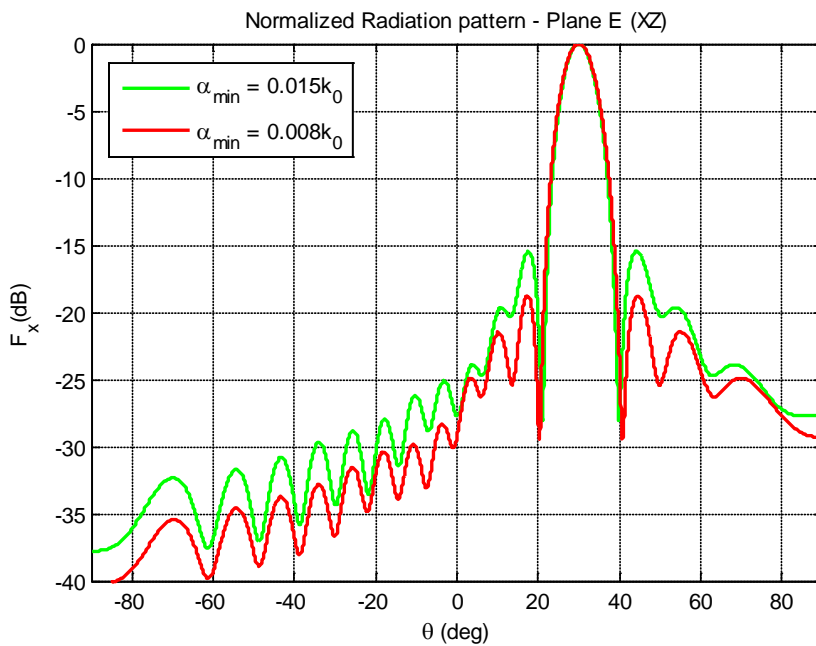
Figure 3.13: Normalized radiation pattern. f = 5 GHz – L = $8\lambda_0$ = 480 mm – η = 90%.

It can be seen that the desired cosine pattern has been greatly degenerated at the beginning. This is because the antenna is radiating more power than needed at the beginning, with an invariant attenuation constant over this part of the antenna. Fig. 3.13

presents the radiation pattern in two different scenarios. It can be seen that, the higher the minimum leakage factor value is (related to the maximum leakage factor value), the higher the sidelobe level gets. This is definitely an unfavorable situation, because sidelobe reduction depends strongly on the minimum achievable value. As can be seen, sidelobe level changed from -23 dB to -19 dB (red curve) or -15 dB (green curve).
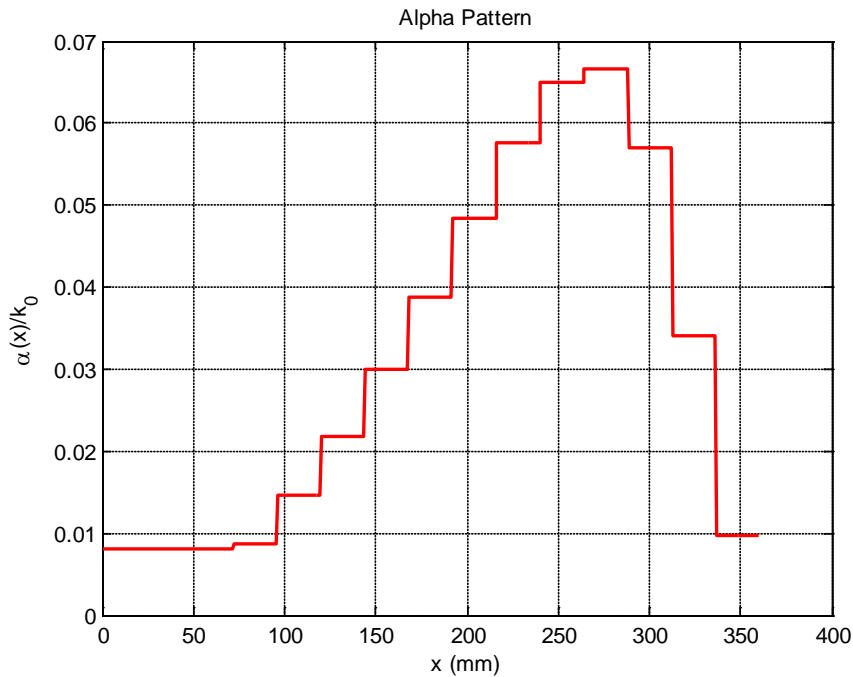

Figure 3.14: Base leakage factor distribution. f = 5 GHz – L = $6\lambda_0$ = 360 mm – η = 90%.
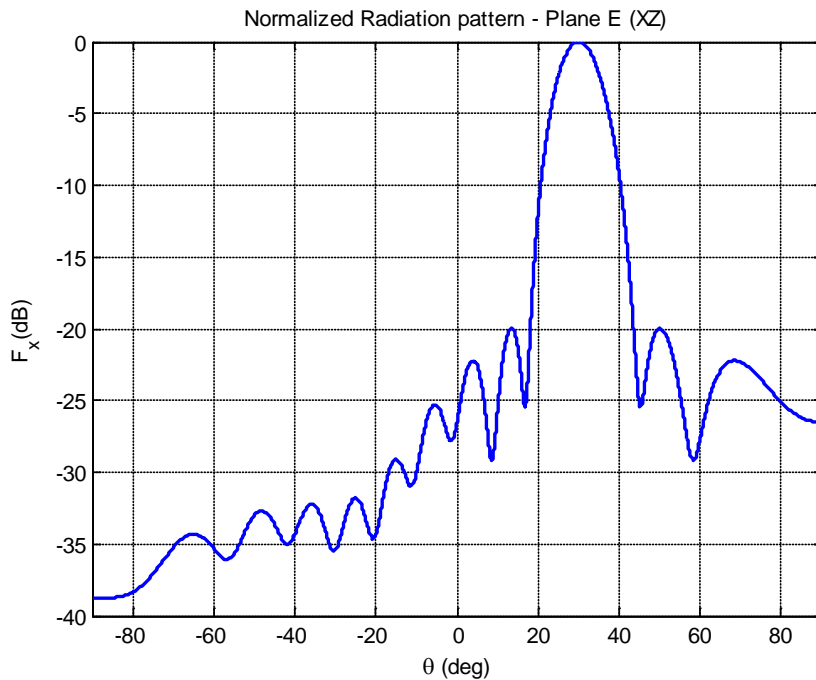
Figure 3.15: Normalized radiation pattern. f = 5 GHz – L = $6\lambda_0$ = 360 mm – η = 90%.

It is known that invariant attenuation constant along the entire antenna leads to high side lobe levels in the radiation pattern. Hence, if the antenna has a large radiative section with a constant leakage rate, as in the hard-truncated case, side lobes are going to increase their levels, and vice versa, a smaller radiative section with a constant leakage rate leads to a decrease in side lobe levels. A possible solution would be to reduce the antenna length, maintaining the same radiation efficiency, or even reducing it slightly. Thus, in order to satisfy the efficiency condition, the required attenuation constant has to increase accordingly. Now, the smallest value of α would be smaller compared to the new largest value needed of α. However, notice that reducing the length of the antenna implies also a reduction in the number of unit cells, and consequently, a small degradation in the resultant aperture illumination, as described before.

For instance, by reducing the antenna length to $6\lambda_0$ as presented in Fig 3.14, the difference between the minimum and maximum achievable α's is greater. In Fig 3.15, radiation pattern shows that side lobes amplitude have been reduced up to -20 dB.

LWA at microwave frequencies: CRLH-LWA

4.1. Introduction to metamaterials

Electromagnetic metamaterials can be defined as artificial effectively homogeneous electromagnetic structures with unusual properties not readily available in nature [Caloz and Itoh, 2006]. In conventional materials, propagation of electromagnetic waves exhibits parallel phase and group velocities, which means that the phase and the Poynting vectors are collinear and have the same direction. The vectors related to the electric field, magnetic field and phase constant constitute the so-called right-handed triad. However, the speculation of the existence of substances with simultaneous negative dielectric permittivity and magnetic permeability, presented by the soviet physicist V. Veselago in 1967, suggested that wave propagation with antiparallel phase and group velocities could occur in these media, in contrast with well-known materials available in nature. Therefore, the vectors involved in this case would constitute a left-handed triad. Several phenomena and properties related to these substances, such as negative refraction at the interface between a RH and a LH medium and reversal Doppler Effect, have been described and explained, among others.

30 years from Veselago's publication, british physicist J. B. Pendry detailed how to obtain macroscopic negative permeability or permittivity (separately), by arranging regular right-handed materials such as split ring resonators (SRR) or parallel wires in a periodical fashion, respectively, as depicted in Fig. 4.1.
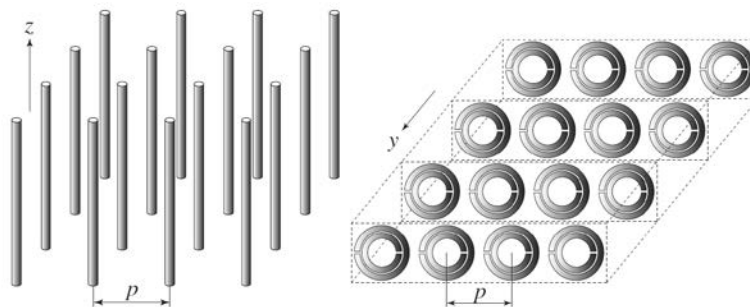
Figure 4.1: First negative-ε/positive-μ and positive-ε/negative-μ MTM, constituted only by standard metals and dielectrics, proposed by Pendry. From [Pendry et al, 1999].

Figure 4.2: First experimental LH structures, constituted of TWs and SRRs. Reproduced from [Smith et al, 2000] and [Shelby et al, 2001]

Soon after, an artificial effective homogeneous structure was proposed by D. Smith [Smith et al], [Shelby et al], inspired on Pendry's work, combining both type of periodical loading simultaneously to achieve both negative permeability and permittivity over a specific frequency range. Fig 4.2 depicts the first experimental demonstration of LH materials.

Planar metamaterials were introduced one year after, based on the periodical loading of a host transmission line with electrically small and closely spaced series capacitances and shunt inductances, providing a practical implementation of electromagnetic metamaterials. [Caloz et al., 2002], [Iyer and Eleftheriades, 2002].

The circuit model of a unit cell related to a purely left-handed transmission line consists of a simple series capacitance and a shunt inductance, and it provides anti-parallel phase and group velocities [Caloz and Itoh, 2005]. However, as the wave propagates along the structure, the associated voltages and currents induce other effects, being manifested by a series inductance and a shunt capacitance. Therefore, a purely LH structure does not physically exist, since a LH structure as defined before, intrinsically includes the contributions of two additional elements.
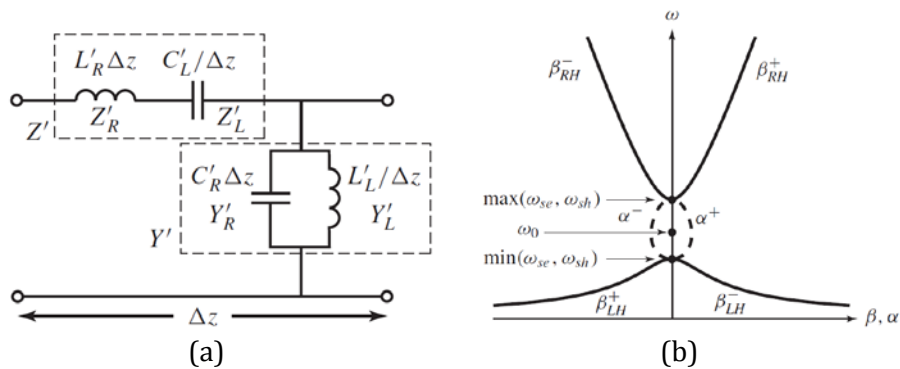

Fig. 4.3: a) CRLH unit-cell LC model. b) Complex propagation constant in unbalanced CRLH TL.

In order to consider these additional effects, the concept of composite right/left-handed transmission lines (also called negative-refraction TL) was introduced in [Caloz and Itoh, 2003], [Caloz and Itoh, 2006]], [Iyer and Eleftheriades, 2002]. Fig. 4.3 (a) shows the CRLH unit-cell LC model, where sub indexes R and L denote right-handed and left-handed, respectively. At low frequencies, right-handed immitances tend to zero, leading to an

equivalent pure LH TL ($L_R = C_R = 0$), with antiparallel phase and group velocities and a high-pass filter behavior. At high frequencies, the situation inverts, so that left-handed immitances tend to zero, leading to an equivalent pure RH TL ($L_L = C_L = 0$) with parallel phase and group velocities and a low-pass filter behavior, since RH immitances predominate. At all other frequencies, the transmission characteristic depend on the combination of RH and LH contributions [Caloz and Itoh, 2006].

In general, a frequency bandgap exists between the LH and RH behaviors, which leads to an unbalanced structure, as illustrated in Fig. 4.3 (b). Nevertheless, if the shunt and series resonances occur at the same frequency, then this bandgap disappears. Furthermore, a smooth transition between both behaviors replaces this gap and an infinite-wavelength appears at the transition frequency. In unbalanced cases, wave propagation does not occur due to a zero-group velocity over that frequency range, whereas in balanced cases, wave propagation does occur because of a non-zero group velocity.

Useful mathematical expressions for determining the complex propagation constant and Bloch impedance, considering that the unit cell length of a CRLH TL is very small compared to the guided wavelength are listed next [Caloz and Itoh, 2006]:

$$\gamma = \sqrt{Z'Y'} \qquad\qquad Z_B = \sqrt{\frac{Z'}{Y'}} \qquad\qquad (4.1.1)$$

$$Z' = j\left(\omega L_R - \frac{1}{\omega C_L}\right) \qquad\qquad Y' = j\left(\omega C_R - \frac{1}{\omega L_L}\right) \qquad\qquad (4.1.2)$$

$$Z_B = \sqrt{\frac{L_R}{C_R}\left(\frac{\omega_{se}^2 - \omega^2}{\omega_{sh}^2 - \omega^2}\right)} \qquad\qquad (4.1.3)$$

$$\gamma = \alpha + j\beta = js(\omega)\sqrt{\left(\frac{\omega}{\omega_R}\right)^2 + \left(\frac{\omega_L}{\omega}\right)^2 - \omega_L^2\left(\frac{1}{\omega_{se}^2} + \frac{1}{\omega_{sh}^2}\right)} \qquad\qquad (4.1.4)$$

where

$$s(\omega) = \begin{cases} -1, & \omega < \min(\omega_{se}, \omega_{sh}) \quad \text{LH range} \\ +1, & \omega > \max(\omega_{se}, \omega_{sh}) \quad \text{RH range} \end{cases} \qquad\qquad (4.1.5)$$

Also, resonant frequencies have been defined conveniently as

$$\omega_R = \frac{1}{\sqrt{L_R C_R}}, \quad \omega_L = \frac{1}{\sqrt{L_L C_L}}, \quad \omega_{se} = \frac{1}{\sqrt{L_R C_L}}, \quad \omega_{sh} = \frac{1}{\sqrt{L_L C_R}} \qquad\qquad (4.1.6)$$

As commented previously, the unit cell length must be much smaller than the guided wavelength, so that a propagating wave sees an effectively homogeneous media.

4.2. CRLH-LWA

A very interesting feature of CRLH TLs is that both LH and RH behaviors always penetrate the fast-wave region, enhancing therefore leaky wave applications, such as antennas, within this frequency band. In this case, and based on the theoretical fundamentals of LWAs, a CRLH-LWA can radiate at any angle from back-fire to end-fire directions (including broadside) using the fundamental spatial harmonic (n = 0), assuming beforehand that the structure is periodic, whereas in conventional LWAs, backward-to-forward frequency scanning is only achievable by using higher-order harmonics, usually the n = - 1.

Furthermore, broadside radiation can be achieved for balanced structures. From previous section, it is known that a frequency bandgap exists when the shunt and series resonances in the LC model of a unit cell do not occur at the same frequency; hence, an unbalanced CRLH-LWA, cannot radiate power at that direction since that frequency would correspond to a frequency in the afore mentioned gap, where the structure does not support wave propagation. If the unit cell is balanced, however, effective wave propagation takes place at the transition frequency and, as the wave is guided with a propagating constant less than the free-space wavenumber (fast-wave condition is satisfied), a radiative phenomenon is introduced. On the other hand, CRLH LWAs often present a reduction in the radiation efficiency at the broadside direction, due that a series and a shunt resistors are required to efficiently radiate at the broadside direction [Gómez Díaz et al, 2011c].
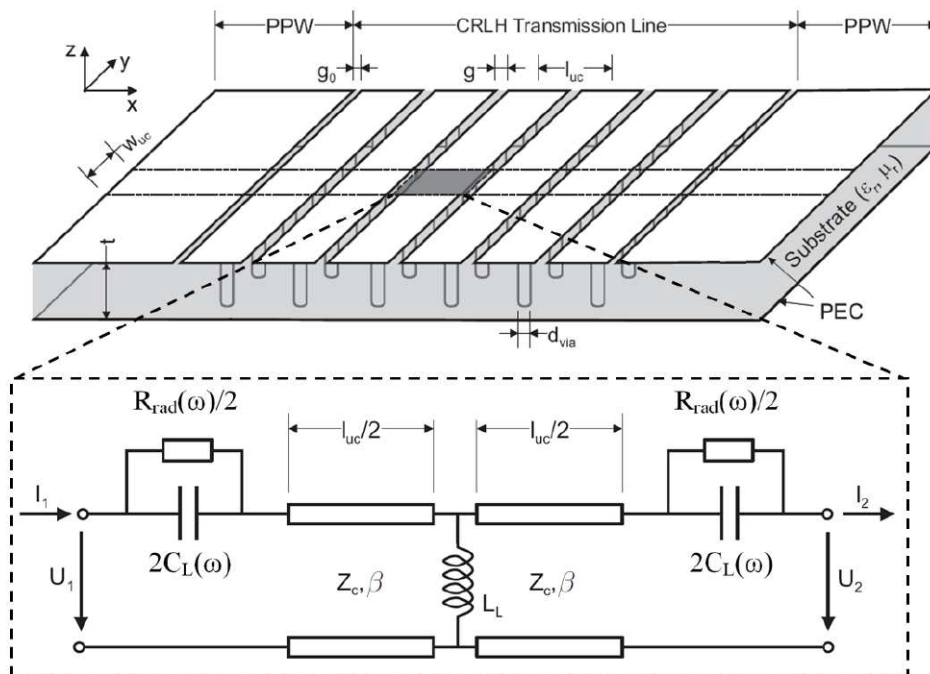

Figure 4.4: Topology of the LWA; TL model for a unit-cell. Reproduced from [Gómez Díaz et al, 2011a]

Fig.4.4 shows the base topology of the CRLH-LWA, as well as its proposed symmetrical unit-cell equivalent model for analysis [Gómez Díaz et al, 2011a]. This topology has been chosen over others due to the advantages it provides: the implemented antenna is

24

compact, simple and easy to manufacture. The structure is inherently two-dimensional; therefore, instead of obtaining a fan beam radiation pattern, the resultant radiation pattern type is a pencil beam. However, since effective wave propagation only occurs in one direction, there is only scanning capabilities in one plane, with a narrow beam in both planes, which is an advantage over other antenna topologies. It can be seen that a parallel-plate waveguide is used as the host transmission line, and the periodical loadings are cylindrical via-holes and slits oriented in the transverse direction. These slits, aside from providing a left-handed capacitance, provide an equivalent resistance related to the radiation losses as the waves propagates along the structure. Note that both elements are frequency dependent, thus presenting a dispersive behavior.

The antenna consists of a planar substrate layer of thickness t with homogeneous and isotropic materials characterized by relative permittivity ε_r and relative permeability μ_r. The structure is supposed to be finite in the X and Z directions, but infinitely periodical along the Y direction. According to the figure, the energy propagates in the X direction, and the effective wave propagation occurs in the XZ plane. The resulting antenna is inherently 2D, because the slots are periodically located along the longitudinal direction (X axis) but they are continuous in the transverse direction (Y axis). This antenna therefore radiates in a pencil beam with frequency-scanning capabilities in only one plane, since it does not support leaky wave propagation in the other direction.

The back side of the substrate is completely metalized. The front side, metalized as well, has a finite number of parallel and equidistant slots. The first and last slots have a width g_0, different from the other slots, which have a width g. This is because the first and last slots are used for matching the input/output ports, and do not have radiation purposes. The metal stripes in the front side, separated by the slots, are connected from their centers to the back side metallization by a rectangular grid of via holes with diameter d_{via} with a spacing of l_{uc} and w_{uc} in the X and Y directions, respectively. The vias and slots constitute the loading of the PPW (parallel-plate waveguide) host TL, and at the right frequency range, make the loaded section behaves as a CRLH TL.

Without the presence of any slot, the host TL loaded solely by the rectangular grid of via holes creates a wired medium (or artificial dielectric) [King et al, 1983], which exhibits very strong dispersive properties, similar to the ones observed in a hollow rectangular waveguide, including a cut-off frequency. Below cut-off, there is no propagation in the WM (wired medium) and above cut-off the WM supports RH propagation with an effective wave number along the x-direction that is always smaller than the free space wave number k_0.

Introducing the slots in the upper metallization has two effects. On the one hand, a coupling between the region above and the region inside the PPW is established, which facilitates leaky-wave radiation, provided that the real part of the CRLH TL effective wave number (k_{eff}) is smaller than the free space wave number, k_0. On the other hand, a CRLH TL is created which may support left-handed (LH) propagation below the WM cut-off frequency.

In this case the structure is balanced; therefore there will be a smooth transition from left-handed to right-handed frequency regions. However, as previously commented, even in

this case the antenna presents a reduction in the radiation efficiency at the broadside direction, due that are required a series and a shunt resistors to efficiently radiate at the broadside direction, and the PPW loading only provides a series resistor.

For balanced designs, a modal-based iterative method has been proposed [Gómez Díaz et al, 2011a] in order to reduce considerably the time to obtain a full characterization of the antenna, based on the geometrical parameters. Obtained results show a very good agreement between the proposed method and full-wave simulations from commercial software (HFSS/CST).

The first step is to design the base wired-medium, by setting WM's cut-off frequency. According to documentation on an extensive study of artificial dielectrics, the relationship between the geometrical parameters and the cut-off frequency is given by the following transcendental equation [King et al, 1983]:

$$kw_{uc} \tan\left(\frac{kw_{uc}}{2}\right) = \frac{\pi w_{uc}}{l_{uc} \ln\left(\frac{l_{uc}}{\pi d_{via}}\right)} \tag{4.2.1}$$

where
$$k = 2\pi f_{WM} \sqrt{\varepsilon_r \varepsilon_0 \mu_r \mu_0} \tag{4.2.2}$$

and w_{uc}, l_{uc} and d_{via} represent the width and length of the unit cell, and the diameter of the via holes. Thus, a specific value of cut-off frequency can be obtained by several sets of geometrical parameters, which adds flexibility at the time of designing the base WM.
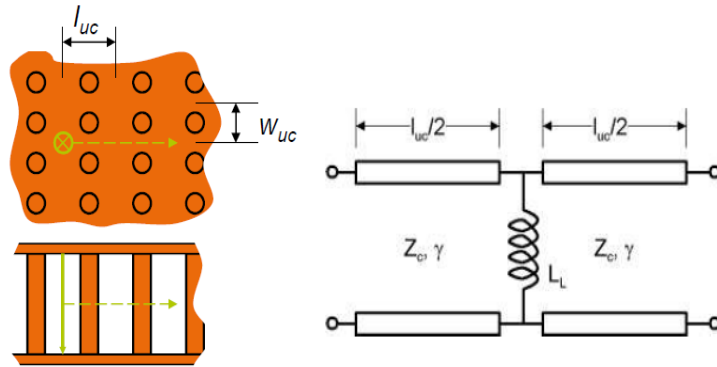
Figure 4.5: Wired medium: Geometry description and analytical model. Reproduced from [Bertuch, 2011]

The complex propagation constant of the wired medium can be obtained analytically, applying PBCs (chapter 3) in the TL model depicted in Fig. 4.5, considering that the host TL is a PPW, and is periodically loaded by an inductance (via hole). An example is illustrated in Fig. 4.6.

As can be seen, the fundamental spatial harmonic in the periodic waveguide is naturally fast and is completely located within the fast-wave region; furthermore, it presents a dispersive behavior similar to that of a hollow waveguide. This implies that there is no need to work with higher order harmonics since a CRLH LWA is achievable by using the fundamental harmonic. Also, if the CRLH TL is supposed to be balanced, the WM's cut-off

frequency can also be named 'transition frequency', because of the fact that it provides a smooth transition between the RH and LH frequency bands.
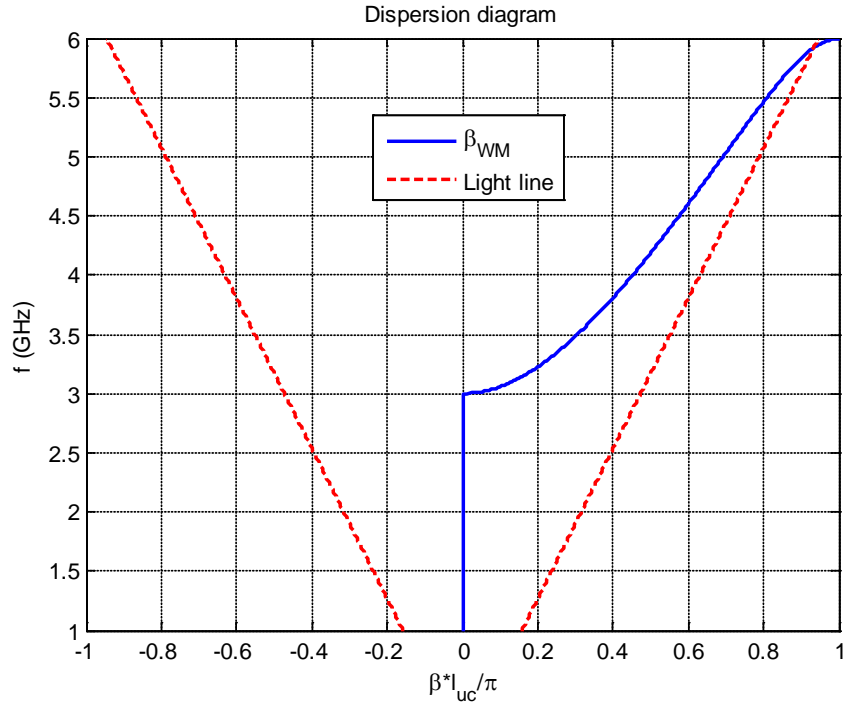

Figure 4.6: Dispersion diagram of a wired medium. Parameters: f_{WM} = 3 GHz, l_{uc} = 23.54 mm, w_{uc} = 23.54 mm, d_{via} = 1 mm, ε_r = 1.12 and t = 3.52 mm.
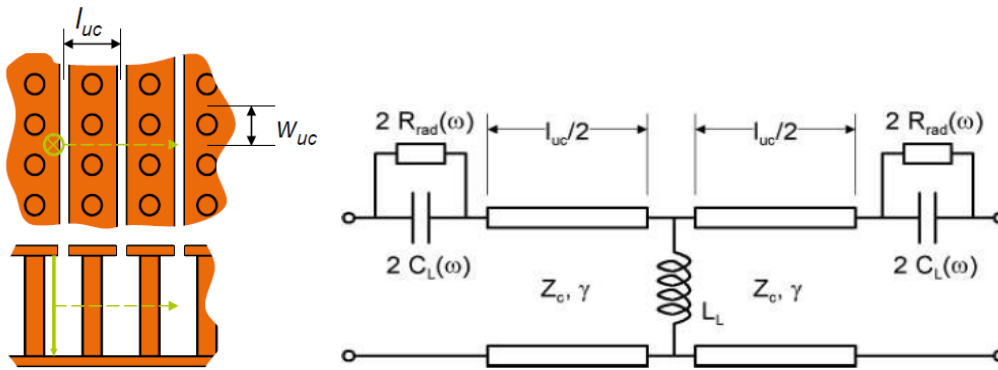

Figure 4.7: CRLH LWA: Geometry description and analytical model. Reproduced from [Bertuch, 2011]

Now, for an open and balanced structure, the geometry and analytical proposed model [Gómez Díaz et al, 2011a] are illustrated in Fig. 4.7. The CRLH TL is finally obtained after the periodical addition of the slots. The width of the slots, however, has to fulfill the balancing condition (both series and shunt resonances occur at the same frequency) in this case. The optimal width value to balance the structure is obtained by using a modal-based iterative method proposed in [Gómez Díaz et al, 2011a], which solves the electromagnetic problem in the interface air-dielectric by applying suitable boundary conditions. After this, all the required dimensions to fully analyze the structure are known, and the complex propagation constant, among other quantities, can be obtained with this

method. The dispersion diagram comparison of the WM and the CRLH LWA is shown in Fig. 4.8. The most symbolical difference is the appearance of a LH band, consequence of the added capacitive effect of the slots. Also, it can be seen that the fundamental harmonic has been perturbed as well, hence changing the dispersion diagram in the RH side.
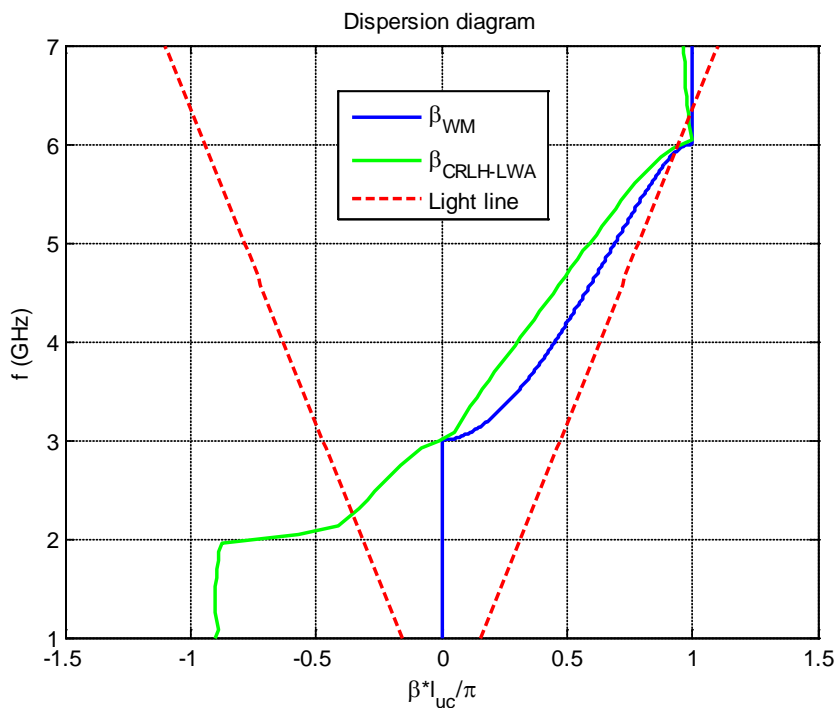
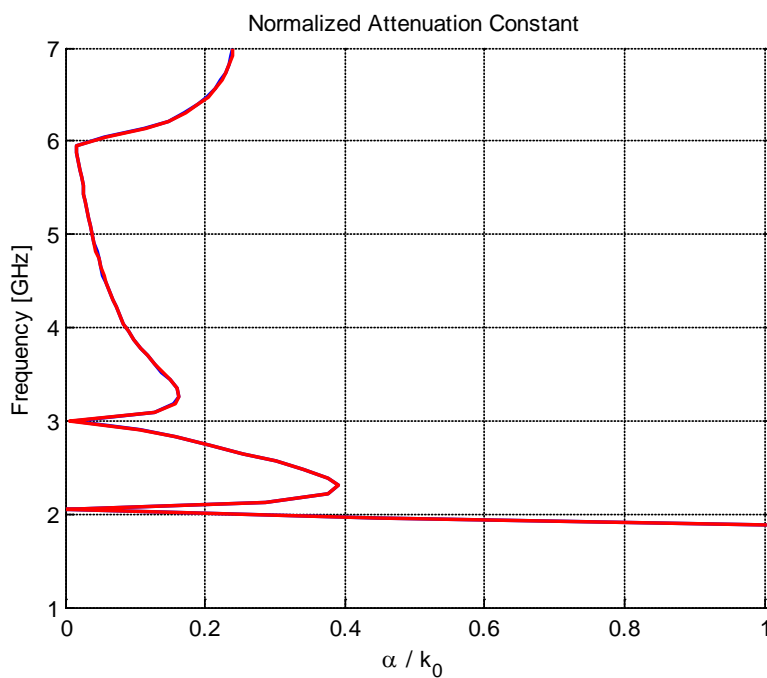Figure 4.8: CRLH dispersion diagram – comparison with WM.

Figure 4.9: Normalized attenuation constant.

The attenuation constant is obtained along with the propagation constant. It can be seen that near the transition frequency, the radiation losses reduces considerably due to the lack of a shunt resistance in the analytical model, because the PPW loading only provides a series resistance instead of both series and shunt [Gómez Díaz et al, 2011c]. The leakage factor is quite high in the LH region; this implies that the obtained radiation pattern for backward propagation will consist of a fat beam, since all the power is leaked at the beginning of the antenna. In contrast, the leakage factor is smaller in the RH region, and the radiation pattern will present a narrow main beam thus obtaining a higher directivity.
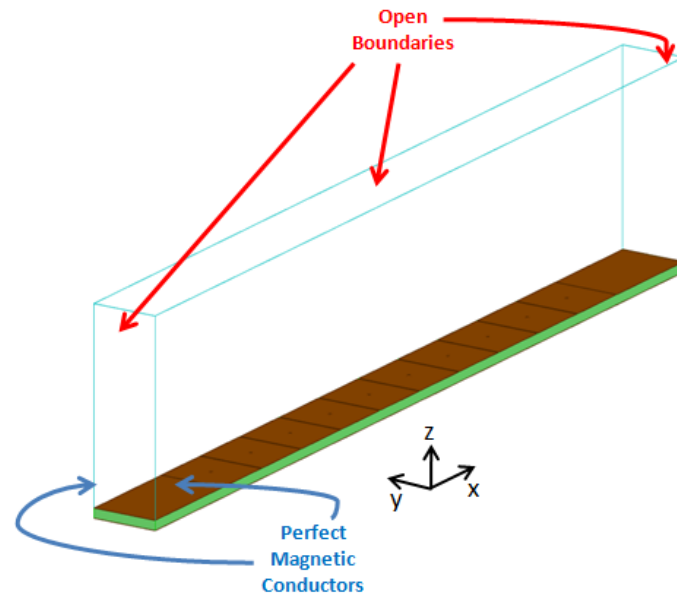
Figure 4.10: Geometry model for Full-wave simulation.
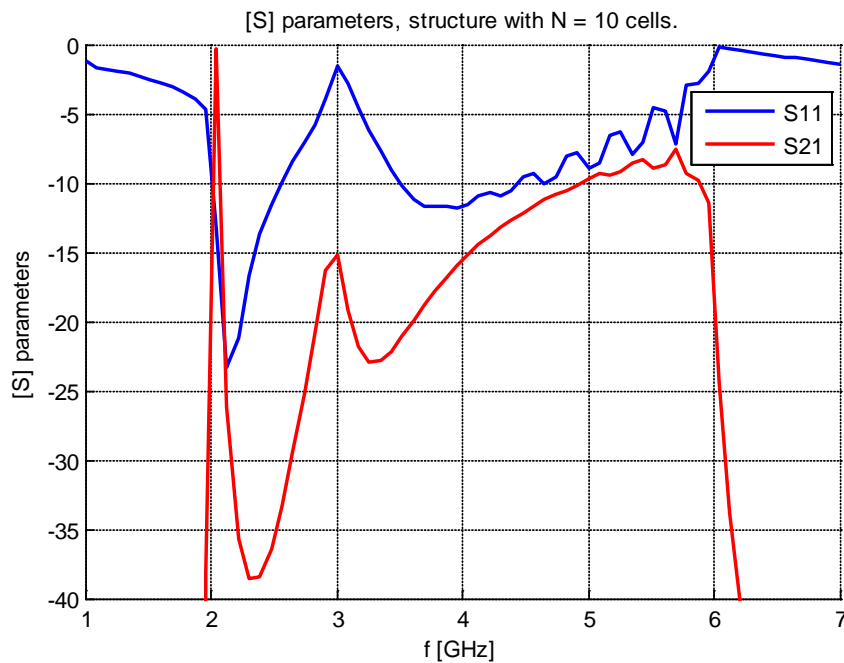
Figure 4.11: S - parameters.

Now, in order to obtain the scattering parameters and the radiation patterns at all frequencies, a single stripe composed of 10 unit-cells is used. It has to be noticed that the first and last slots do not have the same width as the other slots, and must accurately derived. This is because they are utilized to improve matching in the input/output ports. Note that these slots are responsible of the connection of the CRLH TL to the feeding TL.

The HFSS geometry model is depicted in Fig. 4.10; the types of boundary conditions applied to the side walls of the simulation volume are indicated. Scattering parameters are shown in Fig 4.11. It can be distinguished both LH and RH frequency regions, as well as the reflection peak at broadside, which explains why the antenna is not radiating efficiently at this direction.
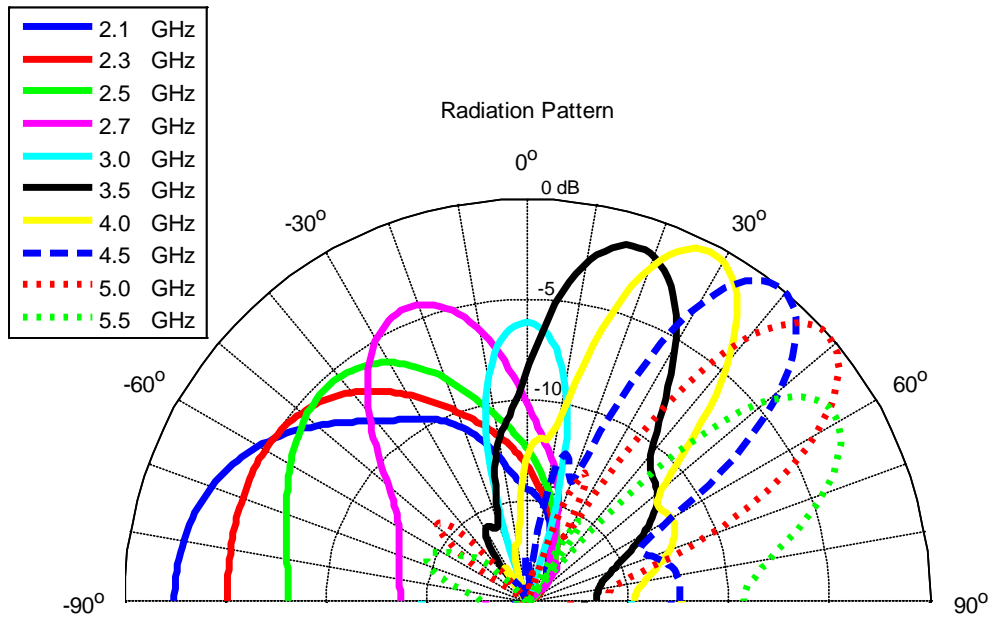
Figure 4.12: Radiation pattern in function of frequency.

Furthermore, Fig. 4.12 presents the scanning capabilities of the antenna, as a function of the operating frequency. Specifically, a scanning of the main beam from the angle θ = −45º up to θ = +60 degrees is shown. As expected, a decrease in the radiation efficiency is found at the broadside direction (θ = 0º). As explained before, note that the directivity is higher in the RH region than in the LH frequency region. This is related to the fact that the radiation losses are higher in the LH region (as shown in Fig. 4.9). Therefore, the input power is radiated in a few unit-cells, leading to a reduced effective length of the antenna (and therefore, a lower directivity). On the other hand, radiation losses are lower at the RH region, and the power is radiated along the whole structure, leading to a larger effective length of the antenna (and, consequently, to a higher directivity).

4.3. Study of the influence of geometrical parameters in the complex propagation constant

Based on the results of the designed CRLH LWA in the previous section, it could be seen that all the geometrical parameters are involved in the characteristics of the antenna complex propagation constant, highlighting that even the slot width affects it considerably. In the literature available, there is only evidence of one taper design [Siragusa, 2012] in the field of metamaterial antennas. In this paper, the aperture distribution optimization was carried out by using genetic algorithms along with full-wave simulations, and the time needed for that task was tremendously high, since there were no analytical expressions available to control the phase constant and the leakage factor for that specific geometry. Furthermore, using that approach gives few insights on how influent is a determined parameter in the complex propagation constant; it is a fact that there are parameters that have a higher impact on it more than others. This suggests that it may be quite difficult to control both radiation leakage and phase constant in a CRLH LWA, depending on its base topology. On the other hand, it is also difficult to obtain physical insights on the modification of a determined geometrical parameter and its influence.

In this particular topology, there are four parameters that influence the properties of a propagating wave: length of the unit cell (l_{uc}), width of the unit cell (w_{uc}), diameter of the via-hole (d_{via}) and slot width (g_{slot}). Note that the dielectric thickness is fixed by the substrate manufacturer and it is not convenient to vary it along the antenna.

Also, the fact that the all the unit cells are balanced, introduces a major constraint in the leakage factor control, as, by logic, it depends almost exclusively on the slot width: if the slot is narrow, then a small portion of the wave would radiate to surrounding space, and if the slot is wide, then a large portion of the wave would radiate to surrounding space. Due to this, the method proposed on [Gómez Díaz et al, 2011a] cannot be used now, as it only works properly for balanced structures. Because of this, radiation in broadside direction may be considerably affected; nevertheless, since the taper design is done for another frequency, far from broadside, the fact that all the unit cells are unbalanced (in principle) lacks importance.

Based on the antenna designed in the previous section, the starting point would be to vary independently one parameter at the time, in order to obtain the influence of isolated geometry parameters in the complex propagation constant.

Diameter of via-hole variation

In this parametrical study, the dimensions that remain constant have the following values: l_{uc} (unit-cell length) = 23.54 mm, w_{uc} (unit-cell width) = 23.54 mm, g (slot width) = 0.5 mm. d_{via} (via-hole diameter) varies from 0.8 mm to 1.2 mm. A frequency sweep is also run, from 2 GHz to 6 GHz in steps of 0.125 GHz.
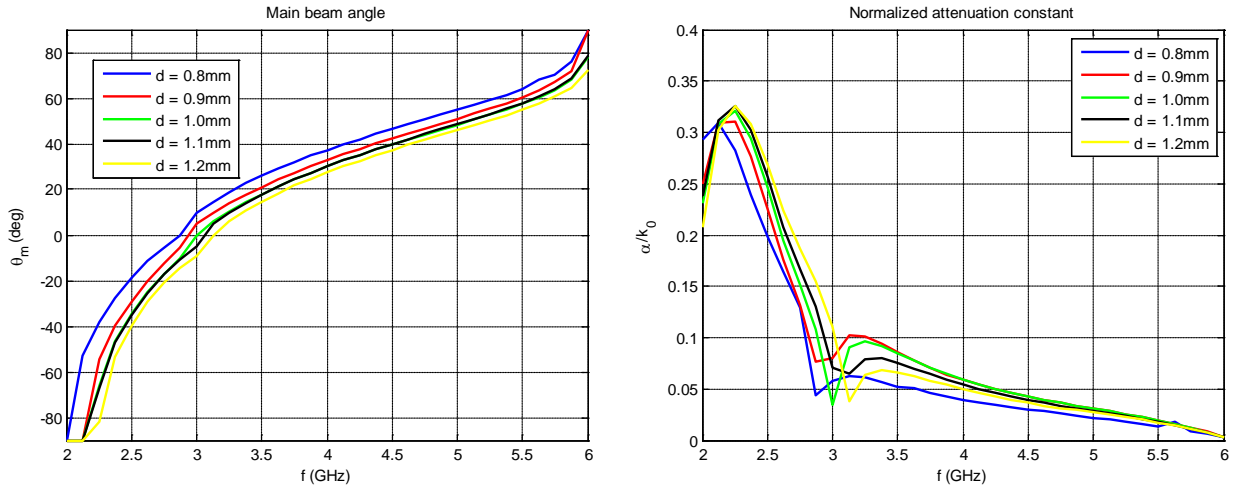
31

Figure 4.13: Main beam angle and normalized attenuation constant for d_{via} variations.

As shown in Fig. 4.13, both propagation and attenuation constant change when the diameter of the via-hole is modified. A clear trend can be seen regarding the WM's cut-off frequency, as it increases when d_{via} increases. Furthermore, it can be noticed that increments in d_{via} do not always lead to linear monotonous increments in the value of the main beam angle. Regarding attenuation constant variations, it can be seen that radiation reduction occurs at different frequencies, since the WM's cut-off frequency value is changed as well.
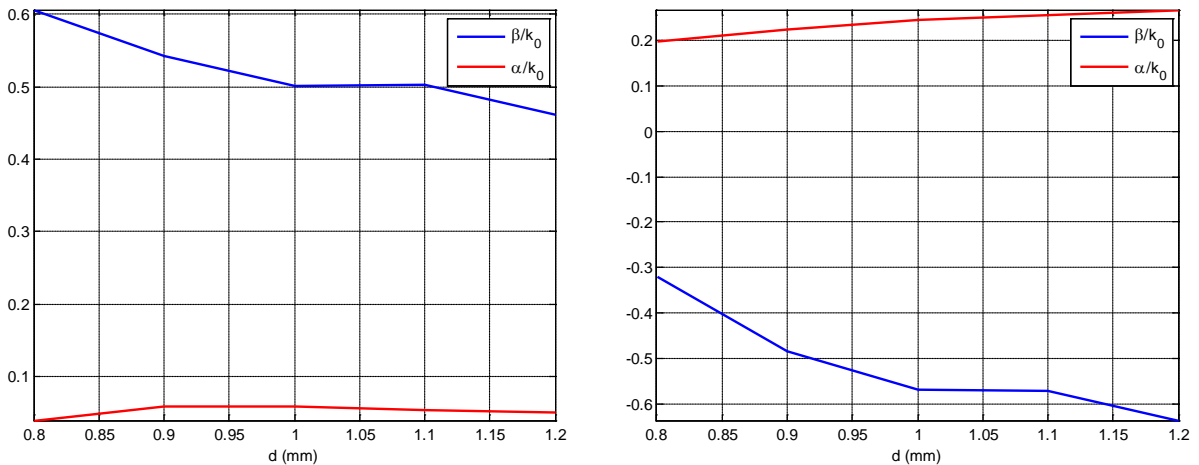
Figure 4.14: Influence of d_{via} on complex propagation constant for RH and LH frequencies.

Fig. 4.14 shows the variations of both phase and attenuation constant for a given frequency, as a function of the via-hole diameter in the RH and LH regions, respectively. For f = 4 GHz (RH region) and f = 2.5 GHz (LH region), a decrease in the phase constant takes place as the diameter increases. Nevertheless, its influence on the attenuation constant is very subtle.

Width of the unit-cell variation

In this parametrical study, the dimensions that remain constant have the following values: l_{uc} (unit-cell length) = 23.54 mm, d_{via} (via-hole diameter) = 1 mm, g (slot width) = 0.5 mm. w_{uc} (unit-cell width) varies from 21 mm to 25 mm. A frequency sweep is also run, from 2 GHz to 6 GHz in steps of 0.125GHz.
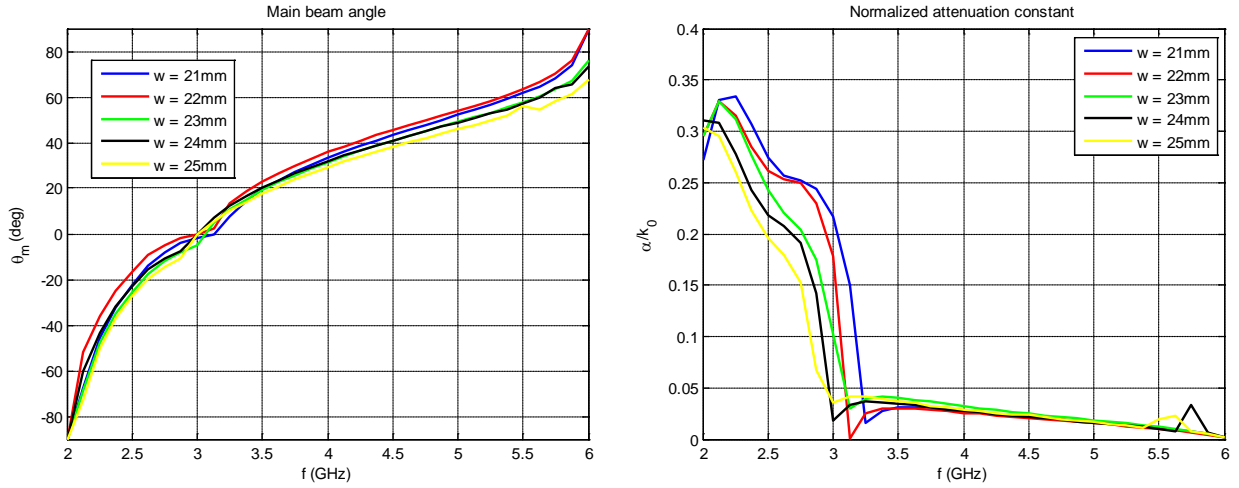

Figure 4.15: beam angle and normalized attenuation constant for w_{uc} variations.

As shown in Fig. 4.15, both propagation and attenuation constant change when the width of the unit cell is modified. A clear trend can be seen regarding the WM's cut-off frequency, as it decreases when w_{uc} increases. Furthermore, it can be noticed that increments in w_{uc} do not always lead to linear monotonous decrements in the value of the main beam angle. Regarding attenuation constant variations, it can be seen that radiation reduction occurs at different frequencies, since the WM's cut-off frequency value is changed as well.
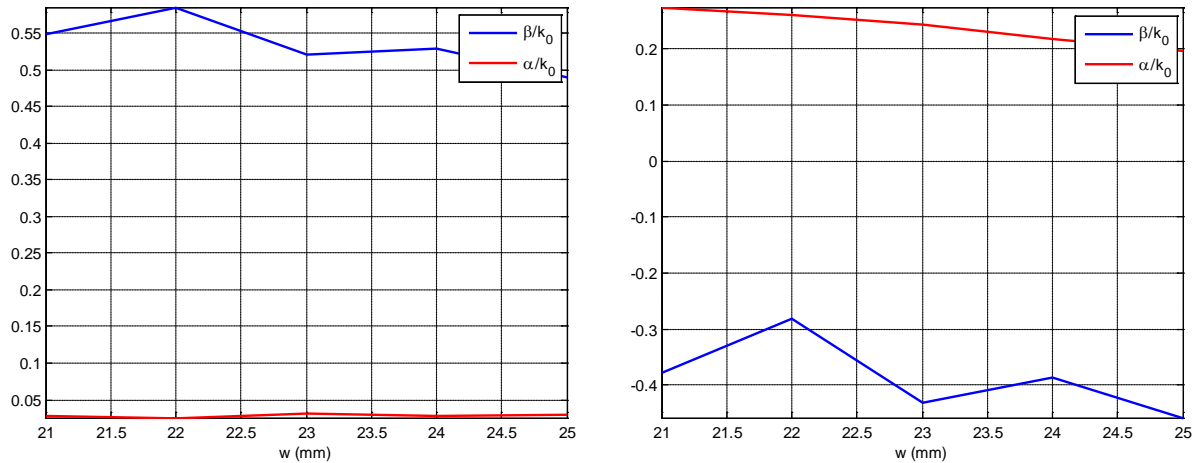

Figure 4.16: Influence of w_{uc} on complex propagation constant for RH and LH frequencies.

Fig. 4.16 shows the variations of both phase and attenuation constant for a given frequency, as a function of the unit-cell width in the RH and LH regions, respectively. For f = 4 GHz (RH region) and f = 2.5 GHz (LH region), variations in the phase constant tend to smaller values, but this decrease is not monotonous as the width increases. On the other

33

hand, its influence on the attenuation constant is very subtle, similar to the way d_{via} influences it.

Length of the unit-cell variation

In this parametrical study, the dimensions that remain constant have the following values: w_{uc} (unit-cell width) = 23.54 mm, d_{via} (via-hole diameter) = 1 mm, g (slot width) = 0.5 mm. l_{uc} (unit-cell length) varies from 21 mm to 25 mm. A frequency sweep is also run, from 2 GHz to 6 GHz in steps of 0.125 GHz.
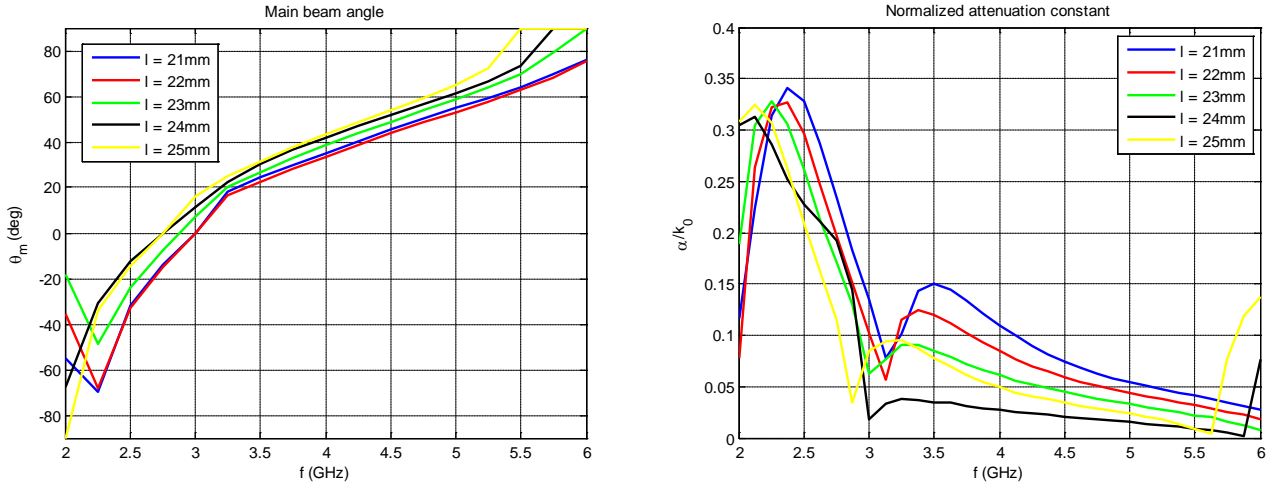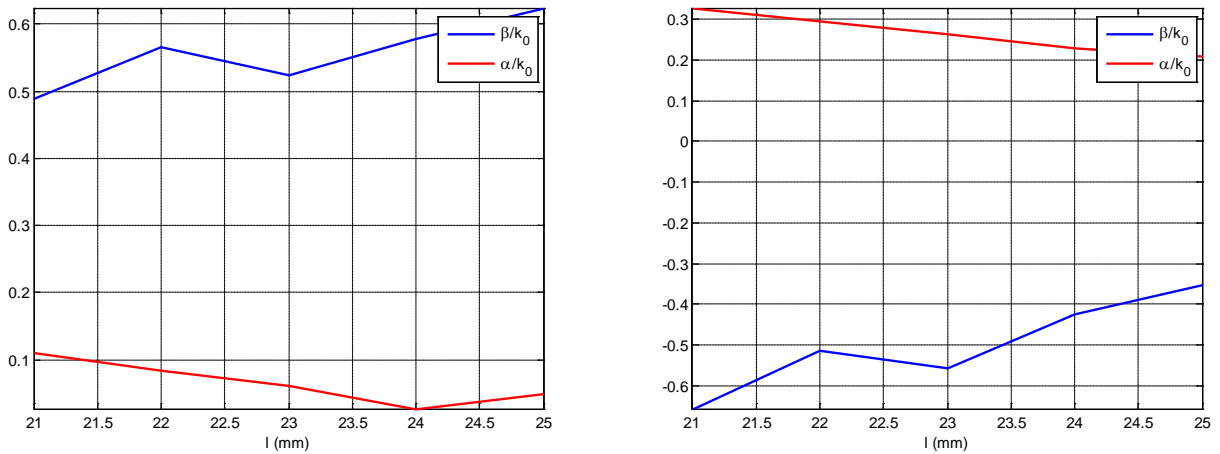

Figure 4.17: beam angle and normalized attenuation constant for l_{uc} variations.

Figure 4.18: Influence of l_{uc} on complex propagation constant for RH and LH frequencies.

As shown in Fig. 4.17, both propagation and attenuation constant change when the length of the unit cell is modified. A clear trend can be seen regarding the WM's cut-off frequency, as it decreases when l_{uc} increases. Furthermore, it can be noticed that increments in l_{uc} lead often to increments in the value of the main beam angle. Regarding attenuation constant variations, it can be seen that radiation reduction occurs at different frequencies, since the WM's cut-off frequency value is changed as well.

In Fig. 4.18 are depicted the variations of both phase and attenuation constant for a given frequency, as a function of the unit-cell length in the RH and LH regions, respectively. For f = 4 GHz (RH region), variations in the phase constant tend to larger values generally as the length increases, and presents an oscillatory-increasing trend. In contrast with the previous studies, an increase in the unit-cell length often leads to a reduction in the attenuation constant, which is very useful for changing aperture illumination distributions in antennas, since very small values of normalized attenuation constant are usually needed.

<u>Slot width variation</u>

In this parametrical study, the dimensions that remain constant have the following values: w_{uc} (unit-cell width) = 23.54 mm, l_{uc} (unit-cell length) = 23.54 mm, d_{via} (via-hole diameter) = 1 mm. g (slot width) varies from 0.3 mm to 0.7 mm. A frequency sweep is also run, from 2 GHz to 6 GHz in steps of 0.125 GHz.
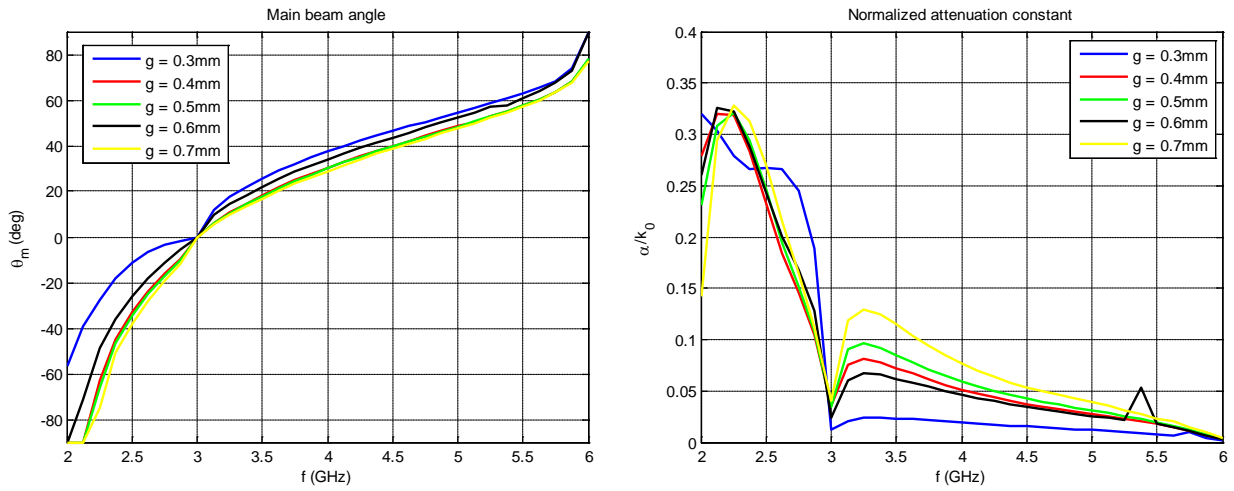

Figure 4.19: beam angle and normalized attenuation constant for g variations.
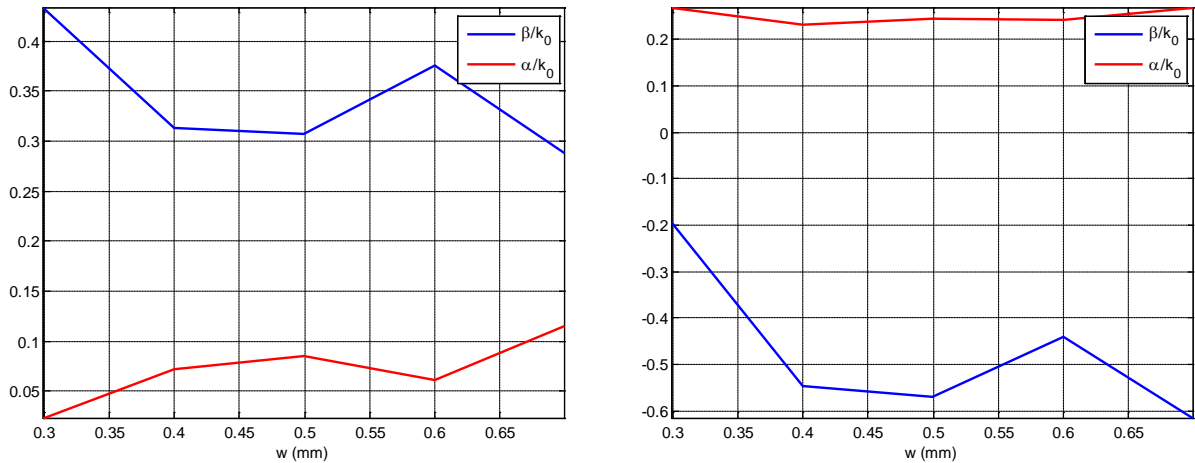

Figure 4.20: Influence of g on complex propagation constant for RH and LH frequencies.

As shown in Fig. 4.19, both propagation and attenuation constant change when the length of the unit cell is modified. In contrast with previous results, the WM's cut-off frequency is not considerably affected; however, the unit-cells are still unbalanced. Furthermore, it can

be noticed that increments in g do not always provide linear monotonous decrements in the value of the main beam angle. Regarding attenuation constant variations, it can be seen that radiation leakages tend to increase as the slot width increases. This constitutes a key result, as it leads to a proper control of the leakage rate.

Fig. 4.20 shows the variations of both phase and attenuation constant for a given frequency, as a function of the slot width in the RH and LH regions, respectively. For f = 4 GHz (RH region) and f = 2.5 GHz (LH region), variations in the phase constant tend to smaller values, but this decrease is not monotonous as the slot width increases, and presents an oscillatory-decreasing trend. On the other hand, an expected increase in the attenuation constant is achieved by making the slot wider. In the LH region however, these variations do not seem to reduce or increase leakage factor values, which are always large.

A straightforward (and logical) conclusion of this preliminary study is that modifying an isolated geometrical parameter does not provide isolated control on the phase constant or the attenuation constant. In the cases of diameter of via-hole and width of the unit cell, however, it can be said that an isolated control may exist, since results dictate that variations of these parameters do not produce noticeable changes in the attenuation constant in the RH region, for instance, but do produce noticeable changes in the phase constant.

Therefore, several geometrical parameters must be simultaneously modified in order to study the viability of a taper design. This is because a taper design cannot be achieved by varying solely one geometric parameter, due to the impossibility of an independent control of α and β.

Since all these results are provided by full-wave simulations, it would be a tedious task to run a parametric sweep varying all the variables at the same time. The HFSS model used for this purpose consists of a reduced number of unit-cells, to reduce the computational cost (mostly RAM) and time. More than 2 unit cell is needed in pursuance of obtaining correct values of α, as well as a fine mesh, since the radiation leakage depends on the coupling between unit cells. Furthermore, note that the calculation of the phase constant includes implicitly the unwrap function due to the periodicity of the cosine function involved (see section 3.2), and as a consequence, a frequency sweep is also needed.

This procedure is already cumbersome and time consuming, and by adding the conjunct variation of all the geometrical parameters, the complexity increases.

Hence, a simplified approach is proposed to increase the physical insight into the problem: fix the values of two structural parameters, and vary with a parametric sweep the two remaining at the same time. The parameters involved now would be the length of the unit cell and the slot width considering that:

- The length of the unit cell influences more on the main beam angle than the width of the unit cell and the diameter of via hole: the possible perturbations, both vias and slots, are periodically placed with this distance along the longitudinal direction, where effective wave propagation occurs. Furthermore, results show that leakage factor can be reduced.

- The slot width controls almost exclusively the radiation leakage. A wider slot will certainly provide larger radiation losses, whereas a narrower slot will provide the opposite, smaller radiation losses.

According to these results, variations of the diameter of the via-hole could counteract the influence of the slot width in the main beam angle, leaving the control of the attenuation constant to the slot, turning into an appealing and interesting solution. However, changes in d_{via} may be impractical in this situation, since feasible diameter values in manufacturing processes are standardized, which introduces an important constraint in the range of values d_{via} could vary. The main objective of this second study is to evaluate the viability of the amplitude taper design. For this purpose, it is needed that the obtained contour plots of phase constant and attenuation constant intersect, which provides several values of leakage rate for a fixed angle. If a contour curve related to a certain value of phase constant is intersected by many contour curves of attenuation constant at a given frequency, then potentially a taper design could be achieved.

Now, based on the dimensions of the antenna design in the previous section, a two-variable parametric sweep is carried out. These contour plots are obtained with a MATLAB routine. Once the parametric sweep in commercial EM software HFSS finishes, the scattering parameter matrix is exported to MATLAB for each simulated variation. Then, the complex propagation constant is calculated by using the theory commented in section 3.2, after the S parameters to ABCD parameters conversion takes place. Later on, for a given frequency, the contour plots represent the variation of both phase and attenuation constants in function of the length of the unit cell and the width slot.
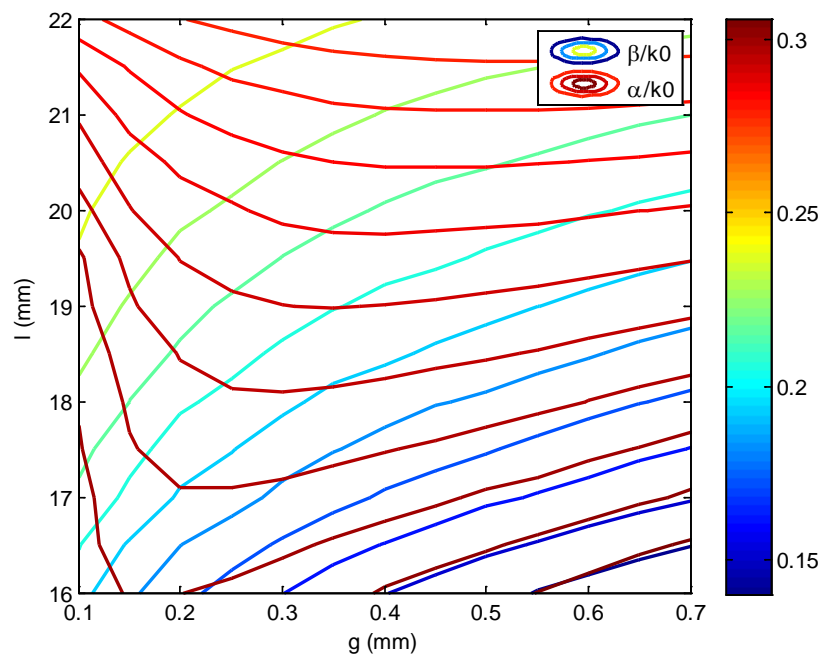

Figure 4.21: Intersecting contour curves – LH region.

It can be seen that for the LH region, as illustrated in Fig. 4.21, there are contour curves of β intersecting plenty of contour plots of α. According to this, it is possible to change the radiation leakage factor, and simultaneously, maintain the phase constant invariant.
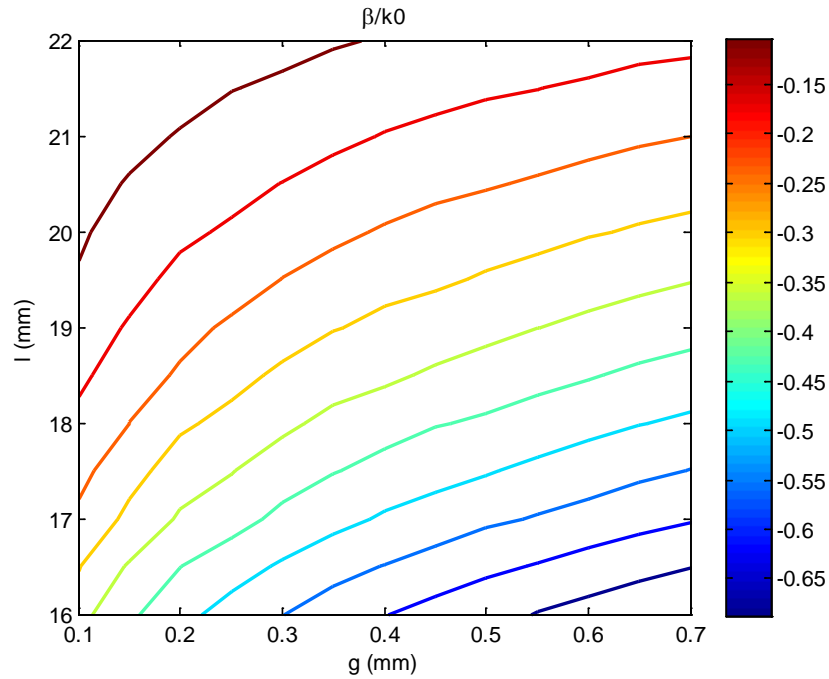

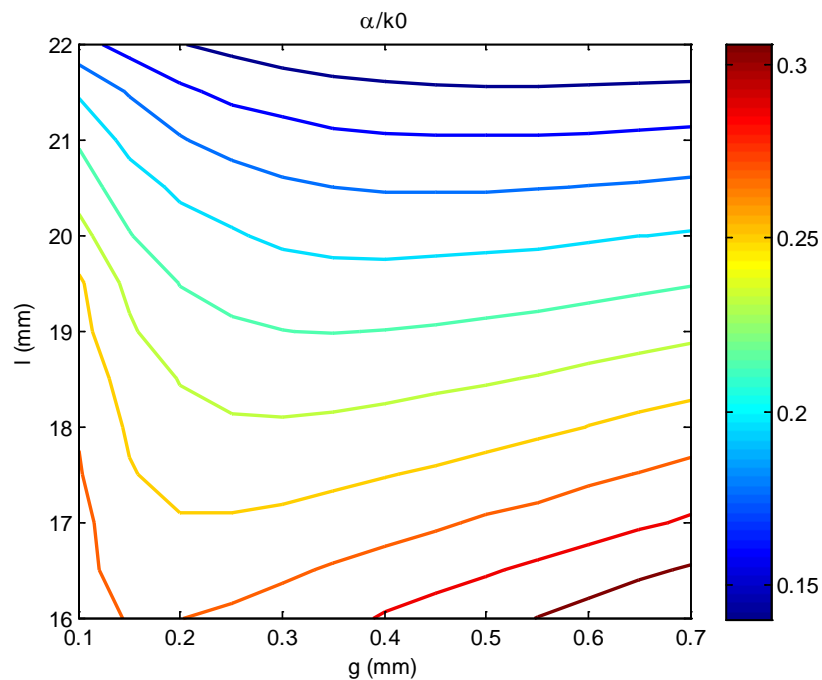Figure 4.22: Normalized phase constant contour plots – LH region.

Figure 4.23: Normalized attenuation constant contour plots – LH region.

However, there is a major issue regarding α contour plots: values are extremely high. From the very beginning, in the case of the base CRLH LWA, the attenuation constant was

very high in the LH region and now, after using smaller values for the slot width, the obtained values are still unsuitable for a taper design. This makes non-feasible a taper design in the LH region with this particular topology, because large variations in the slot width do not produce large variations in α, which is very high.
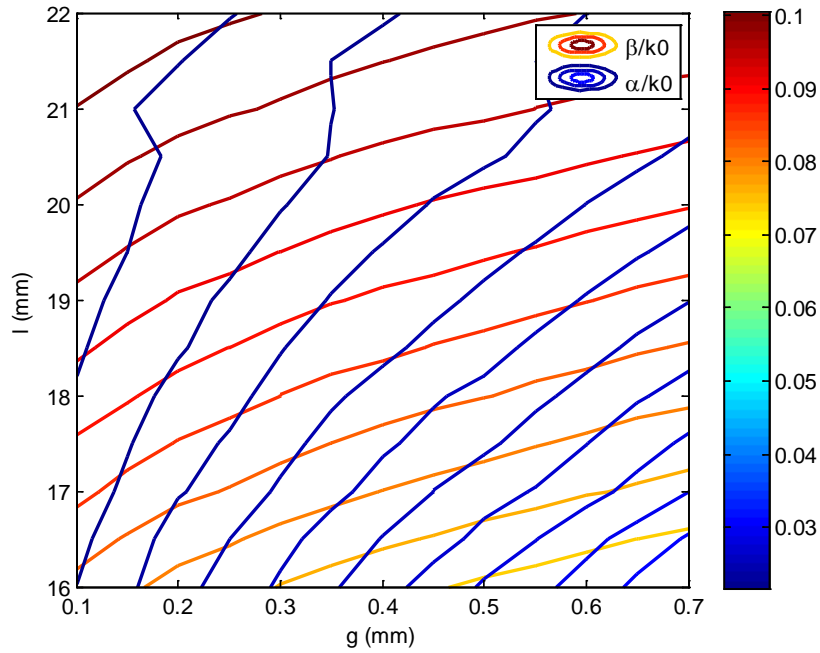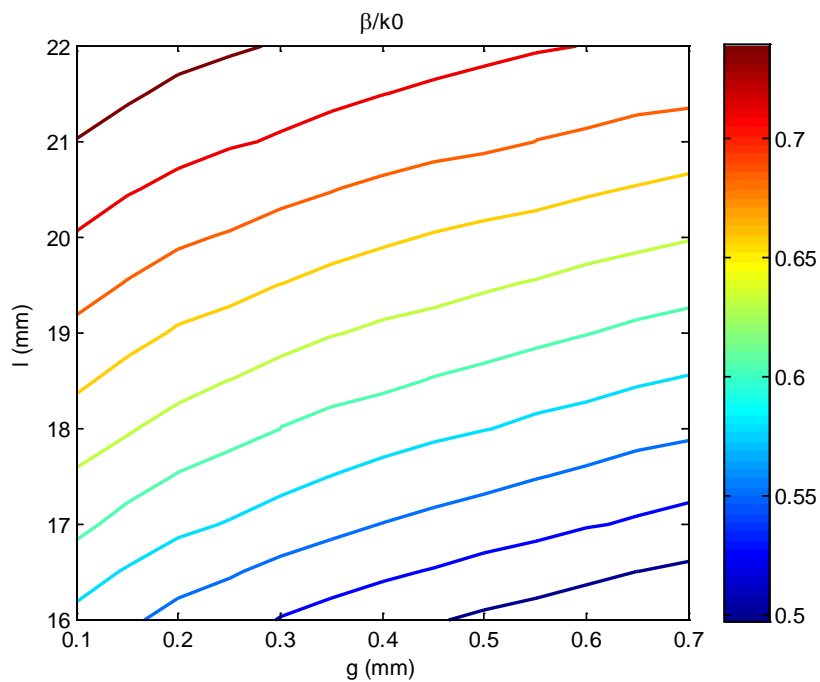

Figure 4.24: Intersecting contour curves – RH region.

Figure 4.25: Normalized phase constant contour plots – RH region.

On the other hand, in the RH region there are also contour curves of β that intersect plenty of attenuation constant contour curves. As previously stated, it is possible to modify the leakage factor and maintain the phase constant invariable at the same time. Nevertheless, in contrast with the attenuation constant values obtained in the LH case, the values obtained here are very appealing and suitable for a taper design. Therefore, a taper design in the RH region is feasible.
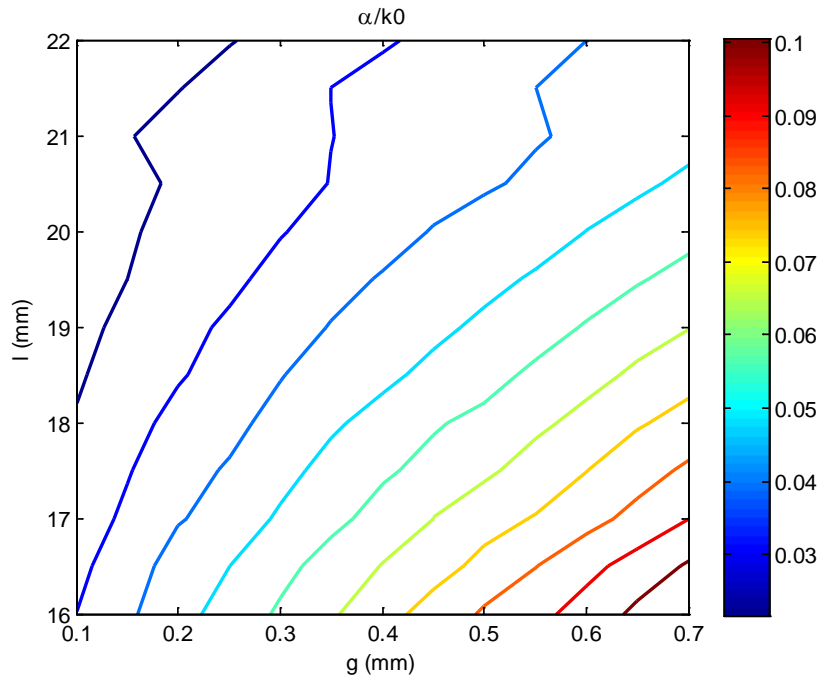

Figure 4.26: Normalized attenuation constant contour plots – RH region.

4.4. Taper design

According to the results commented in the previous section, it is possible to obtain intersecting contour curves of both phase and attenuation constants whether the chosen frequency corresponds to RH or LH regions. Nevertheless, the feasibility of a taper design depends on the effective control of the attenuation constant, so that the values needed for a radiation leakage distribution based on a specific aperture illumination distribution can be obtained with a tapered geometry. Thus, taper designs in the LH region are non-feasible in this particular topology, due to the difficulty to obtain practical values of attenuation constant, whereas taper designs in the RH region are feasible, since most of the values required are accessible.

As mentioned before, in a taper design it is crucial that all unit-cells provide the same phase constant, since all the radiated power must be directed at the same angle to surrounding space. Therefore, the first step in a taper design would be the choice of the main beam angle. Once it is fixed, then all the points where this curve intersects with attenuation constant contour curves must be extracted, since they relate the appropriate geometry for determined main beam angle and leakage factor. The main goal of this

optimization process is to reduce side lobe level up to -20dB by modifying the aperture illumination with a customized one, such as triangular, cosine, cosine square, among others [Link 1]. In this case, the most suitable pattern would be the cosine-type, as side lobes can be at best -23dB below the main lobe. The frequency chosen for this taper design is f = 5 GHz. The desired aperture illumination is the cosine type. Hence, in order to obtain the leakage factor distribution, parameters such as the antenna length and the radiation efficiency are fixed; in this case: $L = 8\lambda_0$ = 480 mm and η = 90%. Figs. 4.27 and 4.28 illustrate the aperture illumination and leakage distributions.
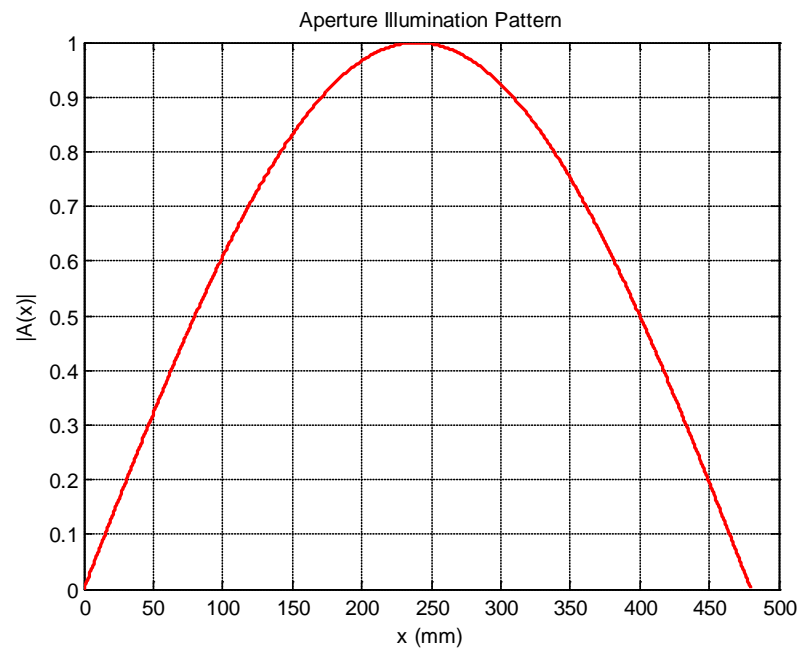

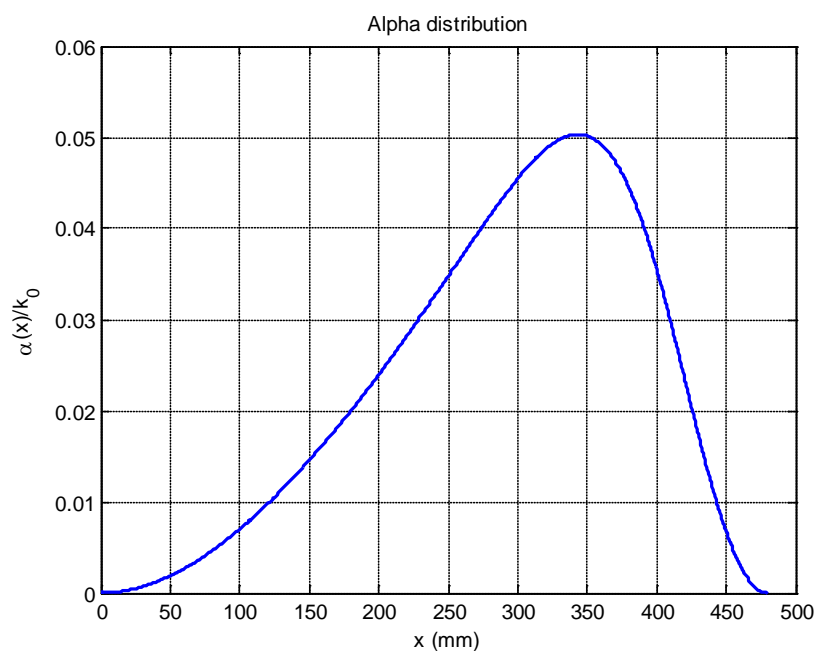Figure 4.27: Desired aperture illumination distribution.

Figure 4.28: Required leakage distribution.

For a taper frequency f = 5 GHz, the obtained contour plots are shown in Figs. 4.29 – 4.30. For a normalized phase constant β/k_0 = 0.71, most of the required values in Fig 4.28 can be obtained with geometrical parameters. For this purpose, variations from 19 mm to 22 mm in the case of the unit-cell length and from 0.1 mm to 0.6 mm in the case of the slot width are required, as shown in Table 1.
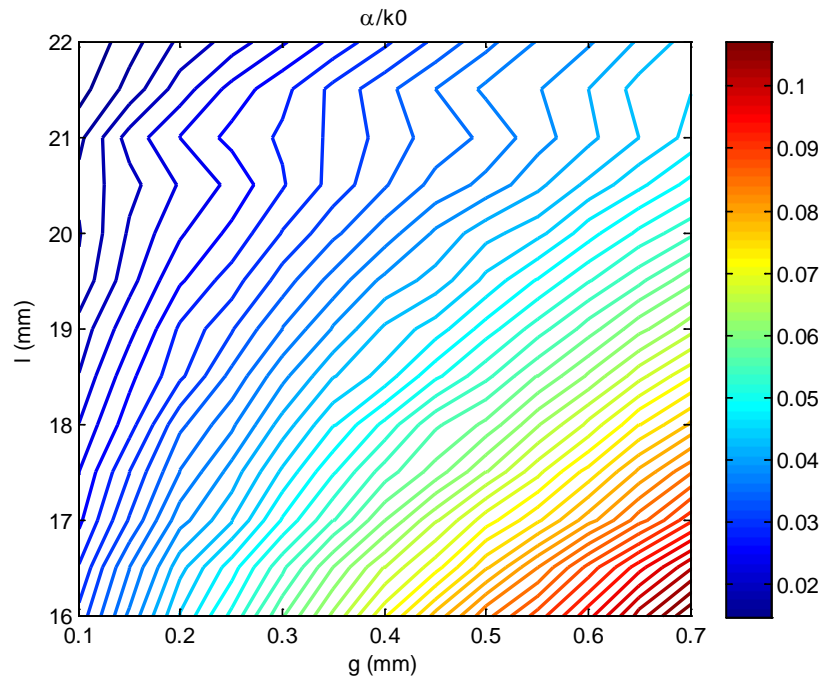

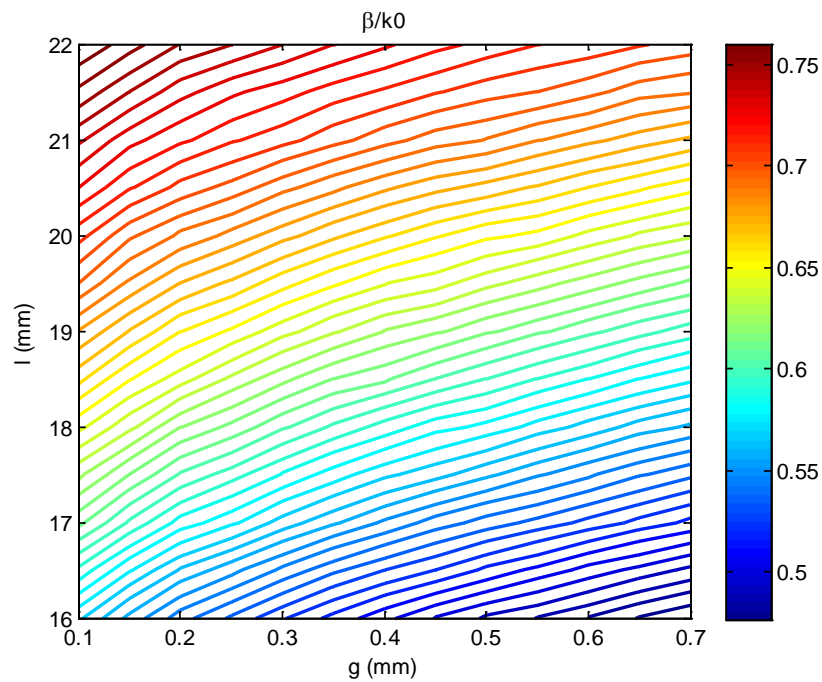Figure 4.29: Normalized attenuation constant contour curves for f = 5 GHz.

Figure 4.30: Normalized phase constant contour curves for f = 5 GHz.

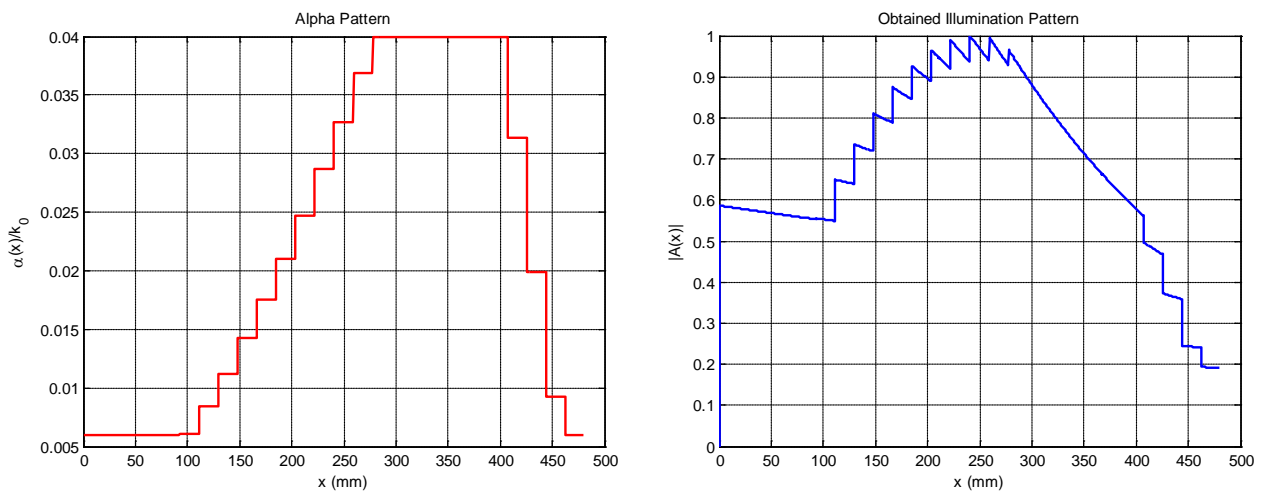| $\alpha/k_{0\ \text{provided}}$	$\beta/k_{0\ \text{provided}}$	l_{uc} (mm)	g_{slot} (mm)
0.02	0.71	20.2	0.132
0.022	0.71	20.54	0.192
0.025	0.71	20.76	0.241
0.028	0.71	20.97	0.303
0.031	0.71	21.26	0.374
0.034	0.71	21.45	0.433
0.038	0.71	21.71	0.523
0.04	0.71	21.96	0.634

Table 1: Accessible leakage rate values for β/k_0 = 0.71.

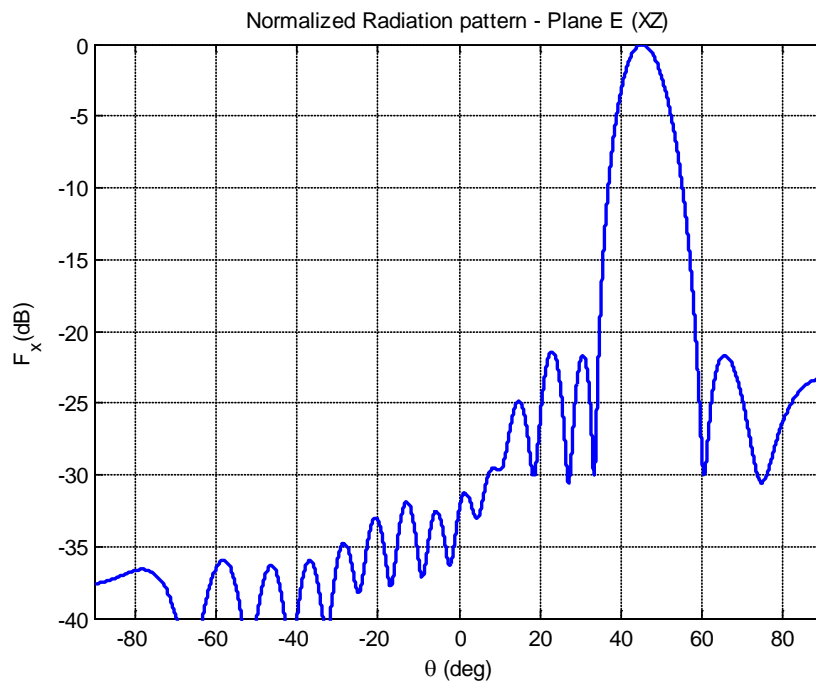Figure 4.31: Truncated leakage distribution – Resultant illumination pattern.

Figure 4.32: Resultant normalized radiation pattern.

Note that the smallest value accessible from Fig. 4.29 is around 0.015 (slot with 0.1 mm width), which is still too high for α_{min}-truncating (see section 3.3). Therefore, another two-variable parametric sweep has to be done for gaps smaller than 0.1 mm. Evidently, smaller values can be obtained, starting from 0.0074.

On the other hand, note that a parametric sweep for obtaining larger values of normalized attenuation constant would be also needed since the highest value available with these geometrical variations is smaller than the highest value required. Fig. 4.31 shows the effect of truncating the distribution to the maximum accessible value from these contour plots. As can be seen in Fig. 4.32, the sidelobe level is under -20dB, which is the main goal. Fortunately, there is no need to run another parametric sweep in this case.

Now, in order to prove this tapering concept, a full-wave simulation of a CRLH-LWA composed of 26 modified unit-cells is carried out with commercial EM software HFSS. Table 2 contains all the dimensions used for this purpose, and Fig. 4.33 illustrates the final model designed using the approach detailed. The structure is excited with the PPW-fundamental mode, with a TL section of $0.75\lambda_0$ = 45 mm long.

| N	$\alpha/k_{0 \text{ provided}}$	$\beta/k_{0 \text{ provided}}$	l_{uc} (mm)	g_{slot} (mm)
1	0.0074	0.71	18.5	0.01
2	0.0074	0.71	18.5	0.01
3	0.0074	0.71	18.5	0.01
4	0.0074	0.71	18.5	0.01
5	0.0074	0.71	18.5	0.01
6	0.0074	0.71	18.5	0.01
7	0.0074	0.71	18.5	0.01
8	0.0086	0.71	18.5	0.02
9	0.010	0.71	19.0	0.04
10	0.013	0.71	19.5	0.06
11	0.016	0.71	20.0	0.08
12	0.020	0.71	20.2	0.1328
13	0.025	0.71	20.76	0.2412
14	0.028	0.71	20.97	0.303
15	0.031	0.71	21.26	0.3746
16	0.038	0.71	21.71	0.5235
17	0.040	0.71	21.96	0.6339
18	0.040	0.71	21.96	0.6339
19	0.040	0.71	21.96	0.6339
20	0.040	0.71	21.96	0.6339
21	0.040	0.71	21.96	0.6339
22	0.038	0.71	21.71	0.5235
23	0.028	0.71	20.97	0.303
24	0.016	0.71	20.0	0.08
25	0.0086	0.71	18.5	0.02
26	0.0086	0.71	18.5	0.02

Table 2: Tapered geometry values.
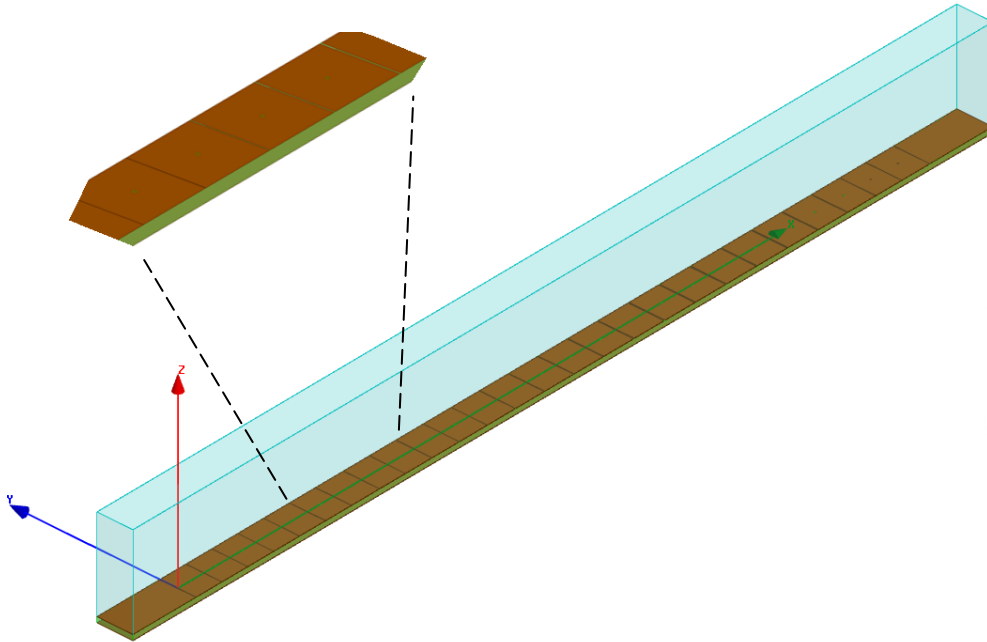
Figure 4.33: HFSS CRLH-Tapered-LWA geometry model.

Fig. 4.34 illustrates the normalized directivity in plane XZ and presents the effective reduction of the sidelobe level with the proposed tapered geometry, as well as the comparative between HFSS results and the MATLAB routines.
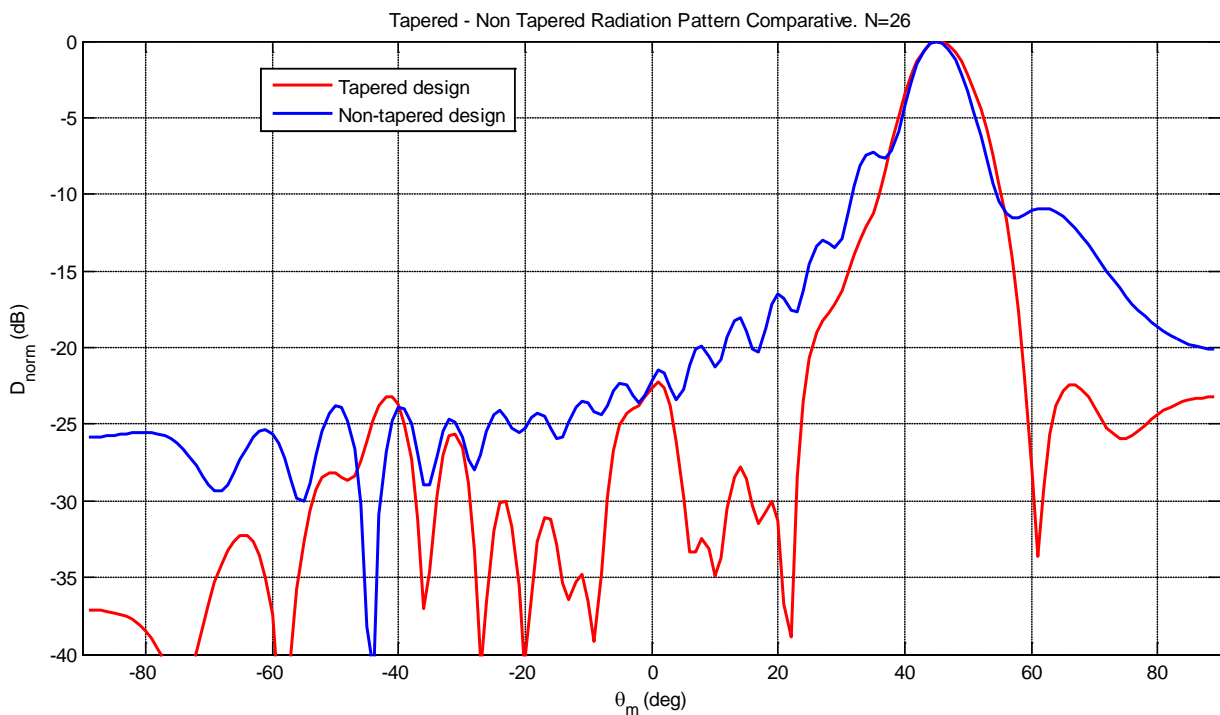

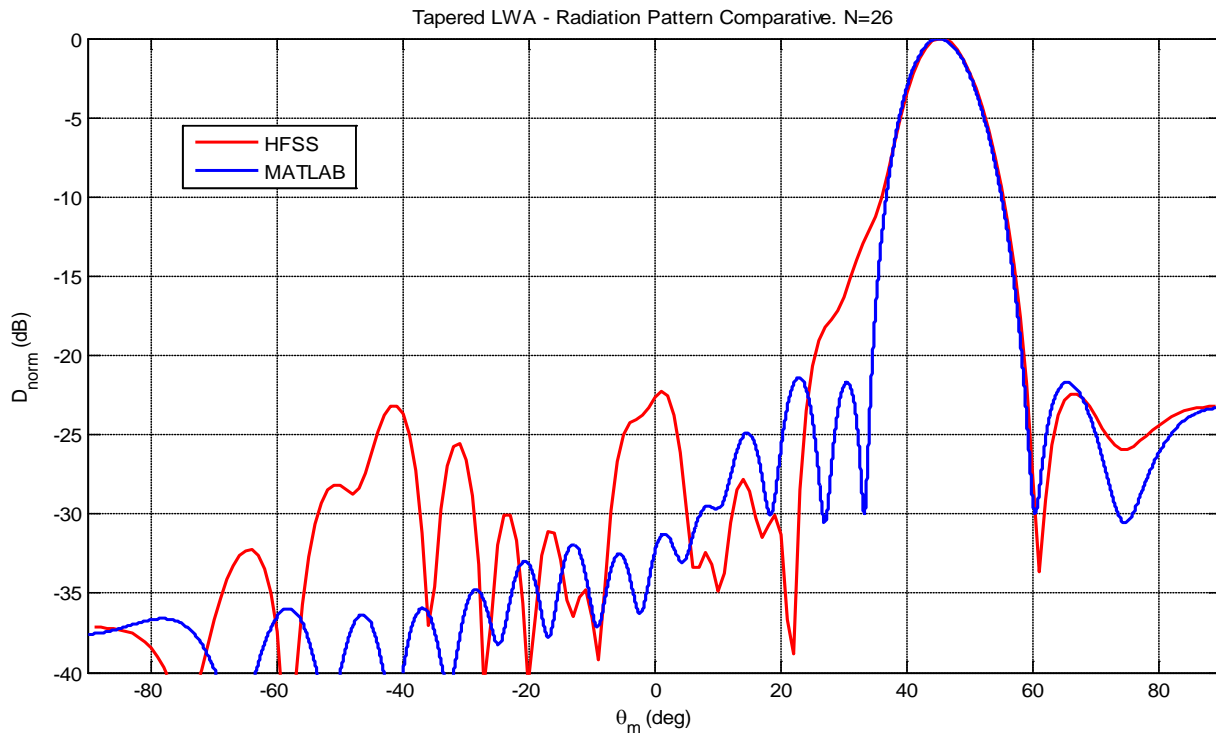Figure 4.34(a): SLL effective reduction.

Figure 4.34(b): Normalized radiation pattern comparative.

It can be seen that side lobes have been reduced to the desired level, which is under -20dB. The main beam, however, does not present symmetry around the main beam angle, since the side lobes located from +20º to +40º have been reduced and "absorbed" by the main beam. On the other hand, the sidelobe located at +62º has been reduced from -11dB to -22dB, which represents a reduction of 100%. Note that the highest sidelobe level in the non-tapered design is 7dB below the main beam, far from the theoretical 13dB characteristic in antennas with uniform field distribution along the aperture. The comparative shows good agreement in angles greater than main beam angle; the sidelobe level within this range differs only on 0.6dB (-21.71 vs -22.32). For angles smaller than main beam angle, although there is almost no agreement between graphs, the sidelobe level is still under -20dB; side lobes that were originally close to the main beam are now part of it.

These results demonstrate that a taper design can be implemented in CRLH-LWAs based on a mushroom-type unit-cell with the theoretical basis described in section 3.3. Nevertheless, this tapered antenna design is impractical, since it cannot be implemented physically due to two major issues related to standard manufacturing process. First, the material used as substrate is foam (hence its low relative dielectric permittivity value), and introduces many difficulties in most physical implementations of designs that requires it. In this particular case, drilling the foam in order to create the via-holes is not a straightforward task. Aside from that, perforations can even change its dielectric permittivity value, which represents an undesirable effect.

Second, and more important: the slot width. This parameter constitutes a major constraint in the control of the complex propagation constant, as its minimum value is limited by the

precision of the available technical resources. In this particular design, the goal was to demonstrate the concept and this specific restriction was not taken into consideration in order to obtain smaller values of leakage rate.

Practical design

In this subsection, an alternative design is proposed based on realistic material and parameter dimensions in order to manufacture a prototype. In contrast with the previous antenna, the dielectric substrate employed for this practical design is Rogers Duroid 5880, characterized by relative permittivity ε_r = 2.2 and thickness t = 1.57 mm. Regarding slot width, the size constraint is now considered from the very beginning. The procedure to design the base CRLH LWA was already presented in section 4.2.

The WM's cut-off frequency is fixed to 5 GHz, and the geometrical parameters set that provide it is: l_{uc} = 16 mm - w_{uc} = 20 mm - d_{via} = 5 mm. This is one of the many sets that correspond to a WM with a cut-off frequency equal to 5 GHz. Note that the effective homogeneity condition is not satisfied, since $l_{uc} > \lambda_g/4$. This fact will constitute a huge difference between the results previously presented and the ones obtained here. First, from the initial study in section 4.3, it is known that increasing the unit-cell length often leads to a decrease in the attenuation constant for a fixed g_{slot}. Therefore, smaller values can be obtained if the homogeneity condition is not fulfilled; in the previous antenna, the leakage rate values were insufficient for a taper design when the gap restriction was considered and $l_{uc} < \lambda_g/4$. Second, in antennas based on practical substrates, like the one presented in [Gómez Díaz et al, 2011b], it can be seen that the length of the unit-cell is quite small due to this condition. Moreover, small values of g_{slot} (0.2mm) still provide high values of attenuation constant in the RH region [Gómez Díaz et al, 2011b], making extremely difficult a possible control by reducing the slot width, which is also limited by the precision of the available technical resources. This suggests that small values can be obtained if the ratio between unit-cell length and slot width, for a given frequency, is high.

By adding slots (with width g = 0.5 mm) periodically along the longitudinal direction, a CRLH LWA is created. Figs. 4.35 - 4.37 illustrate the features of the redesigned antenna.
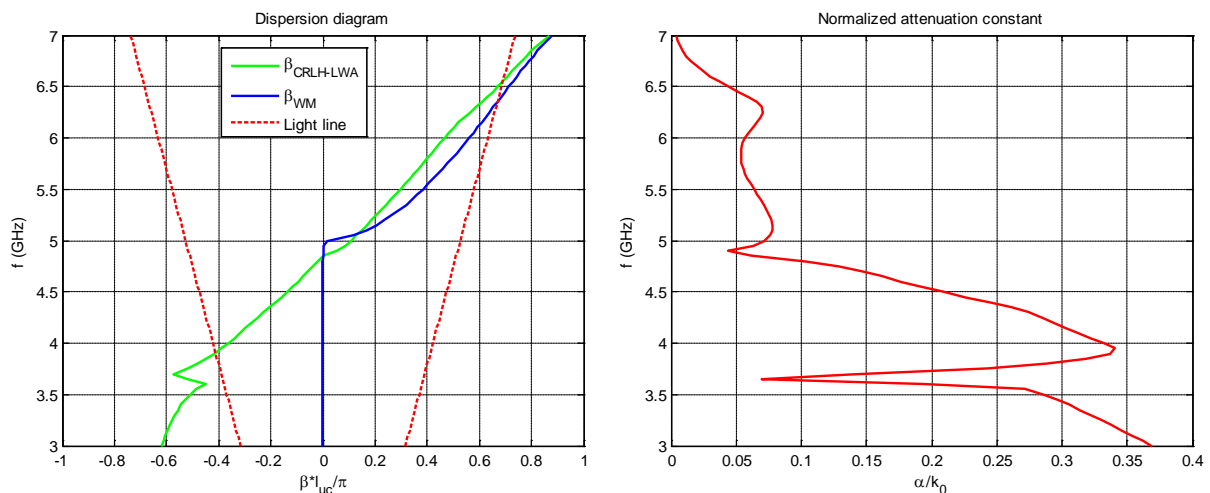

Figure 4.35: Dispersion diagram/Normalized attenuation constant of the redesigned antenna.

As can be seen, the fundamental spatial harmonic of the designed antenna is fast for frequencies between 4 GHz to 6.5 GHz approximately. In contrast with the WM's fundamental harmonic, the cut-off frequency has suffered a slight shift, going from 5 GHz to 4.85 GHz. The attenuation constant presents a radiation reduction at broadside direction. The values obtained in the RH region are small and suitable for a taper design. Scattering parameters are illustrated in Fig. 4.36, referred to the PPW host TL characteristic impedance (19.98Ω in this case). The matching is very good in the LH region, similar as it was in the previous design. In the RH region however, the reflected power is higher than 10%; this can be fixed by designing additionally an input matching network, in order to reduce this inefficiency, especially for the upcoming practical tapered design.
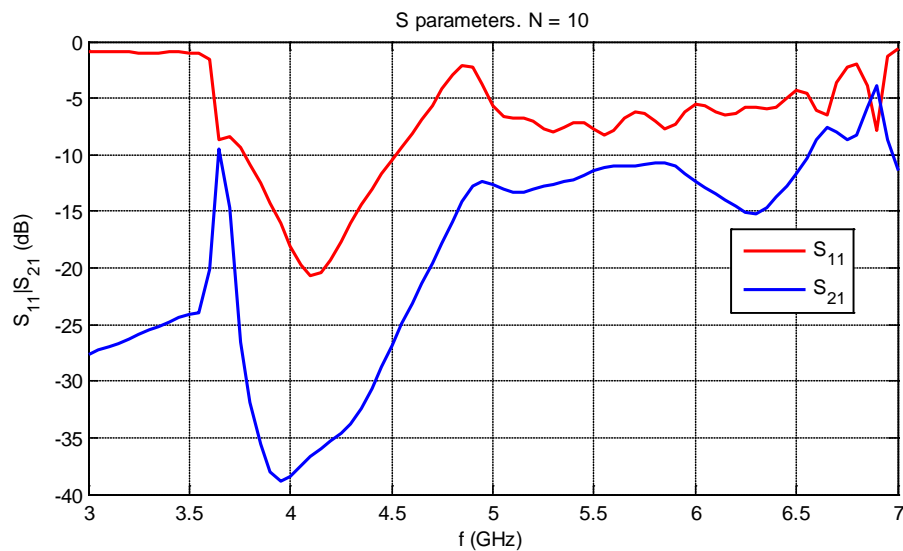

Figure 4.36: S parameters.

Fig. 4.37 depicts the normalized radiation patterns obtained at different frequencies. Note that both main beam and side lobes are well-defined. Therefore, this antenna is suitable for optimization, so that side lobes can be reduced to a desired level from the main beam.
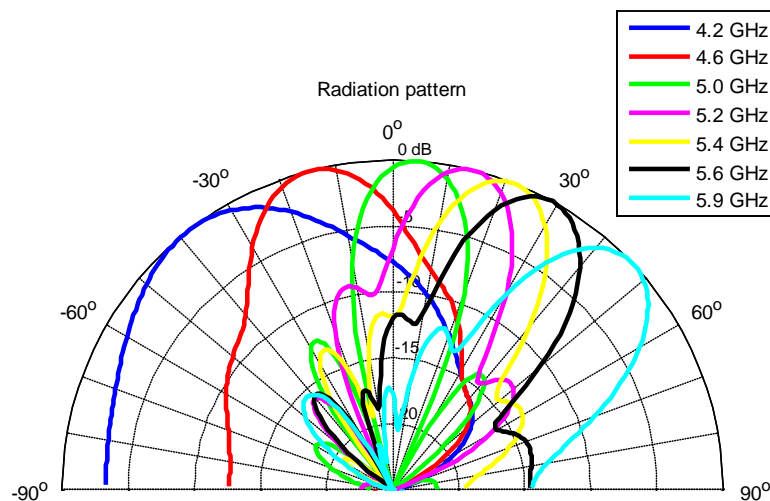

Figure 4.37: Radiation pattern at different frequencies.

Next, the contour curves that relate the complex propagation constant with the geometrical parameters modified are presented in Fig. 4.38. For a taper frequency f_{TAPER} = 5.4 GHz.
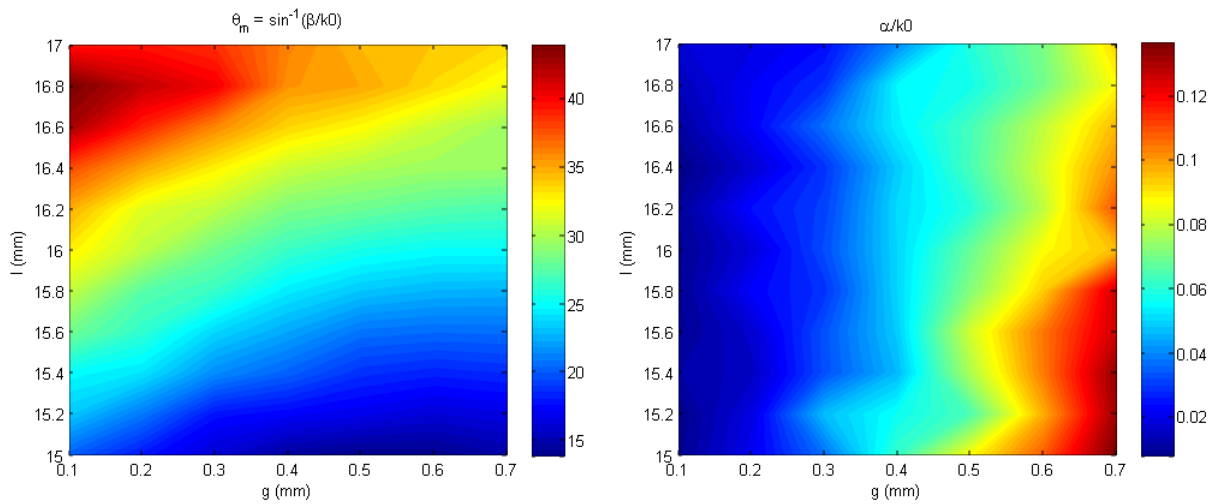

Figure 4.38: Beam angle and leakage rate contour curves for f = 5.4 GHz.

Now, regarding the modification of the cosine-type aperture amplitude distribution, Fig. 4.39 shows the required leakage distribution and its resultant illumination pattern. In this case: $L = 4\lambda_0 = 222$ mm and $\eta = 92\%$. The minimum normalized attenuation constant value accessible is 0.008 as can be seen in Table 3.
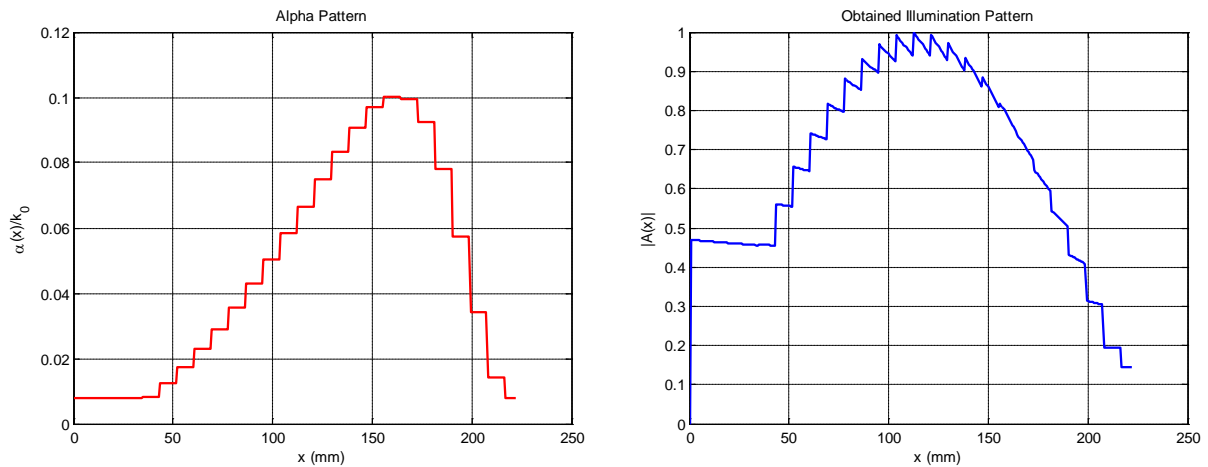

Figure 4.39: Required leakage distribution/Resultant illumination pattern for f = 5.4 GHz.

N	$\alpha/k_{0\ provided}$	$\theta_{m\ provided}$ (deg)	l_{uc} (mm)	g_{slot} (mm)
1	0.008	20	15.2	0.10
2	0.008	20	15.2	0.10
3	0.008	20	15.2	0.10
4	0.015	20	15.4	0.20
5	0.022	20	15.5	0.25
6	0.032	20	15.6	0.30
7	0.048	20	15.8	0.40
8	0.064	20	16.0	0.50

9	0.081	20	16.0	0.60
10	0.091	20	16.0	0.72
11	0.010	20	16.0	0.75
12	0.091	20	16.0	0.72
13	0.053	20	15.9	0.45
14	0.015	20	15.4	0.20

Table 3: Tapered geometry values for practical design.

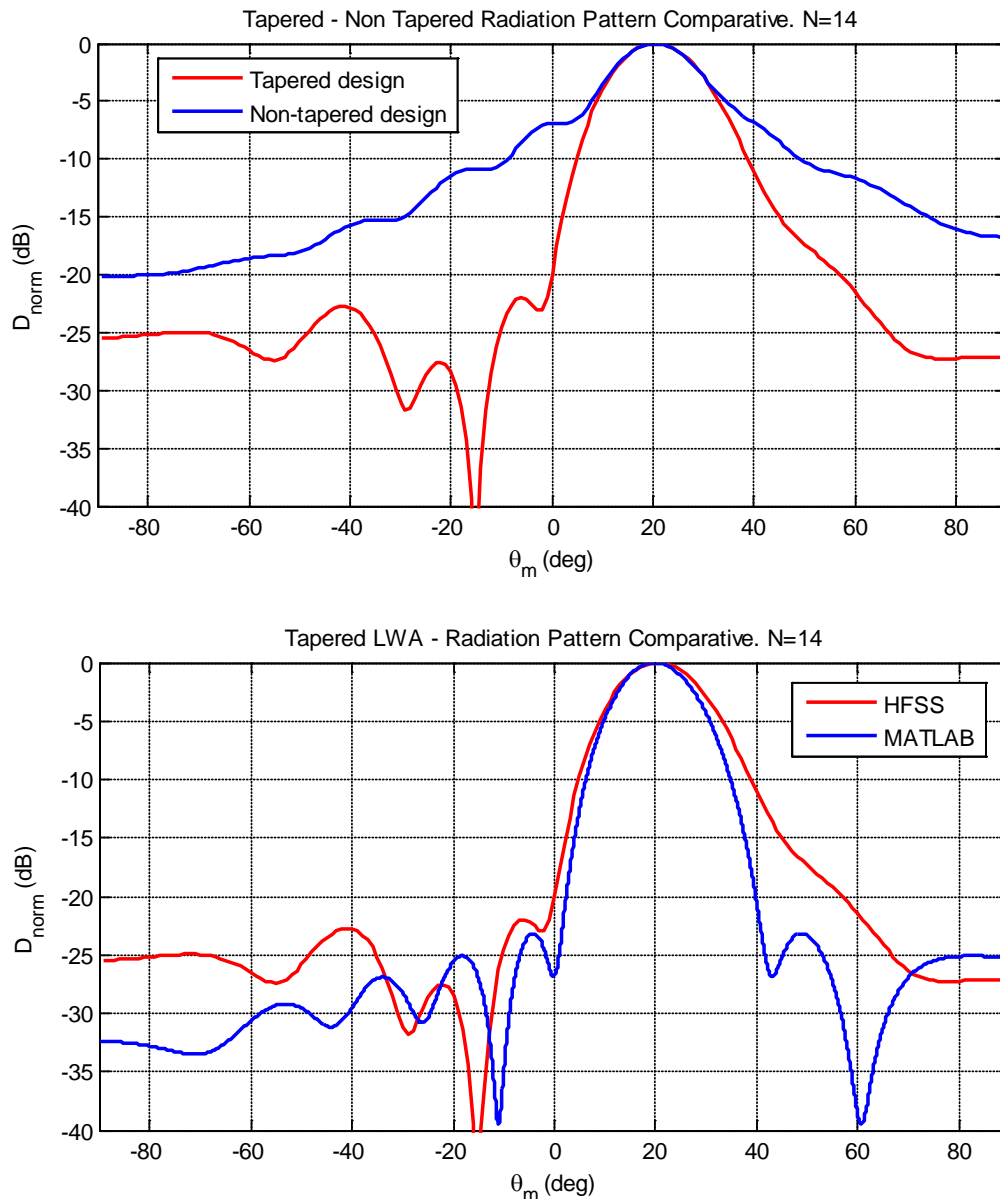
Figure 4.40: SLL effective reduction – Normalized radiation pattern comparative.

A shown in Fig. 4.40, side lobes reduction process has proven to be successful, since the simulated tapered geometry have reduced the sidelobe level from -7dB to -22dB, achieving a -15dB reduction. The radiation pattern obtained from analytical approach (section 3.3) presents good agreement overall with the results obtained by full-wave simulation; sidelobe level was supposed to be -23.16dB, in contrast with the obtained value of -21.96dB.

LWA at optical frequencies: O-LWA

5.1. Introduction

While radiowave and microwave antennas constitute the cornerstone of current wireless communication systems and a wide variety of applications and services, their optical analog is basically nonexistent in today's technology. However, recent research in nano-optics and plasmonics has generated considerable interest in the optical antenna concept, and several studies are currently focused on how to translate established radiowave and microwave antenna theories into the optical frequency regime.

The reduced presence of optical antennas in current technological applications is mostly due to their characteristic dimensions, often in the order of nanometers, which demands very high fabrication accuracies. The advent of nanoscience and nanotechnology provides access to this length scale with the use of novel top-down nanofabrication tools (for example, electron-beam lithography) and bottom-up self-assembly schemes. The fabrication of optical antenna structures is an emerging opportunity for novel optoelectronic devices [Wang, 2011].

Some of the applications in the near-infrared frequency range that have gained significant attention in the recent years, such as planar imaging [Song, 2009] and LIDAR [Toth, 2009], are based on antennas with very directive beams and a electronically controlled beam steering capability.

A novel optoelectronic dielectric antenna comprising periodic semiconductor corrugations has been proposed in [Song, 2011]. The OLWA can be employed as a passive transmitter or receiver as well as a beam steering device. The fact that this antenna is based on semiconductor materials enhances electronic tunability of the optical parameters of silicon and hence, to modify its radiation capabilities [Song, 2011]. The proposed antenna is implemented theoretically on the Silicon-On-Isolator platform, which provides tight mode confinement due to a large index contrast, essential for miniaturization and simultaneous low loss operation [Friedman, 1988]. This antenna is based on the periodic leaky-wave antenna concept: the addition of periodical perturbations in an open host TL, in which its fundamental mode is slow, excites an infinite number of spatial harmonics, and radiation phenomenon takes place when at least one of these harmonics becomes fast. The reconfigurability aspect of this antenna is quite limited, since the results showed

barely noticeable difference in the antenna's radiation properties; its reconfigurability is based on excess carrier injection in the silicon perturbations.

A practical implementation of this particular structure is not straightforward at all, as all materials involved are solids, and the manufacturing processes available nowadays do not permit the addition of the corrugations between two rigid dielectrics. On the other hand, the field of optofluidics has the potential of integrating optics with microfluidics, enabling cost-effective methods for lab-on-a-chip applications [Psaltis, 2006], representing a very appealing alternative to the aforementioned approach. In the present work, the functioning principle of this antenna is explained and, at the same time, an alternative microfluidic implementation is proposed, by using suitable materials and fabrication techniques.

5.2. Rectangular Optical Fiber

Optical fibers are the optical analog of waveguide or transmission lines in microwaves. Optical fibers are widely used in fiber-optic communications, which permits transmission over longer distances and at higher bandwidths (data rates) than other forms of communication with less attenuation and are also immune to electromagnetic interference. A rectangular optical fiber is no different from a cylindrical one; both are based on the same principle: Total Internal Reflection. The total internal reflection condition states that, in order to guide a light wave without attenuation losses along an optical fiber section, the modal refractive index (or normalized propagation constant in the longitudinal direction) must be greater than the cladding refractive index and smaller than the core refractive index. Mathematically, in order to achieve mode confinement:

$$n_{clad} < \frac{\beta}{k_0} < n_{core} \qquad (5.2.1)$$

Therefore, the cut-off frequency of the two dimensional rectangular dielectric waveguide is the frequency at which the normalized propagation constant in the longitudinal direction is equal in value to the cladding refractive index. Above cut-off, the fields will be confined mostly in the core, and a small portion of the wave will still travel through the cladding, but close to the cladding-core interface. As frequency largely increases above cut-off, the mode gets tightly confined, and the fields in the cladding highly attenuate in the transverse direction. On the other hand, if operating frequency is below cutoff, propagation phenomena still exist along the longitudinal direction. However, the transverse components of the field traveling through the cladding are not evanescent (fields do not decay along the transverse directions), which leads to a radiation phenomenon, since the confinement is not ensured.

The analysis of this particular structure is carried out with commercial EM simulator, HFSS. The proposed model is described as follows: the structure consists of a dielectric rectangular box embedded (core) in another dielectric rectangular box (cladding) with a relative permittivity smaller than that of the first, which is also surrounded by air. In this way, a wave is guided along the entire structure if its frequency is above the cutoff

frequency of the dielectric waveguide, and the fields are more confined in the core as this frequency increases, above cutoff. Provided the symmetry of the problem in Y-Z axes, the modes excited in this waveguide will be degenerated, and similar to the ones found in a conventional rectangular waveguide (TE_{10}-TE_{01}). In this case, only the mode polarized along Y axis will be used.

Regarding materials, instead of using the materials proposed in [Song, 2011], the fiber cladding will be made of PDMS (Polydimethylsiloxane). This material has been widely employed in many microfluidics devices, as well as in other applications, due to the versatility it provides in manufacturing processes, such as soft-lithography or nanostencil lithography [Aksu, 2011]. Furthermore, this material present a very small loss tangent (<< 0.001). In this case, PDMS will be used to create a microfluidic channel (fiber's core), in which a determined liquid will flow through it. The liquid used for this purpose is the benzyl alcohol. The refractive indexes of both materials are shown in Fig. 5.1.

$$w_{core} = 1.75\,\mu m$$
$$w_{clad} = 7\,\mu m$$
$$n_{core} = 1.54$$
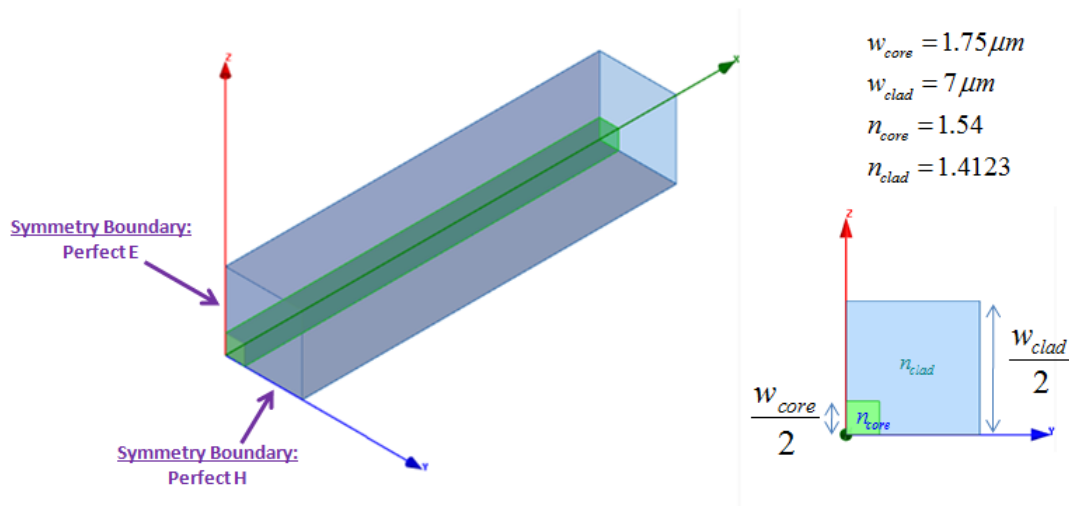$$n_{clad} = 1.4123$$

Figure 5.1: Geometry model for a rectangular optical fiber.

Symmetry boundary conditions are applied to reduce computational cost and required time considerably. By setting Perfect E and Perfect H boundaries in XZ and YZ planes, respectively, the excited mode will be aligned in the Y direction. Fig. 5.1 shows the dimensions used and the geometry model.
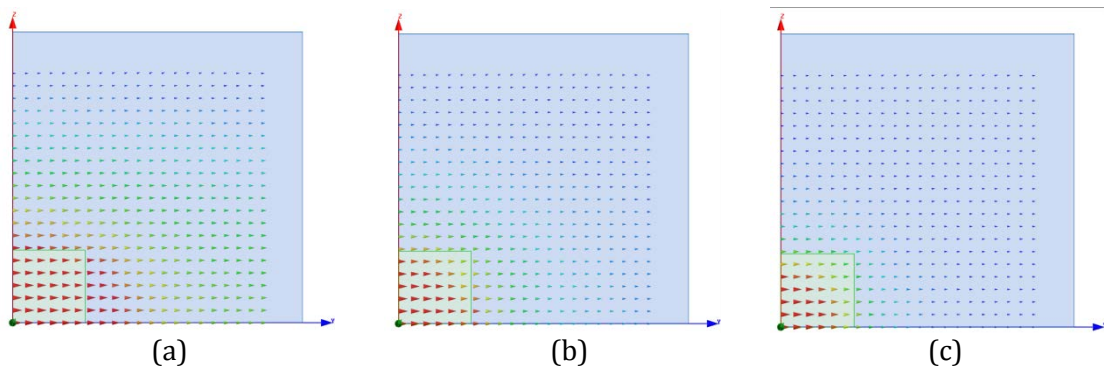

(a)   (b)   (c)

Figure 5.2: Electric field at input port. (a) 90 THz, (b) 130 THz, (c) 190 THz.

53

Fig. 5.2 illustrates the fields on the input port as a function of operating frequency. All these scenarios correspond to operating frequencies above cut-off. It can be seen that the mode gets more confined as frequency increases, as described before. The operating frequency range of interest goes from 175 THz to 215 THz, which corresponds to the third window of transmission in optical communications. The Scattering parameters and the normalized propagation constant of the rectangular optical fiber are shown in Figs. 5.3 and 5.4 respectively. The scattering parameters in the frequency region of interest have expected values (very low percentage of reflected power and very high percentage of transmitted power). Hence, the wave is guided without attenuation from one port to the other. Note that the materials involved in this design are considered lossless.
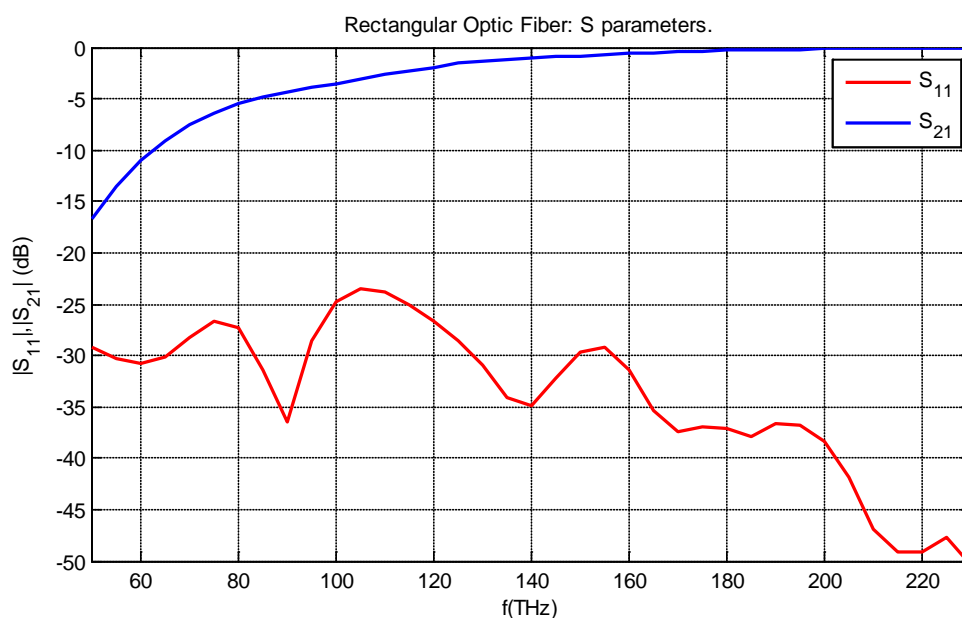

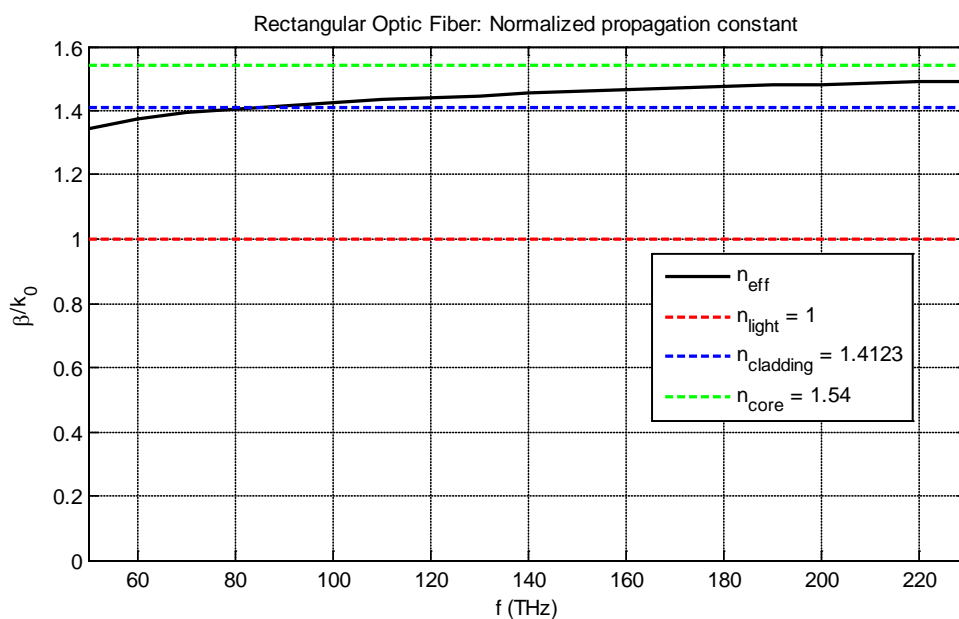Figure 5.3: Rectangular optical fiber S parameters.

Figure 5.4: Rectangular optical fiber Normalized propagation constant.

The normalized propagation constant plot shown in Fig. 5.4 is very useful in order to understand the operation of this dielectric waveguide with frequency: for a modal refractive index greater than 1 but less than 1.4123 (n_{clad}=1.4123), the wave is in the slow-wave region and it is being guided, but the fields are not confined in the core, they are travelling also through the cladding, and due to this, there is also a leakage phenomenon (incident field lines in cladding-air interface; $|S_{21}|$ is not close to 0dB). Now, if the modal refractive index value is between the cladding refractive index and core refractive index, the wave starts being confined solely in the core (the closer it is to n_{core}=1.54, the more the confining is; the closer it is to n_{clad}=1.4123, the less the confining is). In this case, the wave is completely guided and there is no leakage phenomenon whatsoever provided that in this region total internal reflection is achieved. Fig. 5.5 illustrates the fields propagating inside the rectangular dielectric waveguide in function of frequency. As can be seen, in the frequency range of interest, the mode is tightly confined.
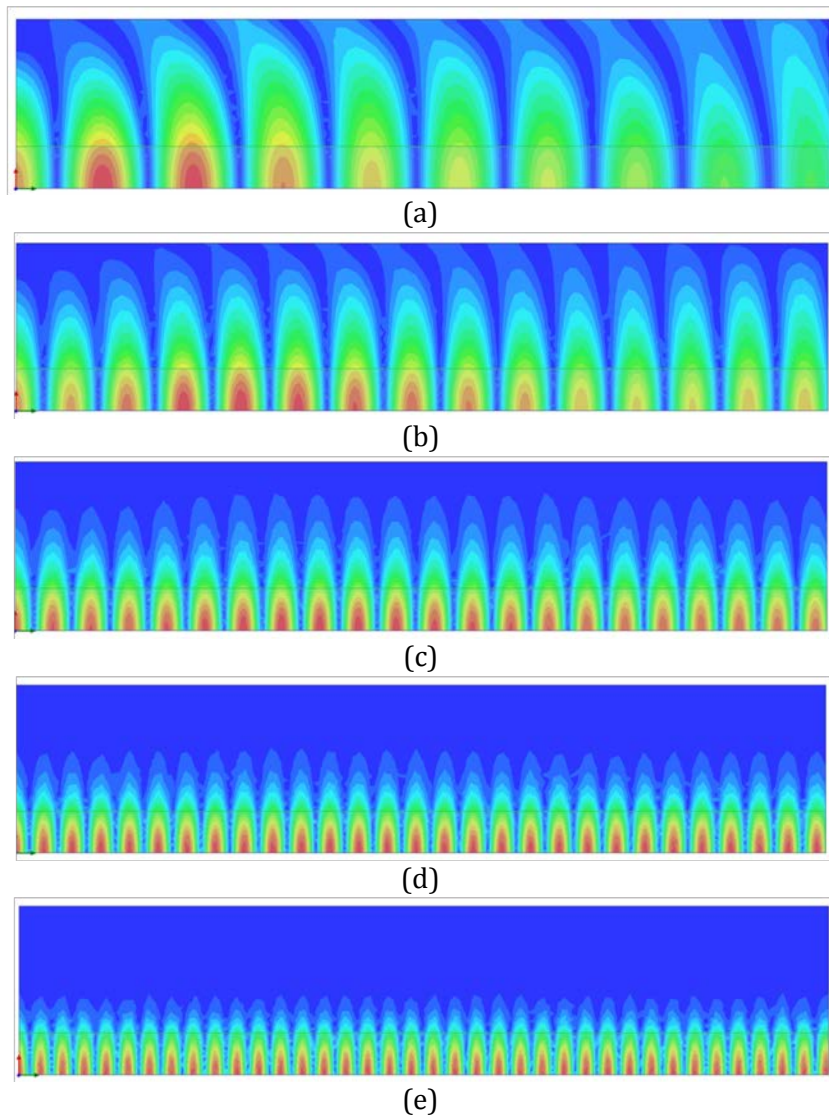

(a)

(b)

(c)

(d)

(e)

Figure 5.5: Field distribution in function of frequency.
(a) 60 THz, (b) 90 THz, (c) 130 THz, (d) 170 THz, (e) 220 THz.

5.3. Optical Leaky-Wave Antenna

In the previous section, the waveguiding structure was designed and analyzed with commercial EM software HFSS. Now, in order to obtain a leaky mode, a set of corrugations must be added periodically into the rectangular optical fiber. As commented in section 3.1, this periodicity creates a guided wave that consists of an infinite number of space harmonics, which are characterized by phase constant β_n and related to each other by (3.1.7). The fundamental space harmonic (β_0) is simply the original β of the dominant mode of the unperturbed waveguide, but somehow perturbed due to the presence of the periodic perturbations.

In this case, the waveguiding structure is already open and its propagating mode corresponds to a slow-wave. By adding these corrugations with an optimized period d, the space harmonic $n = -1$ becomes fast, and the unperturbed mode becomes a leaky mode, thus allowing radiation.
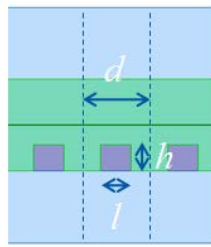

Figure 5.6: Perturbation geometry.

The set of perturbations consists of rectangular silicon bars aligned in the Y direction (parallel to the electric field) with dimensions h, l and w in Z, X and Y directions respectively. The distance between perturbations is d, and its value is conveniently fixed so that the antenna can radiate power at broadside direction and at angles close to it, both positive and negative. Fig. 5.6 depicts the perturbation used as the host TL loading. The proposed antenna comprises 40 periodical corrugations with optimized dimensions $l = 0.5\mu m$, $h = 0.5\mu m$, $w = w_{core} = 1.75\mu m$ and $d = 1.1\mu m$, obtained from a parametric sweep. Since this structure is large and complex, the model employed in HFSS makes use of symmetry boundary conditions to reduce the amount of memory needed for calculations.

$$N_{cells} = 40$$
$$d = 1.1\mu m$$
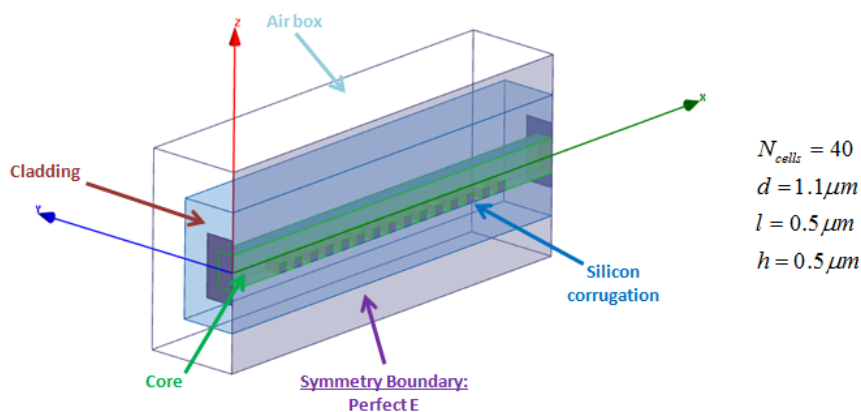$$l = 0.5\mu m$$
$$h = 0.5\mu m$$

Figure 5.7: HFSS model for the perturbed dielectric waveguide.

Fig. 5.8 shows the scattering parameters of the perturbed dielectric waveguide. As can be seen, the influence of the addition of the set of corrugations is such that both reflection and transmission coefficients have been considerably modified when compared to those obtained in the unperturbed dielectric waveguide: the matching has got overall worse and the power transmitted to the output port has been reduced as well. Nevertheless, this leaky structure is quite efficient, since it reflects in the worst case the 10% of the incoming power back to the source; it reflects less than 5% of the input power in almost the entire operating frequency range.

Note that a very interesting feature of this figure is the appearance of a peak in the S_{11} parameter, which is related to the broadside radiation frequency and the characteristic radiation reduction in periodical LWAs. In this case, the perturbations dimensions are optimized in order to overcome this negative effect. The S_{21} parameter has decreased due to the radiation losses present in the structure.
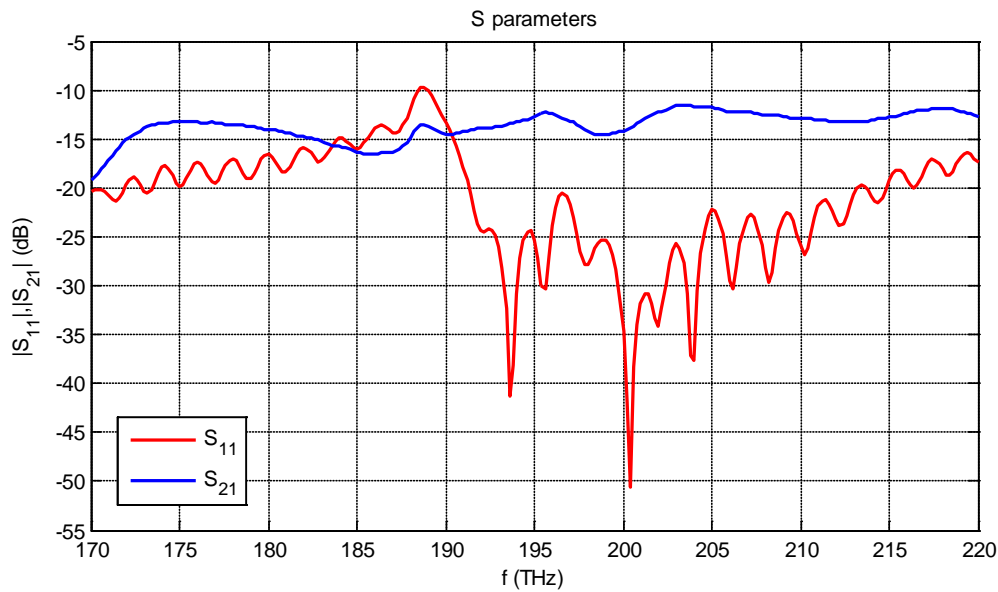

Figure 5.8: S – parameters.

After obtaining the scattering parameters of the perturbed waveguide, the next step would be to calculate the complex propagation constant, as well as its Bloch impedance. These parameters are crucial to confirm the initial hypothesis that this structure behaves as a LWA at optical frequencies, and can be obtained by using the theoretical basis commented in section 3.2. The results are presented in Figs. 5.9 – 5.11.

Fig. 5.9 shows the characteristic impedance of the perturbed waveguide, where is compared with the port impedance as a function of frequency. Due to the presence of radiation losses, the characteristic impedance obtained is complex, and presents a capacitive behavior for 'LH' frequencies and an inductive behavior for 'RH' frequencies, for this particular set of corrugations. Note that at broadside radiation frequency, the characteristic impedance changes considerably: the real part suffers an important reduction and the imaginary part switches from capacitive behavior to inductive behavior. Moreover, since the imaginary part of the characteristic impedance is smaller in value to

the real part at any frequency, it is expected to have a very small leakage rate and, consequently, a very narrow main beam for any frequency as well.
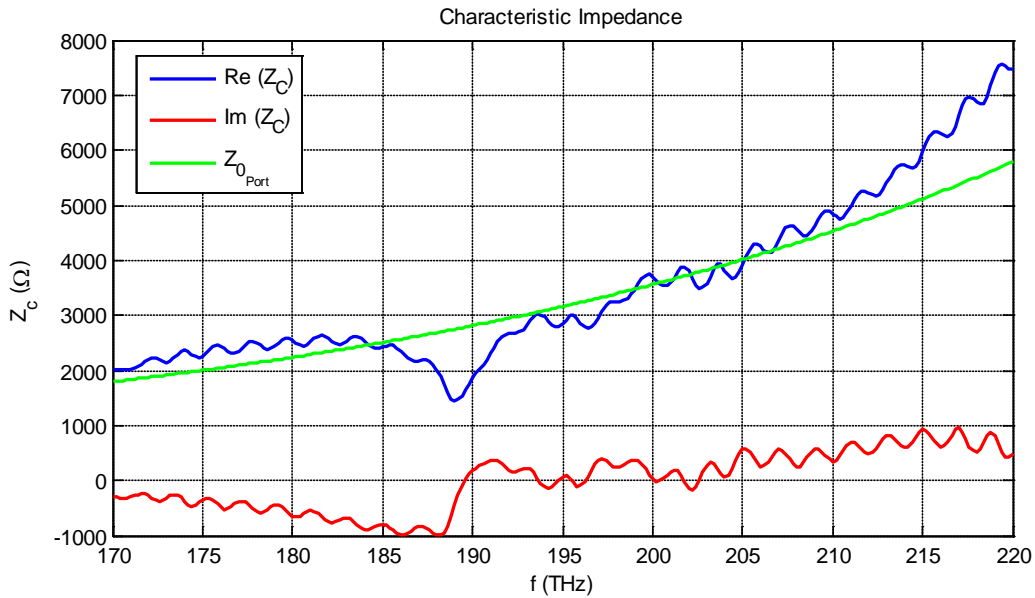

Figure 5.9: Perturbed waveguide characteristic impedance.

The normalized propagation constant is shown in Fig. 5.10. Three different curves are presented; in order of appearance: the fast space harmonic in the perturbed structure, the dominant mode in the unperturbed structure and an illustrative curve for the space harmonic n = -1, considering in this case that the geometry of set of corrugations influences slightly the phase constant, and the period is more relevant. This last curve is quite useful, as it provides an approximate phase constant of the propagating wave without needing to analyze the actual structure during hours. It can be seen that the exact and the approximate curve are similar, but differ mostly due to the influence of the geometry of the perturbation.
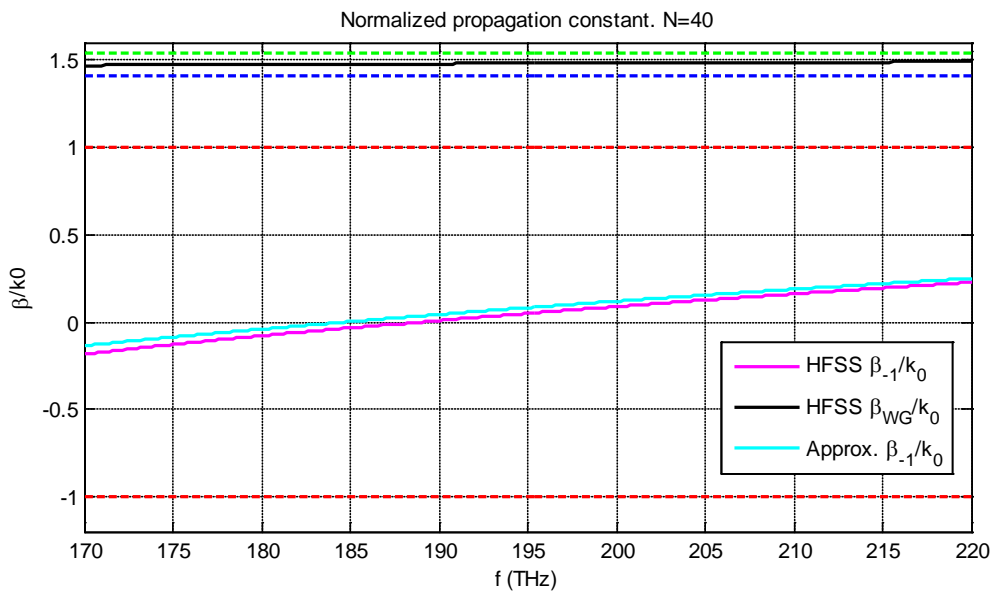

Figure 5.10: Normalized propagation constant.

As previously commented, the broadside radiation frequency is determined by the dimensions of the perturbations employed, which is the main difference between the exact and approximate β_{-1} curves. To conclude, with this set of corrugations, the whole mode becomes fast since the space harmonic $n = -1$ is within the fast-wave region in the frequency range of interest.
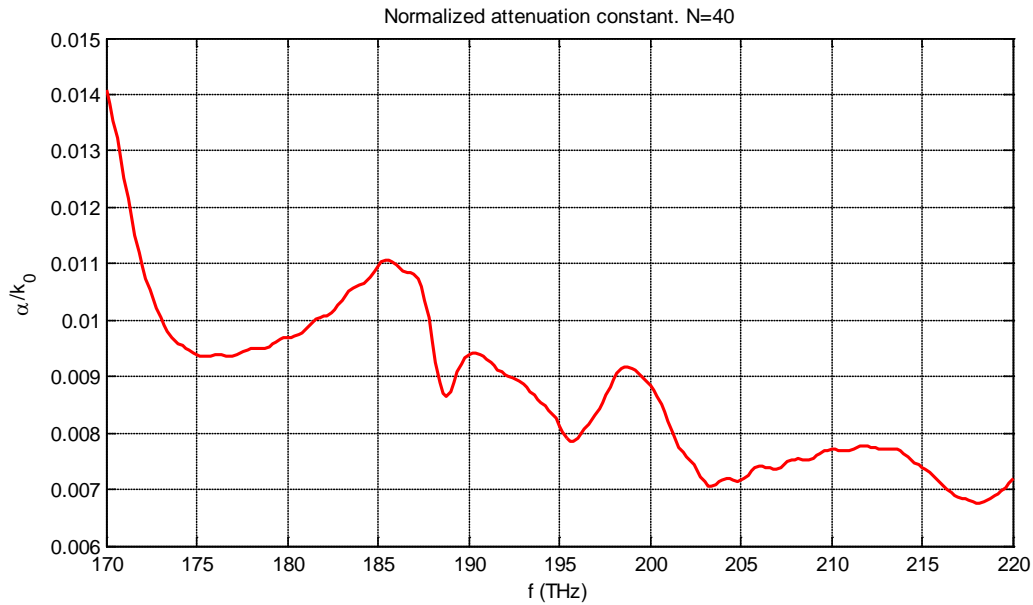

Figure 5.11: Normalized attenuation constant.

The normalized attenuation constant is depicted in Fig. 5.11. Note that the values are overall very small, as commented before.
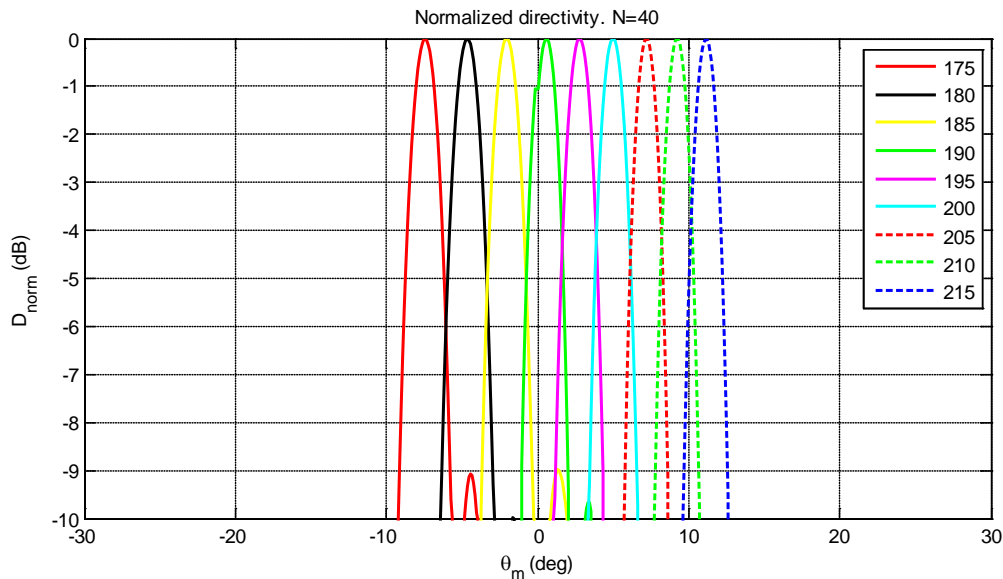

Figure 5.12: Beam scanning capability in XZ plane.

Fig. 5.12 shows the beam scanning capability of the perturbed waveguide in the XZ plane. Main beams are very narrow due to the small values of leakage rate. These results, altogether with those presented in Fig. 5.13 are very important, since they confirm the

hypothesis that this perturbed waveguide behaves as a leaky-wave antenna at optical frequencies. Fig. 5.13 shows the comparative between the angles obtained with the HFSS FarField calculator and the angles calculated from the normalized propagation constant, following the leaky-wave theory presented in section 3.1. As can be seen, excellent agreement is found.
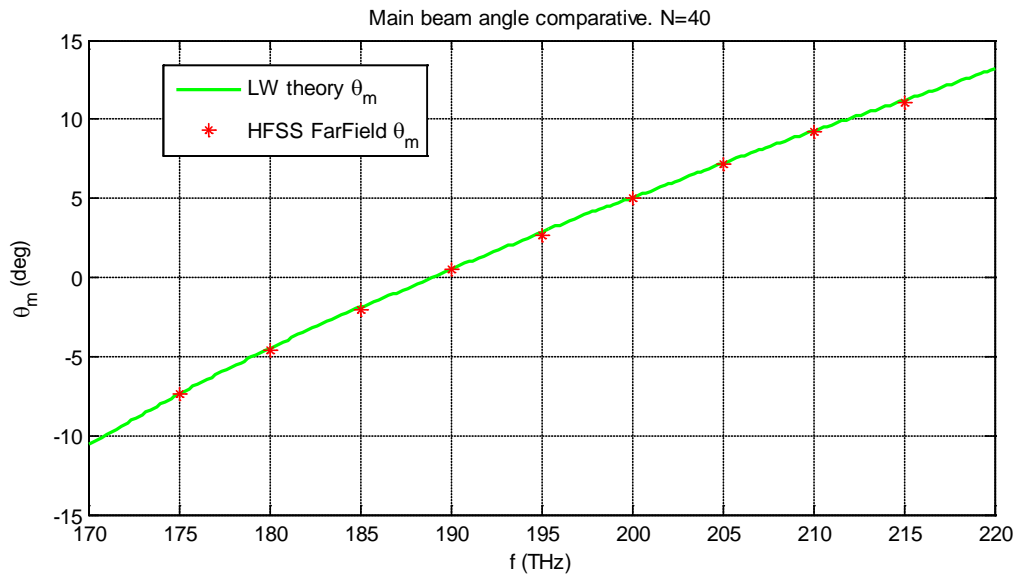

Figure 5.13: Main beam angle comparative.

The radiation pattern in the XZ plane as a function of frequency is illustrated in Fig. 5.14. Note that, since the guiding structure is completely open, LW radiation takes place at angles near broadside, as well as at angles in the diametrical direction. In this case, with this set of perturbations the radiation phenomenon is stronger at the bottom face.
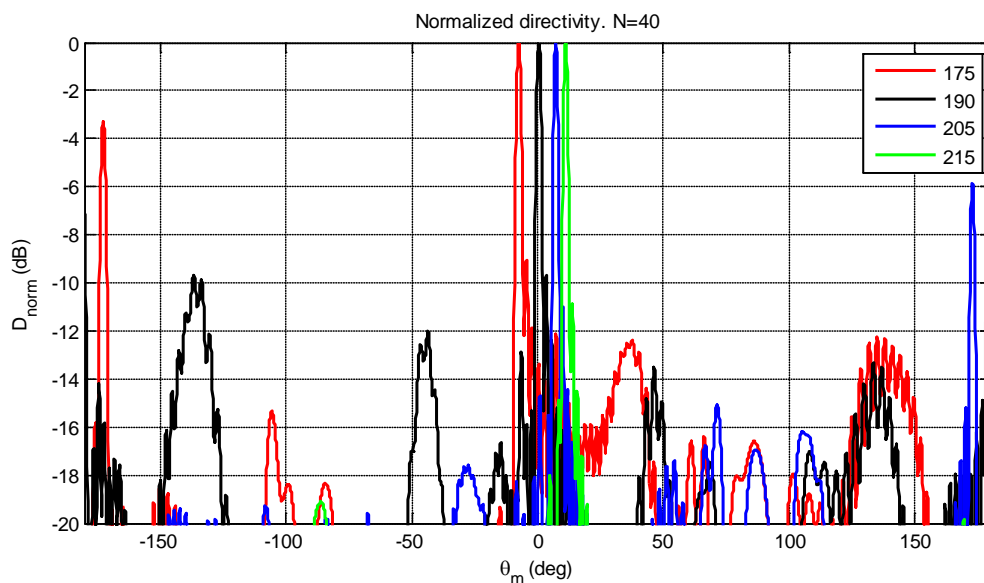

Figure 5.14: Normalized radiation pattern in function of frequency.

In this figure, with the purpose of presenting clearly the scanning effect, the angle axis has been modified. Since radiation is stronger at the bottom face, larger main beams actually

point at negative angles (-170º to +170º, through -180º), not at angles near 0º. Also, side lobes are -10 dB below main beam at any frequency, which is characteristic of a uniform N-cell LWA. This alternative implementation of an optical leaky-wave antenna is, a priori, easier to manufacture. The design proposed in [Song, 2011] is shown in Fig. 5.15. The materials used for the cladding and the core are both solids, as well as the corrugations and are all based on silicon. Since these semiconductors can be electronically tuned, it is possible to modify the radiation capabilities of the antenna. Unfortunately, the tunability via carrier injection does not introduce noticeable improvements in the radiation properties. On the other hand, it is obvious that its practical implementation can be quite difficult, mostly due to the geometry of the corrugations and the use of solid materials embedded into other solids.
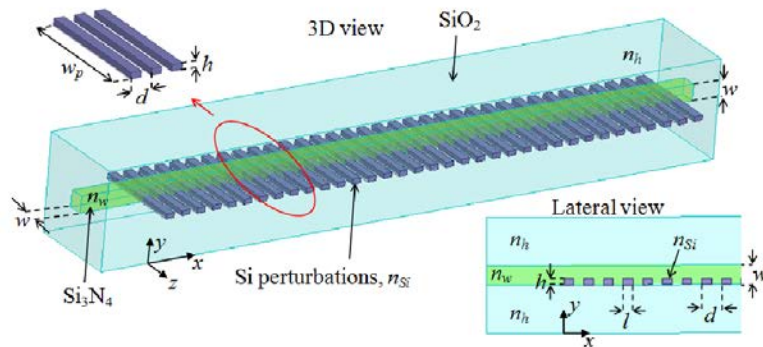

Figure 5.15: Silicon-On-Isolator OLWA. Reproduced from [Song, 2011].

Due to this, a practical implementation based on both solids and liquids gets more appealing. The alternative design makes use of smaller perturbations in the Y direction; the perturbations are only inside the core, and do not pass through the cladding. In contrast with the design proposed in [Song, 2011], the perturbations pass through the cladding, as well as through the core. As could be seen in the presented results, this modification did not affect the radiation capabilities of the optical antenna, and reduces the complexity overall for fabrication. In soft lithography techniques (such as replica molding [Xia, 1996] or decal transfer lithography [Henzie, 2007], among others), flexible materials such as PDMS acts as a mold for pattern replication; these techniques can be applied in order to create a microfluidic channel, where a determined liquid (namely, the fiber's core) will flow.
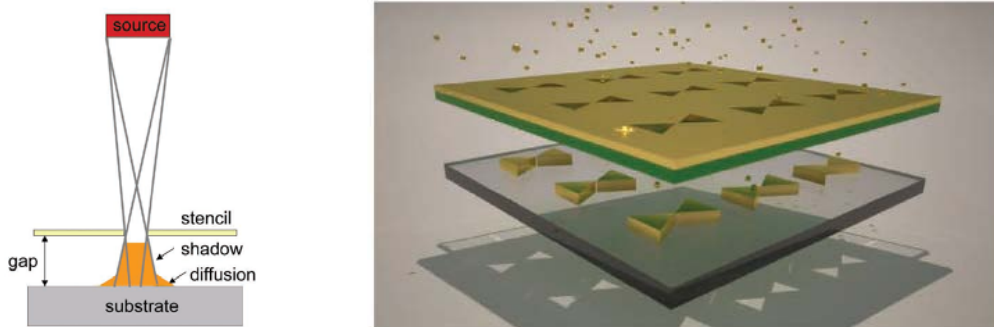

Figure 5.16: Nanostencil lithography technique. Reproduced from [Aksu, 2011]

On the other hand, there are novel methods that can enable nanopatterning on flexible substrates in a single fabrication step. One of these techniques is the nanostencil lithography, proposed in [Aksu, 2011], which utilizes a stencil for transferring nanopatterns to any planar surface. The stencil, when placed on a substrate, acts like a mask and the applied agent (organic or inorganic) is deposited in the apertures present on the stencil. After the stencil is removed, the nanoparticles deposited are attached to the substrate, and have shapes complementary to those of the apertures on the mask. Figure 5.16 depicts this procedure.

Therefore, considering theses fabrication techniques for nanodevices, a possible implementation of the optical antenna may be as follows:

- Start with a rectangular PDMS substrate.
- The perturbations are added by using NanoStencil Lithography. With this technique, evaporated materials can be deposited directionally with a stencil in a substrate.
- After that, the microfluidic chamber is created by using soft lithography on another block of PDMS.
- Finally, the microfluidic channel and the modified substrate are attached.

Fig. 5.17 illustrates the concept of the proposed microfluidic optical leaky-wave antenna. As can be seen, it is needed an additional section of TL in order to ensure that the excited mode corresponds to the desired one, in which the electric field is polarized along the corrugations direction. Moreover, a new beam scanning capability has been introduced: for a given frequency, the antenna can radiate at different angles depending on the liquid flowing through the microfluidic channel, as long as this liquid satisfies the total internal reflection condition to ensure that the mode of the unloaded TL in tightly confined. It is important to notice that in this antenna the radiation pattern theoretically is a fan beam. However, in Fig.5.17 it is shown as a pencil beam, but only in an illustrative way.
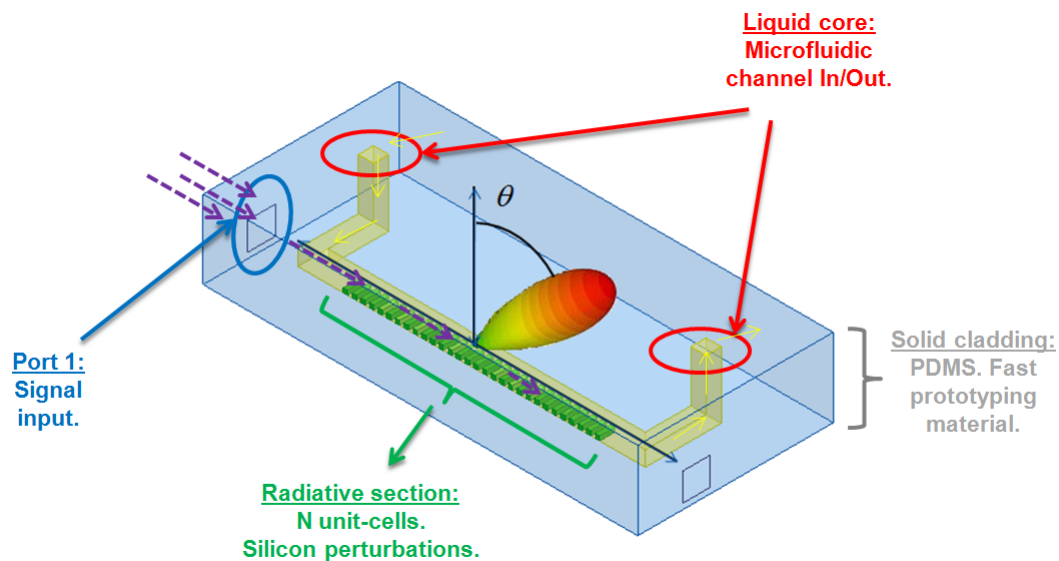

Figure 5.17: Proposed microfluidic optical leaky-wave antenna.

This novel concept can be explained with a straightforward train of thought: the phase constant in the rectangular optical fiber depends on both core and cladding refractive indexes, as well as the width of the core. At a fixed frequency, the mode will be more confined for structures with a higher refractive index difference between the core and the cladding, affecting directly the propagation constant. Fig. 5.18 illustrates this concept. As can be seen, in the frequency range of interest, the change of the employed liquid core leads to an increase/decrease in the modal refractive index, depending on the increase/decrease of the core refractive index.
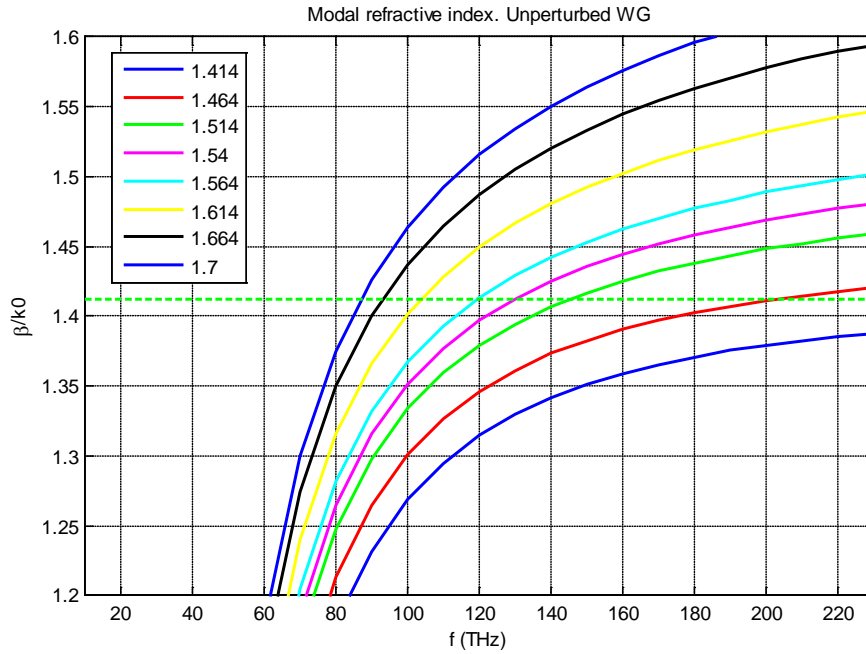
Figure 5.18: Phase constant for different core refractive indexes.

After introducing the perturbations, the fast space harmonic will also change accordingly, as shown in Fig. 5.19. Fig. 5.20 illustrates the beam scanning capability of this proposed novel implementation, as the main beam angle varies in concordance with the modifications of the liquid's refractive index.

Figure 5.19: OLWA normalized propagation constant in function of n$_{core}$.

Figure 5.20: Tunable beam scanning effect.

Conclusions

In this project, two antennas based on the leaky-wave concept, operating at microwave and optical frequencies, have been studied thoroughly. For the first research line, it has been demonstrated that **the reduction of the side lobe level** in a mushroom-type compo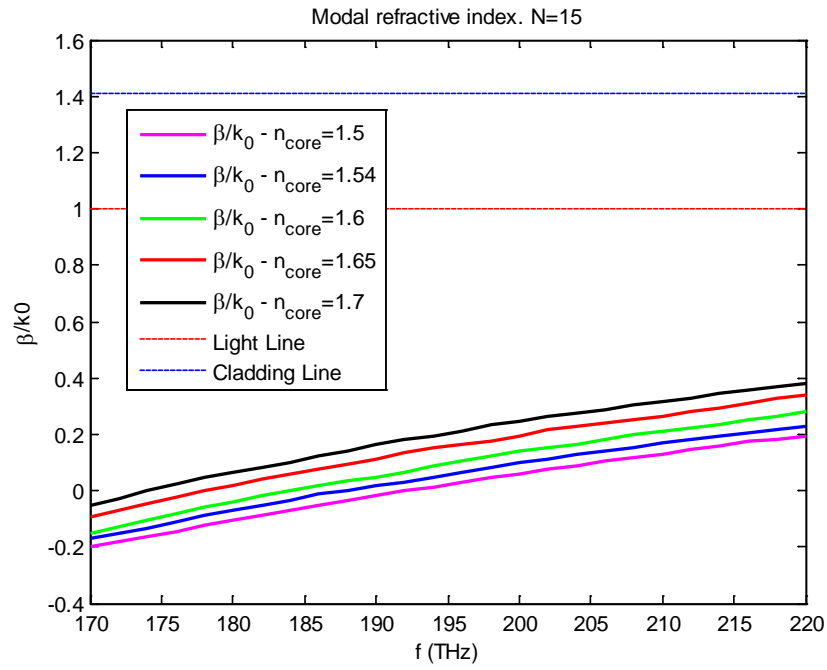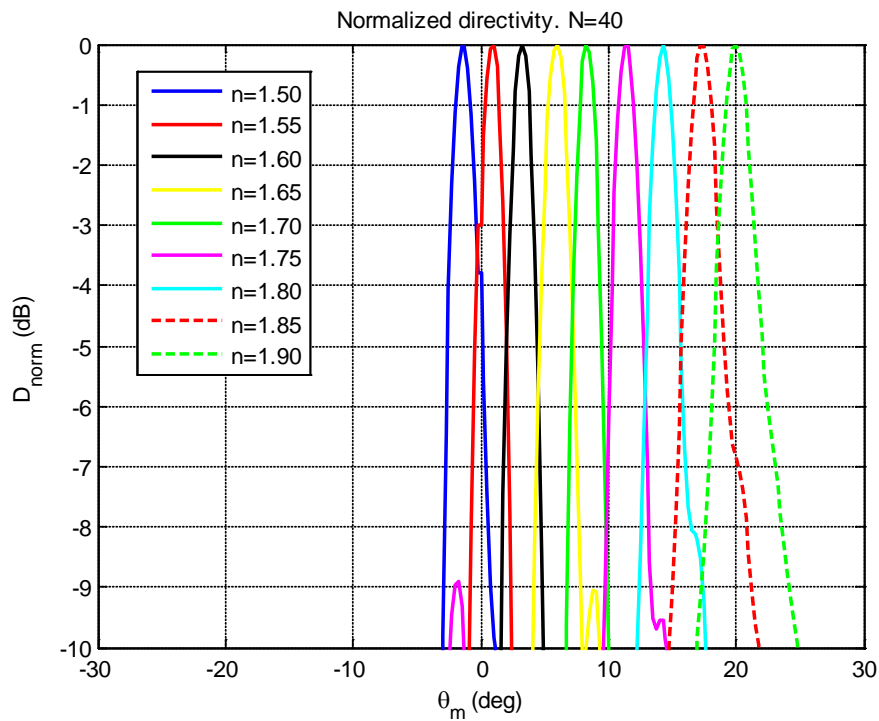site right/left-handed LWA **can be achieved by modifying the aperture illumination distribution**, via the **variation of the geometrical parameters** involved in the mushroom-type structure. The process that led to the consecution of this main objective has been divided in the following steps:

1. An initial analysis of the PPW CRLH-LWA was done by using an iterative method based on modal-matching techniques and Floquet's theorem, in order to understand the behavior and the characteristics of the base antenna. The antenna operates with the fundamental space harmonic of the propagating mode, and can radiate in angles ranging from back-fire to end-fire directions, passing through broadside. At broadside, it cannot radiate efficiently due to the lack of a shunt resistor in the analytical TL-lumped elements model, even if the whole structure is balanced.

2. A study of the influence of the mushroom-type structure geometrical parameters in the complex propagation constant of the propagating mode. This study was carried out in two steps:

   2.1. First, making variations of solely one parameter at the time. This would give the isolated influence of a determined parameter on the antenna properties. Since these variations led implicitly to unbalanced structures, the mode-matching technique could not be used for this study; commercial EM software HFSS was used instead. The obtained results showed that **modifying an isolated geometrical parameter does not provide isolated control on the phase constant or the attenuation constant**. Therefore, several geometrical parameters have to be simultaneously modified to control effectively the complex propagation constant of the antenna.

   2.2. With this purpose, a second study consisting of the **simultaneous variation of the length of the unit-cell and the slot width** was carried out, as these two parameters have several advantages over the remaining parameters; the

remaining had constant values during the study. Increments in the unit-cell length often provide greater main beam angles and smaller leakage rates. On the other hand, increments in the slot width produce an increase in the leakage rate and a subtle decrease in the main beam angle as well. The results, represented in contour plots, showed that **it was possible to control effectively both phase and attenuation constant by varying these two parameters** in both LH and RH frequency bands. Moreover, the obtained contour plots showed that **a tapered geometry could provide several values of leakage rate with a fixed main beam angle**. However, the viability of a taper design was only exclusive to the RH frequency region, since the attenuation constant obtained in the LH region was extremely high, and the control over it was insufficient for a taper design.

3. The election of a specific aperture illumination distribution to reduce side lobes to a desired level. In this step, certain **limitations were considered in order to quantify their effect on the resultant aperture illumination and, consequently in the side lobe level**. It could be seen that the unavailability of small values of attenuation constant affects considerably the desired aperture illumination. Therefore, it is crucial to obtain small values in order to succeed in the pursuance of a side lobe level reduction.

4. The design of a tapered geometry that provides the required leakage distribution. The geometry variations were such that they provided the required normalized attenuation constant distribution and a fixed main beam angle. Two designs were made in this project. The first one and its results served as a proof of concept, whereas the second antenna was designed with different materials, with the purpose of manufacturing it. In both cases, the results showed a **clear reduction in the side lobe level compared to those obtained in the non-tapered antennas**, fully achieving the main objective of the project.

The second research line was related to the **translation** of some **microwave theory concepts and techniques**, such as the concept of **leaky modes**, to open structures that operate as **antennas** at near-IR **optical frequencies**. The study and design of this antenna were developed by following the next steps:

1. A study of the rectangular optical fiber as a conventional transmission line was performed to understand the principle of functioning and the propagation characteristics of a specific mode. Commercial EM software HFSS was used for this purpose. The results showed that the cut-off frequency depended mainly of the difference of the core and cladding refractive indexes, as well as the dimensions of the core. Also, it could be seen that when the mode was tightly confined, the wave would propagate without attenuation along the longitudinal direction.

2. A study of the rectangular optical fiber, but now **loaded with a periodical arrangement of silicon corrugations**. The obtained results showed many differences with those obtained with the unloaded optical waveguide. The

influence of the corrugations was such that they **perturbed the dominant mode of the rectangular optical fiber**. Even though the mode was slightly perturbed, **radiation phenomenon took place**, since the waveguide is naturally open. The obtained results, after applying the theoretical basis reviewed in Chapter 3, showed very good agreement between the simulated and theoretical main beam angles. All these results suggest that **the optical structure behaved exactly as a leaky-wave antenna**.

3. The addition of a novel beam scanning capability of the antenna implemented with microfluidics technology. The results showed that, **after changing the refractive index of the liquid core, the main beam angle will change accordingly**: for increments in the core refractive index, the pointing angle moves toward the end-fire direction, and for decrements in the core refractive index, the pointing angle moves toward the back-fire direction.

It is important to highlight that the main objectives initially target in both research lines have been successfully achieved in this project.

Bibliography

[Aksu, 2011] Aksu, S., Huang, M., Artar, A., Yanik, A. A., Selvarasah, S., Dokmeci, M. R. and Altug, H. (2011), Flexible Plasmonics on Unconventional and Nonplanar Substrates. Adv. Mater., 23: 4422–4430.

[Álvarez Melcón, 1998] Álvarez Melcón, A., Mosig, J.R. Strip, Slot, Air, Inverted Patch (SSAIP): A Cavity Backed Alternative to Broadband Communication Antennas. In Radio Science, vol. 33, n. 6, pp. 1525-1542, November-December 1998.

[Balanis, 2005] Balanis, C. A. (2005). Antenna Theory: Analysis and Design. 3rd Edition. JohnWiley and Sons.

[Balanis, 2007] Jackson, D. R. and Oliner, A. A. (2007) Leaky-Wave Antennas, in Modern Antenna Handbook (ed C. A. Balanis), John Wiley & Sons, Inc., Hoboken, NJ, USA.

[Caloz et al., 2002] Caloz, C., Obake, H., Iwait, H., and Itoh, T. (2002). Transmission line approach of left-handed (LH)materials. In Proc. USNC/URSI Nat. Radio Sci.Meeting, page 39, San Antonio, TX.

[Caloz and Itoh, 2006] Caloz, C. and Itoh, T. (2006). Electromagnetic Metamaterials: Transmission Line Theory and Microwave Applications. Wiley and IEEE Press.

[Floquet, 1883] Floquet, Gaston (1883), "Sur les équations différentielles linéaires à coefficients périodiques", Annales de l'École Normale Supérieure 12: 47–88

[Friedman, 1988] L. Friedman, R. A. Soref, and J. P. Lorenzo, (1988) Silicon double-injection electro-optic modulator with junction gate control, J. Appl. Phys. 63(6), 1831–1839.

[García-Vigueras, 2010] García-Vigueras, M., Gómez-Tornero, J.L., Guzmán-Quirós, R., Quesada-Pereira, F., and Alvarez-Melcón, A. (2010), Control of the Radiation Properties of a FSS Loaded Leaky-Wave Antenna,in Proc. 4th Eur. Conf. Antennas Propag. , Apr. 12–16, pp. 1–4.

[Gómez-Díaz et al., 2011a] Gómez-Díaz, J. S., Álvarez-Melcón, A., and Bertuch, T. (2011a). A modal based iterative circuit model for the analysis of CRLH leaky-wave antennas

comprising periodically loaded PPW. IEEE Transactions on Antennas and Propagation, 59(4):1101–1112.

[Gómez-Díaz et al., 2011b] Gómez-Díaz, J. S., Álvarez-Melcón, A., and Bertuch, T. (2011b). Radiation characteristics of mushroom-like PPW LWAs: Analysis and experimental verification. IEEE Antennas and Wireless Propagation Letters.

[Gómez-Díaz et al., 2011c] Gómez-Díaz, J. S., Cañete-Rebenaque, D., and Álvarez-Melcón, A. (2011c). A simple CRLH LWA circuit condition for constant radiation rate. IEEE Antennas and Wireless Propagation Letters, 10:29–32.

[Gómez, 2005] J. L.Gómez, A. de la Torre, D. Cañete, M. Gugliemi, and A. A. Melcón (2005), Design of tapered leaky-wave antennas in hybrid waveguide-planar technology for millimeter waveband applications, IEEE Trans. Antennas Propag, vol. 53, no. 8, pt. I, pp. 2563–2577, Aug. 2005.

[Gomez et al., 2005] Gomez-Tornero, J. L., Quesada-Pereira, F. D., and Alvarez-Melcon, A. (2005). Analysis and design of periodic leaky-wave antennas for the millimeter waveband in hybrid waveguide-planar technology. IEEE Transactions on Antennas and Propagation, 53(9):2834– 2842.

[Gómez, 2008] Gomez-Tornero, J., Caete-Rebenaque, D., and Alvarez-Melcon, A. (2008), Microstrip leaky-wave antenna with control of leakage rate and only one main beam in the azimuthal plane, IEEE Trans. Antennas Propag., vol. 56, no. 2, pp. 335 –344, Feb. 2008

[Henzie, 2007] J. Henzie, M.H. Lee, and T.W. Odom, (2007). Multiscale Patterning of Plasmonic Metamaterials. Nature Nanotech. 2, 549-554

[Iyer and Eleftheriades, 2002] Iyer, A. K. and Eleftheriades, G. (2002). Negative refractive index metamaterials supporting 2-D waves. In IEEE International Microwave Symposium Digest, pages 412–415, Seattle,WA, USA.

[Jarry and Beneat, 2008] Jarry P, Beneat J. (2008), Advanced Design Techniques and Realizations of Microwave and RF Filters, John Wiley & Sons, Inc.

[Kraus and Marhefka, 2001] J. D. Kraus and R. J. Marhefka (2001). Antennas. McGraw Hill, Third Edition.

[King et al., 1983] King, R. J., Thiel, D. V., and Park, K. S. (1983), The synthesis of surface reactance using an artificial dielectric. IEEE Transactions on Antennas and Propagation, 31(3):471 – 476.

[Oliner, 2003] A. Oliner (2003). Leaky-wave antennas, in Antenna Engineering Handbook, Third Edition, edited by R. C. Johnson, McGraw Hill, 1993.

[Pendry et al., 1999] Pendry, J. B., Holden, A. J., Robbins, D. J., and Stewart,W. J. (1999). Magnetism from conductors, and enhanced non-linear phenomena. IEEE Transactions onMicrowave Theory and Techniques, 47(11):2075–2084.

[Pozar, 2005] Pozar, D. (2005). Microwave Engineering. JohnWiley and Sons, 3rd edition.

[Psaltis, 2006] Demetri Psaltis D., Stephen R. Quake and Changhuei Yang (2006). Developing optofluidic technology through the fusion of microfluidics and optics., in Nature Vol 442, 381-386.

[Ramo et al., 1994] Ramo, S.,Whinnery, J. R., and Duzer, T. V. (1994). Fields and Waves in Communication Electronics. John Wiley and Sons, 3rd edition.

[Sederberg, 2011] S. Sederberg and A. Y. Elezzabi (2011), Nanoscale plasmonic contour bowtie antenna operating in the mid-infrared, Opt. Express 19, 15532-15537.

[Shelby et al., 2001] Shelby, R. A., Smith, D. R., and Schultz, S. (2001). Experimental verification of anegative index of refraction. Science, 292(5515):77–79.

[Siragusa, 2012] Siragusa, R. Perret, E., Lemaitre-Auger, P., Van Nguyen, H., Tedjini, S., Caloz, C. (2012), A Tapered CRLH Interdigital/Stub Leaky-Wave Antenna With Minimized Sidelobe Levels. IEEE Antennas and Wireless Propagation Letters, 11:1214–1217.

[Smith et al., 2000] Smith, D., Padilla, W. J., Vier, D., Nemat-Nasser, S., and Schultz, S. (2000). Composite medium with simultaneously negative permeability and permittivity. Physical Review Letters, 84:4184–4187.

[Song, 2009] Q. Song, F. Qian, E. K. Tien, I. Tomov, J. Meyer, X. Z. Sang, and O. Boyraz, (2009) Imaging by silicon on insulator waveguides, Appl. Phys. Lett. 94(23), 231101 (2009).

[Song, 2011] Q. Song, S. Campione, O. Boyraz, and F. Capolino, (2011) Silicon-based optical leaky wave antenna with narrow beam radiation, Opt. Express 19, 8735-8749 (2011)

[Toth, 2009] C. K. Toth, (2009). R&D of mobile LIDAR mapping and future trends, in Proceeding of ASPRS 2009 Annual Conference (Baltimore, Maryland, 2009).

[Xia, 1996] Xia, Y.; Kim, E.; Zhao, X.-M.; Rogers, J. A.; Prentiss, M. and Whitesides, G. M. (1996). Complex optical surfaces by replica molding against elastomeric masters, In Science 1996, 273, 347-349.

[Wang, 2011] Yan Wang, Amr S. Helmy, and George V. Eleftheriades (2011). Ultra-wideband optical leaky-wave slot antennas, Opt. Express 19, 12392-12401 .

Web references

[Link 1] http://www.upv.es/antenas/Documentos_PDF/Notas_clase/aperturas.pdf

[Bertuch, 2011] Dispersion Properties of Periodically Loaded Parallel-Plate Waveguides: http://151.100.120.244/personale/frezza/EuSA/thirdEdition/CourseLectures/ThursdayApril28/2011_04_28_ESOA_LWA_Bertuch.pdf